Nitrogen-Doped Carbon Materials as Oxygen Reduction Reaction Catalysts for Metal-Air Fuel Cells and Batteries

By

Zhu Chen

A thesis

presented to the University of Waterloo

in fulfillment of the degree of

Master of Applied Science

in

Chemical Engineering

Waterloo, Ontario, Canada, 2012

Author’s declaration:

I hereby declare that I am the sole author of this thesis. This is a true copy of the thesis, including any required final revisions, as accepted by my examiners.

I understand that my thesis may be made electronically available to the public.

Abstract

Metal air battery has captured the spotlight recently as a promising class of sustainable energy storage for the future energy systems. Metal air batteries offer many attractive features such as high energy density, environmental benignity, as well as ease of fuel storage and handling. In addition, wide range of selection towards different metals exists where different energy capacity can be achieved via careful selection of different metals. The most energy dense systems of metal-air battery include lithium-air, aluminum-air and zinc-air. Despite the choice of metal electrode, oxygen reduction (ORR) occurs on the air electrode and oxidation occurs on the metal electrode. The oxidation of metal electrode is a relatively facile reaction compared to the ORR on the air electrode, making latter the limiting factor of the battery system. The sluggish ORR kinetics greatly affects the power output, efficiency, and lifetime of the metal air battery. One solution to this problem is the use of active, affordable and stable catalyst to promote the rate of ORR. Currently, platinum nanoparticles supported on conductive carbon (Pt/C) are the best catalyst for ORR. However, the prohibitively high cost and scarcity of platinum raise critical issues regarding the economic feasibility and sustainability of platinum-based catalysts. Cost reduction via the use of novel technologies can be achieved by two approaches. The first approach is to reduce platinum loading in the catalyst formulation. Alternatively platinum can be completely eliminated from the catalyst composition. The aim of this work is to identify and synthesize alternative catalysts for ORR toward metal air battery applications without the use of platinum re other precious metals (i.e., palladium, silver and gold).

Non-precious metal catalysts (NPMC) have received immense international attentions owing to the enormous efforts in pursuit of novel battery and fuel cell technologies. Different types of

NPMC such as transition metal alloys, transition metal or mixed metal oxides, chalcogenides have been investigated as potential contenders to precious metal catalysts. However, the performance and stability of these catalysts are still inferior in comparison. Nitrogen-doped carbon materials (NCM) are an emerging class of catalyst exhibiting great potential towards ORR catalysis. In comparison to the metal oxides, MCM show improved electrical conductivity. Furthermore, NCM exhibit higher activity compared to chalcogenides and transition metal alloys. Additional benefits of NCM include the abundance of carbon source and environmental benignity. Typical NCM catalyst is composed of pyrolyzed transition metal macrocycles supported by high surface area carbon. These materials have demonstrated excellent activity and stability. However, the degradation of these catalysts often involves the destruction of active sites containing the transition metal centre. To further improve the durability and mass transport of NCM catalyst, a novel class of ORR catalyst based on nitrogen-doped carbon nanotubes (NCNT) is investigated in a series of studies.

The initial investigation focuses on the synthesis of highly active NCNT using different carbon-nitrogen precursors. This study investigated the effect of using cyclic hydrocarbon (pyridine) and aliphatic hydrocarbon (ethylenediamine) towards the formation and activity of NCNT. The innate structure of the cyclic hydrocarbon promotes the formation of NCNT to provide higher product yield; however, the aliphatic hydrocarbon promotes the formation of surface defects where the nitrogen atoms can be incorporated to form active sites for ORR. As a result, a significant increase in the ORR activity of 180 mV in half-wave potential is achieved when EDA was used as carbon-nitrogen precursor. In addition, three times higher limiting current density was observed for the NCNT synthesized from ethylenediamine.

Based on the conclusion where highly active NCNT was produced from aliphatic hydrocarbon, similar carbon-nitrogen precursors with varying carbon to nitrogen ratio in the molecular structure (ethylenediamine, 1, 3-diaminopropane, 1, 4-diaminobutane) were adapted for the synthesis of NCNT. The investigation led to the conclusion that higher nitrogen to carbon ratio in the molecular structure of the precursors benefits the formation of active NCNT for ORR catalysis. The origin of such phenomena can be correlated with the higher relative nitrogen content of the resultant NCNT synthesized from aliphatic carbon precursor that provided greater nitrogen to carbon ratio. As the final nitrogen content increased in the molecular structure, the half-wave potential of the resultant NCNT towards ORR catalysis was increased by 120 mV. The significant improvement hints the critical role of nitrogen content towards ORR catalysis.

To further confirm the correlation between the nitrogen content and ORR activity, another approach was used to control the final nitrogen content in the resultant NCNT. In the third investigation, a carbon-nitrogen precursor (pyridine) was mixed with a carbon precursor (ethanol) to form an admixture. The relative proportion of the two components of the admixture was varied to produce NCNT with different nitrogen content. By adopting this methodology, potential effect of different carbon-nitrogen precursors on the formation of NCNT can be eliminated since the same precursors were used for NCNT synthesis. Based on the electrochemical evaluations, the nitrogen content can be positively correlated to ORR activity. Among the NCNT samples, 41% higher limiting current density was achieved for 0.7 at. % increase in overall nitrogen content. Furthermore, the selectivity of the NCNT catalyst with higher nitrogen content favours the production of water molecule—the favourable product in metal-air battery by 43%.

ORR catalyst is an outer-sphere electron transfer reaction whereby the reactants interact with the surface of catalysts. Consequently, the surface structure can be a determining factor towards the ORR activity of the NCNT in addition to the nitrogen content. In the forth investigation, the surface structure of NCNT was tailored to differentiate the ORR activity of smooth and rugged surface while controlling the overall nitrogen content to be similar. NCNT having different surface structures but similar nitrogen content (approximately 2.7 to 2.9 at. %) were successfully synthesized using different synthesis catalysts. Comparison of the two NCNT catalysts showing different surface structure resulted in a 130 mV increased in half-wave potential favouring the NCNT with more rugged surface structure. This study provided insights to the potential effects of synthesis catalyst towards directing the surface structure and the ORR activity of NCNT.

Through a series of studies, the important parameters affecting the ORR performance of NCNT were elucidated and the most active NCNT catalyst synthesized was used for testing in a prototype zinc-air battery. The fifth study evaluated the performance of NCNT catalyst in different concentrations of alkaline electrolyte and at different battery voltage. An increase in the electrolyte's alkaline strength improved the battery performance to a certain degree until the increasing viscosity impeded the performance of the battery system. The zinc-air battery employing NCNT as ORR catalyst produced a maximum battery power density of 69.5 $mWcm^{-2}$ in 6M potassium hydroxide. The fifth study illustrated the great potential of NCNT towards the ORR catalysis for metal-air batteries.

In combination, the series of investigations presented in this document provide a comprehensive study of a novel material and its application towards ORR catalysis in metal air batteries. Specifically, this report provides insights into the fundamentals of NCNT synthesis; the origins of ORR activity and the optimal operating conditions of NCNT in a prototype zinc-air battery. The excellent performance of NCNT warrants further studies of this material in greater details, and the information presented in this document will create a basis for future investigations towards ORR catalysis.

Acknowledgements

The work reported herein was financially supported by the Natural Sciences and Engineering Research Council of Canada and the University of Waterloo.

The author would like to thank Dr. Zhongwei Chen, and Dr. Aiping Yu for their guidance and tremendous assistance in the Master's study.

Special thanks goes to author's colleagues including, Drew Higgins, Ja-Yeon Choi, Ryan Hsu, Jason Wu, Shaomin Zhu, Haisheng Tao, Dr. Wenmu Li, Dr. Bing Li, Raihan Ahmed, Hadis Zarrin, Jared Lenos and Noorin Samji for their assistance and support.

Furthermore, the author would like to acknowledge the critical inputs of reviewers, including Dr. Zhongwei Chen, Dr. Yuning Li and Dr. Nasser Mohieddin Abukhdeir.

Table of Contents

List of figures xii

List of tables xv

List of abbreviations, symbols and nomenclature xvi

1 Introduction 1

1.1 Metal Air Battery 4

1.1.1 Operation principles of zinc-air battery 8

1.1.2 Technical challenges 16

1.2 Nitrogen-doped carbon nanotube 18

1.3 Scope and objectives 28

2 Materials synthesis and characterization 29

2.1 Chemical vapour deposition synthesis 29

2.2 Scanning electron microscopy 32

2.3 Transmission electron microscopy 34

2.4 X-ray diffraction 37

2.5 X-ray photoelectron spectroscopy 39

2.6 Raman spectroscopy 40

2.7 Thermogravimetric analysis 42

2.8 Half-cell electrochemical evaluation 43

2.9 Zinc-air battery evaluation 48

3 Effects of precursor structure on the ORR activity of NCNT 51

3.1 Purpose of the study 51

3.2 Experimental methods 52

3.3 Results and discussions 53

3.4 Conclusions and remarks 65

4 Effects of precursor composition on the ORR activity of NCNT 67

4.1 Purpose of the study 67

4.2 Experimental methods 68

4.3 Results and discussions 69

4.4 Conclusions and remarks 85

5 Effects of surface structure on the ORR activity of NCNT 87

5.1 Purpose of the study 87

5.2 Experimental methods 88

5.3 Results and discussions 89

5.4 Conclusions and remarks 97

6 Evaluation of NCNT in prototype zinc-air battery 99

6.1 Purpose of the study 99

6.2 Experimental methods 99

6.3 Results and discussions 100

6.4 Conclusions and remarks 109

7 Summary and future direction 110

References 113

Appendix 121

List of figures

Figure 1 Regone plot showing the energy domain of electrochemical storage technologies. 5

Figure 2 Specific energy density of different battery systems in comparison to gasoline 6

Figure 3 Schematic of a zinc-air battery. 10

Figure 4 Different morphology of zinc electrode. 11

Figure 5 Surfactant assisted deposition of zinc electrode. 11

Figure 6 Structure and function of a typical air electrode for zin-air battery. 14

Figure 7 Ball-and-stick model of SWNT, DWNT and MWNT. 20

Figure 8 Hexagonal lattice of the graphitic wall in CNT. 21

Figure 9 Chirality of CNT. The bonds in red denote the ‘armchair’- and ‘zigzag’-like patterns. 22

Figure 10 Adsorption of dioxygen onto the surface of (9,0)-SWNT. 23

Figure 11 Charge density delocalization as a result of nitrogen doping. 25

Figure 12 Growth mechanism of the NCNT by CVD method. 26

Figure 13 Left, electron micrograph of NCNT and right, schematic of NCNT. 27

Figure 14 CVD setup used for the synthesis of NCNT. 30

Figure 15 Chemical structure of carbon/nitrogen precursors and metal catalysts. 31

Figure 16 Schematic drawing of SEM. 33

Figure 17 Schematic drawing of TEM, ... 35

Figure 18 Experimental setup of XRD, Bragg diffraction and Bragg law. 38

Figure 19 Typical setup of XPS experiment 40

Figure 20 Scattering events encounter in Raman spectroscopy. 42

Figure 21 RRDE voltammetry setup and RRDE electrode schematic. 44

Figure 22 ORR polarization of NCNT under four different rotation speeds. 46
Figure 23 Design of prototype zinc-air battery. 49
Figure 24 SEM image of a) EDA-NCNT and b) Py-NCNT. 53
Figure 25 TEM image of a) EDA-NCNT and b) Py-NCNT. The scale bar in the inset is 20 nm. 55
Figure 26 Polarization curve of EDA-NCNT, Py-NCNT and Pt/C at 1600 rpm. 56
Figure 27 K-L plot and polarization curve of EDA-NCNT, Py-NCNT and Pt/C. 58
Figure 28 a) Tafel plots comparison. Tafel plot of b) EDA-NCNT, c) Py-NCNT and d) Pt/C. ... 60
Figure 29 XPS spectrum of EDA-NCNT and Py-NCNT. 61
Figure 30 HR-XPS of N 1S signal of EDA-NCNT and Py-NCNT. 63
Figure 31 Raman spectrum of EDA-NCNT and Py-NCNT. 65
Figure 32 TEM image of the EDA-NCNT, DAP-NCNT and DAB-NCNT. 70
Figure 33 Elementary composition of the NCNT samples by XPS analysis. 70
Figure 34 ORR polarization (a) and % H2O selectivity (b) of EDA-, DAP- and DAB-NCNT... 71
Figure 35 SEM of a) NCNT-a, b) NCNT-b and c) NCNT-c. 72
Figure 36 TEM images of NCNT-a showing bamboo structure and surface. 73
Figure 37 Polarization disk current (a) and ring current (b) of NCNT samples. 74
Figure 38 KL plot and polarization curve of NCNT-a, NCNT-b and NCNT-c. 77
Figure 39 Tafel plot of a) NCNT-a, b) NCNT-b, c) NCNT-c. 80
Figure 40 HR-XPS of the N 1S signals of NCNT samples. 82
Figure 41 HR-XPS of the C 1S signals of NCNT samples. 85
Figure 42 SEM image of A) Fc-NCNT and B) FePc-NCNT. 89
Figure 43 TEM image of A) Fc-NCNT and B) FePc-NCNT. 91
Figure 44 Polarization curve of Fc-NCNT and FePc-NCNT. 91

Figure 45 Polarization curves and K-L plots of Fc-NCNT and FePc-NCNT..... 93

Figure 46 Tafel plot of A) Fc-NCNT and FePc-NCNT..... 95

Figure 47 XPS spectrum of Fc-NCNT and FePc-NCNT..... 96

Figure 48 Raman spectrum of Fc-NCNT and FePc-NCNT..... 97

Figure 49 (a) SEM and (b) TEM images of NCNT samples. 101

Figure 50 ORR polarization curves of NCNT in 0.1 M KOH..... 102

Figure 51 (a) Koutechy-Levich and (b) Tafel plots for NCNT. 103

Figure 52 Zinc-air battery polarization and power density curves of NCNT coated electrode.. 104

Figure 53 Cathodic potential and power density curves for NCNT coated electrode. 106

Figure 54 Nyquist plots of zinc-air battery single cells with NCNT catalyst..... 107

List of tables

Table 1 Characteristics of metal-air battery 6

Table 2 Characteristics of an ideal separator for zinc-air battery 12

Table 3 Factors affecting the performance of metal-air battery 17

Table 4 Summary of the elemental compositions of EDA-NCNT and Py-NCNT from EDX. 54

Table 5 Summary of the important performance indicators of ORR catalysis. 57

Table 6 Kinetic current of EDA-NCNT, Py-NCNT and Pt/C at different potentials. 59

Table 7 XPS analysis of the elemental composition of EDA-NCNT and Py-NCNT. 61

Table 8 HR-XPS analysis of the N 1S signal of EDA-NCNT and Py-NCNT. 64

Table 9 Elemental composition NCNT samples by EDX. 73

Table 10 Summary of the important ORR performance indicators. 75

Table 11 Kinetic current density of different NCNT samples at various potentials 78

Table 12 Elemental compositions of NCNT samples from XPS analysis. 81

Table 13 HR-XPS analysis of the N 1S signal. 82

Table 14 Elemental composition of Fc-NCNT and FePc-NCNT from EDX 90

Table 15 Summary of the important performance indicator of ORR. 92

Table 16 Kinetic current density of Fc-NCNT and FePc-NCNT at different potentials. 93

Table 17 Oxygen electrode activities. 105

Table 18 Parameters evaluated from fit of EIS in zinc-air battery single cell mode 108

List of abbreviations, symbols and nomenclature

ORR	Oxygen reduction reaction
Pt/C	Carbon supported platinum
NPMC	Non-precious metal catalyst
NCM	Nitrogen-doped carbon material
NCNT	Nitrogen-doped carbon nanotube
OER	Oxygen evolution reaction
TPB	Triple phase boundary
PTFE	Polytetrafluoroethylene
PEMFC	Polymer electrolyte membrane fuel cell
AFC	Alkaline fuel cell
CNT	Carbon nanotube
SWNT	Single-walled carbon nanotube
DWNT	Double-walled carbon nanotube
MWNT	multi-walled carbon nanotube
CVD	Chemical vapour deposition
SEM	Scanning electron microscopy/microscope
TEM	Transmission electron microscopy/microscope
EDX	Energy dispersive X-ray spectroscopy
SAED	Selected area electron diffraction
EELS	Electron energy loss spectroscopy
HR-TEM	High resolution TEM
XRD	X-ray diffraction

XPS	X-ray photoelectron spectroscopy
HR-XPS	High resolution XPS
TGA	Thermogravimetric analysis
LSV	Linear scan voltammetry
K-L	Koutecky-Levich
CV	Cyclic voltammetry
EDA	Ethylenediamine
Py	Pyridine
Fc	Ferrocene
EDA-NCNT	NCNT synthesized from EDA/Fc mixture
Py-NCNT	NCNT synthesized from Py/Fc mixture
HWP	Half wave potential
DAP	1, 3-diaminopropane
DAB	1, 4-diaminobutane
EIS	Electrochemical impedance spectroscopy

1 Introduction

Energy conversion and storage are indubitably great challenges of the modern society. The ever-increasing demands for energy resulting from the growing population, needs for personal transportation, and wide-spread use of microelectronic devices have generated global interests in novel energy technologies to integrate affordable energy production, easy storage, and environmental sustainability. Unfortunately, the current energy technologies cannot simultaneous satisfy these requirements. In the aspect of personal communication and computing, the advancement in the processing power of microelectronic devices, and the implementation of novel communication technologies (i.e., 3-Generation, or 4-Generation networks) demands high energy density, safe, reliable and affordable power sources[1]. In the aspect of personal transportation, complete reliance on fossil fuel is depleting the oil supply at an alarming rate; meanwhile, the waste gases from gasoline combustion aggravate environmental pollution[2, 3]. As a result, a global movement in carbon reduction and a search for next generation energy conversion and storage technology are gaining tremendous momentum.

Electrical energy storage can be achieved via different technologies. Traditionally, pumped hydro is the preferred choice for energy storage; however, the site specific nature and high capital costs greatly limit it to large-scale applications[4, 5]. Emerging technologies such as wind power harvest shares similar climate constraints making it unsuitable for delocalized energy storage[6-8]. In comparison to the previously mentioned technologies, electrochemical energy storage presents an attractive solution for mobile energy storage—an integral component of our rapidly expanding modern society[9, 10]. Electrochemical conversion technologies can offer low or

zero carbon emission, high efficiency, and excellent energy sustainability[9]. Battery is one of the most prominent electrochemical energy storage methods[10-12]. Batteries are considered closed systems where the two electrodes are the charge transfer media and constitute the active masses during the redox reactions. The unique characteristic allows a large selection over the composition of electrodes to offer great flexibility in terms of achieving different battery voltages. Such versatility allows one to select the best battery chemistry to target specific purpose—portable, mobile or stationary applications[10-13]. Additional advantages of battery include having a wide range of operation temperature, simple design (i.e., no auxiliary units such as pump or filters), and the capability to deliver high current pulses[13, 14]. As a result of these attractive features, batteries have enjoyed market dominance in personal electronics and are continuing to experience great success over other electrochemical storage technologies. Recently, battery technologies have been in the spotlight for the electrification of automobiles due to growing concern over carbon emission and the sustainable development in the area of personal transportation[2, 3, 15]. One of the most promising battery systems is the lithium-ion battery, which has demonstrated high cycle capability, energy efficiency, and energy density suitable for portable electronics applications[12, 16, 17]. Despite this great success, adapting the lithium-ion battery to the massive automobile market presents daunting challenges. The primary obstacle faced by the current battery technologies is the unsatisfactory storage capacity which restricts the range of practical electric vehicles. The energy density of the lithium-ion battery ranges from 100-200 $Whkg^{-1}$, which is significantly lower compared to the 1700 $Whkg^{-1}$ achievable by the gasoline used in present day automobiles[18]. The principle limitation to the storage capacity of lithium-ion battery is the intercalation chemistry of the negative and positive electrodes[19-22]. In

particular, utilization of irreversible and non-sustainable intercalation compound in the positive electrode greatly reduces energy density and significantly increases battery cost[21, 23].

A potential solution to the existing technical hurdles is metal-air battery which has attracted significant international attention owing to the extremely high energy density, reduced costs and environmental benignity[24-31]. Additionally, selection of different metal anodes allows to tailor the energy storage capacity from hundreds to tens of thousands kW for targeting specific areas of applications such as portable electronics or electric vehicles. These extraordinary characteristics of metal-air battery are extremely appealing for future sustainable development. Currently, zinc-air battery and lithium-air battery demonstrating theoretical specific energy density of 1312 $Whkg^{-1}$ and 13124 $Whkg^{-1}$, respectively, are in the spotlight as promising candidates for electric vehicle applications[3, 18, 29, 32]. However, a plethora of technical hurdles must be surmounted. One of the greatest obstacles is the air electrode in the metal-air battery, which not only determines battery performance and lifetime, but also contributes to a significant cost of the battery[18, 33, 34]. A crucial component of the air electrode is the oxygen evolution (OER) and reduction reaction catalysts, which can significantly facilitate the rate of these reactions[30, 33-36]. For metal-air batteries, catalysts ranging from precious metals (or metal alloys)[37-45] and metal oxides[46-57] supported on carbon materials have been investigated. Despite demonstration of moderate activity and stability in metal-air battery, the cycle efficiency and cycle life of batteries are hindered by carbon oxidation of these catalysts during battery charge and discharge.

The goal of this report is to target the lack of affordable, active and stable ORR catalyst—currently the major bottleneck in metal-air battery performance and commercialization. An initial overview of the metal-air battery technology including specific details on operation principles,

current developments and technical challenges will be provided to set the stage for later discussion on catalyst development and evaluation. Subsequently, potential ORR catalysts for metal-air battery will be discussed and the novel catalyst development is hypothesized. Experimental methods on catalyst synthesis and characterization will also be described followed by a series of five investigations on the novel catalyst. In the first study, the synthesis of novel catalyst and the performance compared to commercial ORR catalyst are presented. The results from the first study open up further questions regarding fundamentals of catalytic activity which will be discussed in the second, third and fourth investigations. The final investigation evaluates the performance of the novel catalyst in a prototype zinc-air battery.

1.1 Metal Air Battery

The first metal-air battery was developed by Leclanche in 1868 using carbon supported manganese dioxide as air electrode. In 1932 a more modern design of metal-air battery was developed by Schudmacher[58]. In Figure 1, the energy storage domains of different electrochemical device is defined according to the Ragone Plot[14]. Compared to other electrochemical devices, the battery displays specific power comparable to the fuel cells from 8-200 $Whkg^{-1}$. With respect to the specific energy, the battery technology spans from 10-500 $Whkg^{-1}$ comparable to electrochemical capacitors. The large energy storage domain of the battery systems imparts flexibility towards mobile power applications.

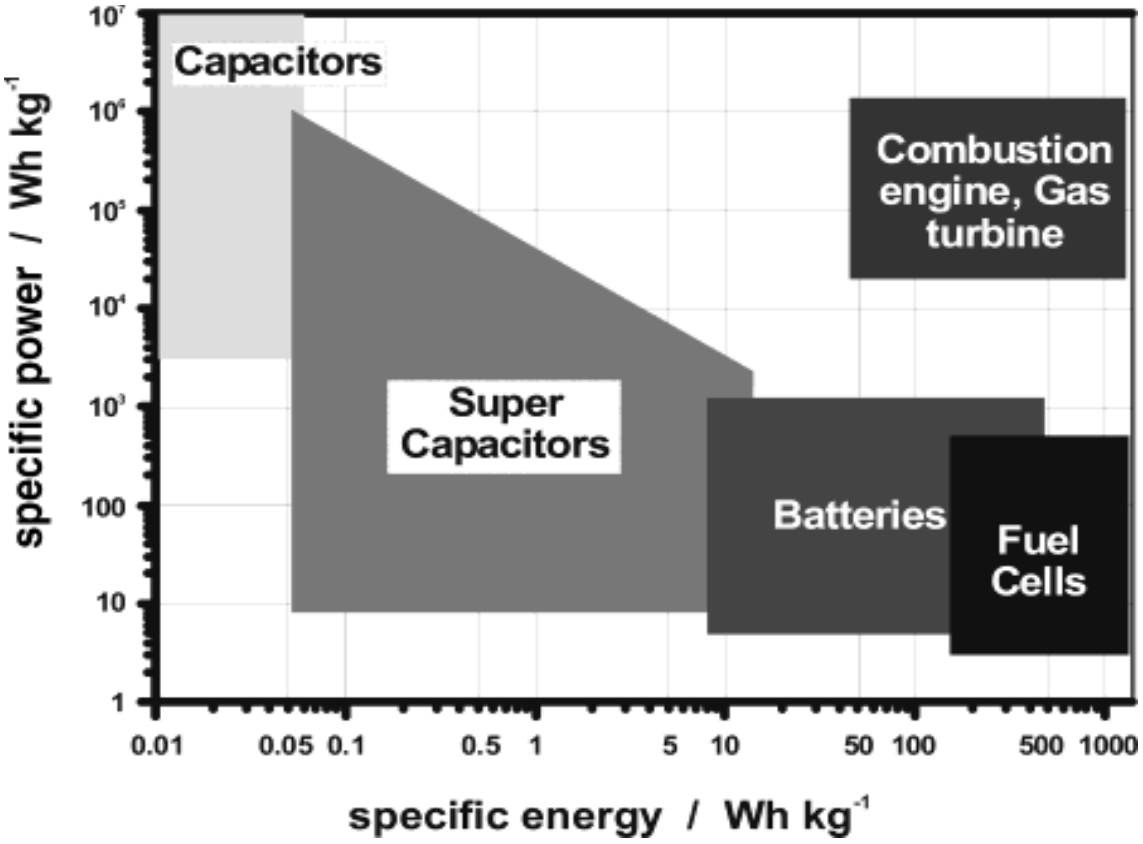

Figure 1 Regone plot showing the energy domain of electrochemical storage technologies. Reprinted from [14], Copyright 2004 with permission from American Chemical Society.

Amidst the different battery systems, metal-air battery is the category that shows the highest energy density as evident from Figure 2.[59] This advantage of metal-air battery comes from the distinguishable characteristic where the air electrode active mass (oxygen) is not stored in the system. Comparing to traditional battery systems, such as lead acid and lithium ion battery, the metal-air battery displays anywhere from 3-20 times higher theoretical specific energy.[60] In addition, the metal-air battery shows a flat discharge voltage[61-65], long shelf life[65-68], environmentally benignity[24, 59, 60, 67, 69], low cost (on metal basis)[24, 59, 67, 69] and the independence of capacitance on load cycle and temperature.[60]

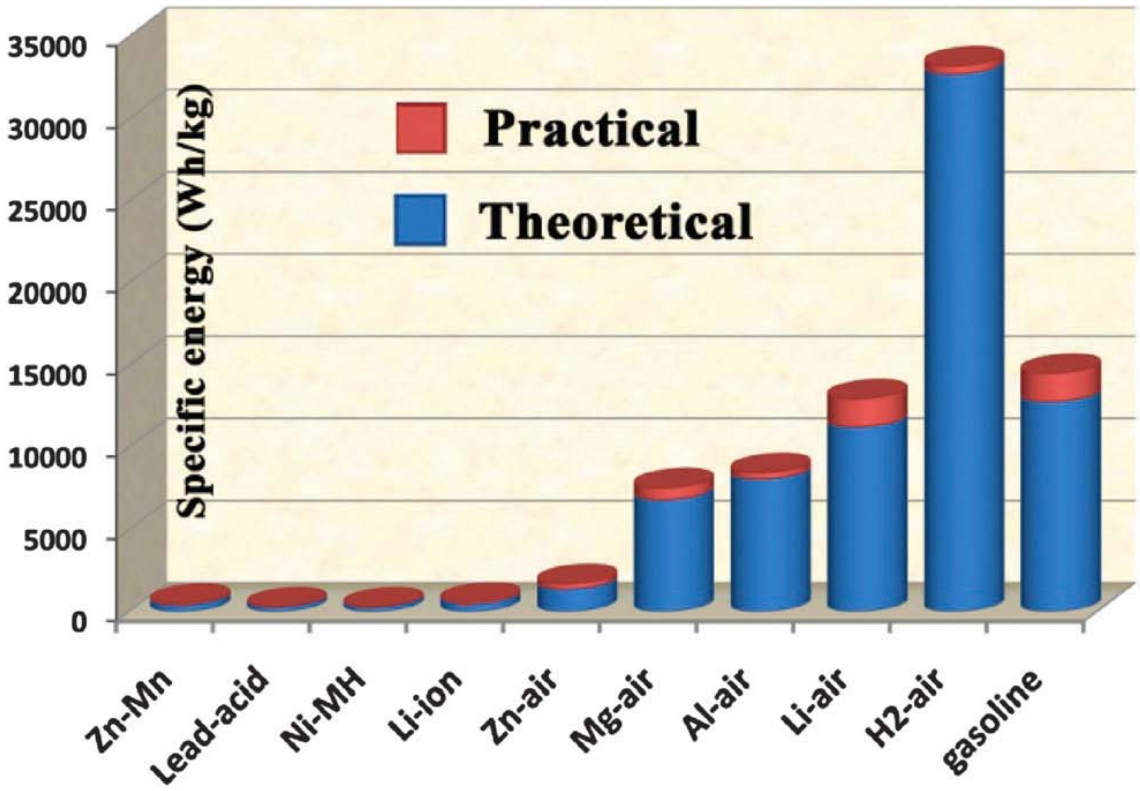

Figure 2 Specific energy density of different battery systems in comparison to gasoline. Reprinted from [58], Copyright 2012, with permission from Royal Society of Chemistry.

The generality of metal-air battery allows the choice of different metals to be used leading to different values of theoretical specific energy.[59, 60] In general, the metal-air battery operates in neutral or alkaline electrolyte where the metal oxidizes at the anode providing electrons that travel through the external circuit to participate in the reduction of oxygen at the cathode. The metals that have been considered for metal-air battery and their electrochemical characteristics are listed in Table 1.

Table 1 Characteristics of metal-air battery.[60]

Metal Anode	Electrochemical equivalent of	Theoretical battery voltage	Theoretical specific energy	Practical operative

	metal (Ahg^{-1})	(V)	($Whkg^{-1}$)	voltage (V)
Li	3.86	3.4	13124	2.4
Ca	1.34	3.4	4556	2.0
Mg	2.20	3.1	6820	1.2-1.4
Al	2.98	2.7	8046	1.1-1.4
Zn	0.82	1.6	1312	1.0-1.2
Fe	0.96	1.3	1248	1.0

Based on the electrochemical equivalent of metal, the principle advantage of using lithium—the lightest and most metal is the high theoretical specific energy of 13124 $Whkg^{-1}$ and high battery voltage of 3.4 V. These characteristics offer very high power and specific energy. However, lithium-air battery is still in the infancy of development whereby the irreversible loss of capacity, lacks of stable air electrode materials along with metal availability, cost, and safety concerns render large scale commercialization premature.[2, 18, 33, 59, 60, 63, 65, 70] Calcium, magnesium, and aluminum have also attracted attention due to the highly energy dense nature. However, high cost and problems regarding anode polarization, instability, safety and parasitic corrosion have prohibited the development of commercial products[24, 59, 60, 70]. Although magnesium-air and aluminum-air battery have found some military application for underwater propulsion.[60]

Similar to the previously mentioned metals, zinc is also very energy dense, showing an electrochemical equivalent of 0.82 Ah/g and it is the most electropositive metal that can be electrodeposited.[32, 60, 62, 67, 68] Further advantages include relatively good stability in alkaline media, low cost, environmental benignity and high abundance.[32, 60, 62, 67, 68] It is estimated that 21 months of global zinc production would be sufficient for the production of 1 billion 10 kW zinc-

air battery to power all of the automobiles in the world. For this reason, zinc-air battery is, at the current stage of development the most promising metal-air battery to be commercialized for multiple markets. However, to scale up the application of zinc-air battery in the commercial markets including portable electronics and electric vehicles, battery performance and lifetime require further improvement and cost reduction. To optimize the battery performance and lifetime, the fundamental principles behind the operation of metal-air battery need to be understood.

1.1.1 Operation principles of zinc-air battery

Two electrochemical reactions constitute the energy storage/conversion in a metal air battery—the ORR at the air electrode; and the metal oxidation at the anode. The ORR half-cell reactions taking place during battery discharge can be written as,

$$O_2 + 2H_2O + 4e \leftrightarrow 4OH^- \qquad E_{cathode}{}^o = +0.401\,V \qquad (1)$$

In equation 1, e denotes electron and E^o denotes the theoretical half-cell voltage according to thermodynamics at standard conditions. The source of oxygen is from the ambient air, thus the only negative mass in the metal-air battery is the metal electrode which oxidizes during battery discharge according to the below reaction,

$$M \rightarrow M^{n+} + ne \qquad E^o_{anode} = depend\ on\ the\ metal \qquad (2)$$

In equation 2, M denotes the specific metal used in a particular metal-air battery system, and the number n depends on the change in the valence of the specific metal in consideration. Evidently, the theoretical half-cell voltage is specific to the selection of metal in this reaction. The theoretical battery voltage can be calculated by the following equation,

$$E^o{}_{battery} = E^o_{cathode} - E^o_{anode} \qquad (3)$$

It should be noted that in the case of a rechargeable metal-air battery, the cathode and anode reverses during battery charge. Under such condition, the metal electrode becomes the cathode, and the air electrode becomes the anode.

One of the most promising metal-air batteries capable in delivering excellent power and energy density is zinc-air battery. Owing to the attractive features of zinc, this type of air battery is currently available on the market in the form of non-chargeable button cells. There are three components in the zinc air battery, the zinc electrode, also called negative electrode; the air electrode also known as the positive electrode; and the separator. These components are illustrated in Figure 3. The overall battery reaction of a zinc-air battery in alkaline condition is described by Figure 3. During battery discharge, zinc metal reacts with hydroxyl ions (OH^-) in the electrolyte which leads to the formation of zincate molecules ($Zn(OH)_4^-$). Concurrently, two electrons are released which travel through the external circuit to reduce the oxygen molecules (from ambient air) at the air electrode. The reaction with oxygen, with the aid of catalysts takes place at the triple phase boundary (TPB)—a reaction zone where electrolyte, catalyst particles and dissolved oxygen gas pockets interface[60]. The ORR reaction on the air electrode replenishes the hydroxyl ions in the electrolyte, while producing some by-products including water and oxygen gas molecules. With increasing concentration of $Zn(OH)_4$, the electrolyte becomes supersaturated and $Zn(OH)_4^-$ dissociates into zinc oxide (ZnO). By combining the negative and positive electrode reactions, the overall theoretical voltage for the zinc-air battery is 1.6 V.

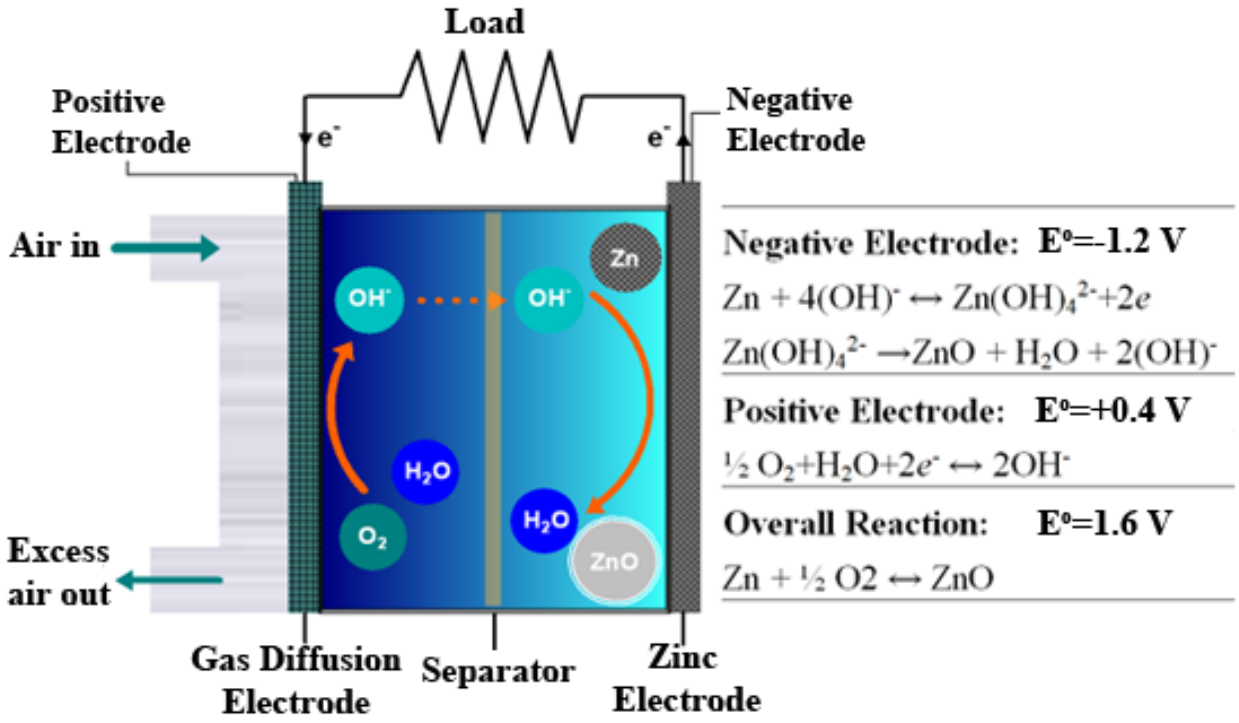

Figure 3 Schematic of a zinc-air battery.

Zinc electrode

Zinc-air batteries employ zinc metal as the active mass at the anode. As a result, by increasing the surface area of the zinc electrode, more efficient reaction of zinc with the electrolyte is promoted which can lead to improved battery performance[70]. Using different morphologies of zinc anodes, including zinc particles[71], zinc dendrites[71], and zinc fibre[72], different battery performances have been recorded reflecting the feasibility of this approach. Figure 4 shows examples of zinc electrode morphology generated via electrodeposition method.

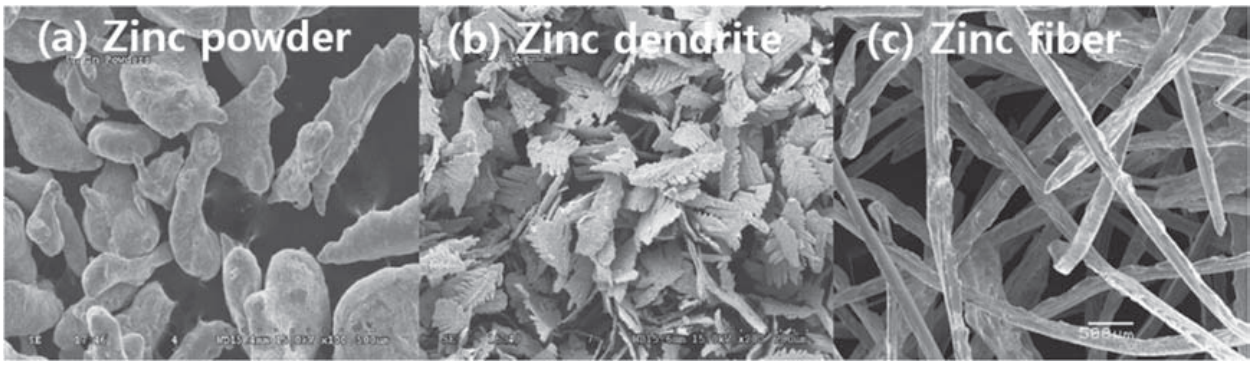

Figure 4 Different morphology of zinc electrode.[71, 72]

More advance structure of zinc electrode can be obtained via the use of surfactants which will act as soft templates to direct the morphological growth during the deposition of zinc. Some example of surfactant assisted electrodeposition of zinc electrode is shown in Figure 5.[73]

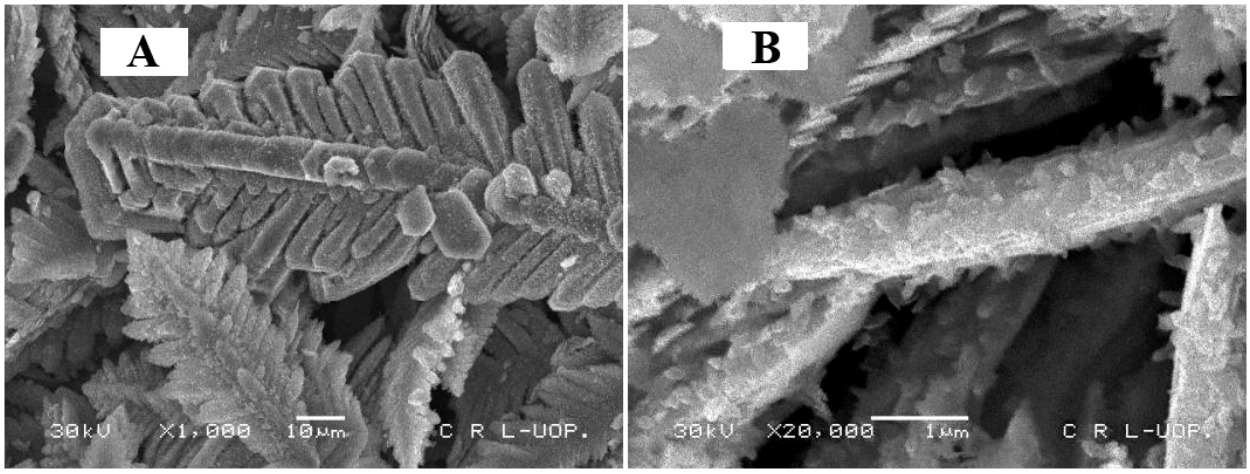

Figure 5 Surfactant assisted deposition of zinc electrode.[73]

Besides controlling the morphology of the zinc electrode, the actual composition can be altered via alloying or surface coating to further improve the electrode performance[74-76]. For example, zinc can be coated with mercury and copper to improve the electrode conductivity and aid in re-precipitation of metallic zinc, respectively. Alloying of zinc with other metals such as indium, nickel, palladium and cadmium can result in the reduction of parasitic corrosion[76]. Additionally

coating zinc anode with Li_2O-$2B_2O_3$ and polymer can improve stability in alkaline conditions[77, 78].

Separator and electrolyte

The principle function of the separator is to transport OH^- from the air electrode to the zinc electrode. Some of the most important requirements for separators are listed in Table 2.

Table 2 Characteristics of an ideal separator for zinc-air battery[70]

Ionic conductivity	High hydroxyl ion conductivity
Electrical conductivity	Insulating to the transport of electrons
Stability	Stable in alkaline conditions and against charge/discharge cycles
Porosity	Properly engineered porous network to allow for hydroxyl ion transport Fine pore structures to absorb and retain electrolyte
Pore size	Selectively permeating the hydroxyl ions but not zinc cations

There are two classes of electrolyte for zinc-air battery one is the liquid electrolyte the other being solid electrolyte. The latter is a newly emerging research area which exploits the unique properties of certain polymer such as polyamide, whereby OH^- transportation is assisted by the functional groups present on the polymer chains. The advantages of having an anion conducting polymer electrolyte are to reduce the potential leakage associated with liquid electrolyte[79]; carbonate formation[79]; higher ion concentration and improved performance[70]. However, achieving high anion conductivity and sufficient stability requires further efforts. As a result, most zinc-air batteries under research and development or currently in the market uses only liquid electrolyte. The viscosity of the electrolyte can be increase to reach the consistency of

slurry or gel to slow down the drying out of the electrolyte. The commonly used alkaline salt includes sodium hydroxide (NaOH), potassium hydroxide (KOH), lithium hydroxide (LiOH) and ammonium chloride (NH_4Cl)[70]. Among these electrolytes, potassium hydroxide is most commonly used owing to the superior ionic conductivity of the potassium ion (73.50 $\Omega^{-1}cm^2$/equivalent)[70, 80]. The concentration of the KOH is also critical for battery operation. Lower concentration reduces the amount of ions available for reaction and increases electrolyte resistance; meanwhile, extremely high salt concentration leads to high viscosity which retards ion transport and may lead blockage of oxygen transport pathways. The optimal concentration of KOH for zinc-air battery is around 30%[68].

Air electrode

Unlike the conventional battery electrode where the active mass constitutes the majority of the electrode, the air electrode draws the active mass from ambient air. Consequently, the air electrode in a zinc-air battery requires the ability to carry out ORR, allow air access and conduct electrons simultaneously. The most prominent design for the air electrode in zinc-air battery is similar to the gas diffusion electrode found in the polymer electrolyte membrane fuel cell. The state of the art gas diffusion electrode is an integration of several types of carbon based materials bound together by polytetrafluoroethylene (PTFE) resulting in a porous gas permeable electrode[61, 64, 81]. Figure 6 illustrates the structure of the air cathode and the functions of the different components of the air electrode. In the cartoon drawings enclosed by red dashed-line boxes, the solid black lines represent the carbon fiber. The grey colour with white hash-lines represents the metal mesh. The solid black circles represent fine carbon powder. The solid yellow circles represent catalyst particles. The light blue dash-arrows represent flow of oxygen

through the gas diffusion electrode and the metal mesh. The green dash-arrows represent the flow of electrons in the metal mesh to the catalyst layer. The images beneath the cartoon drawings represent the respective electron micrographs.

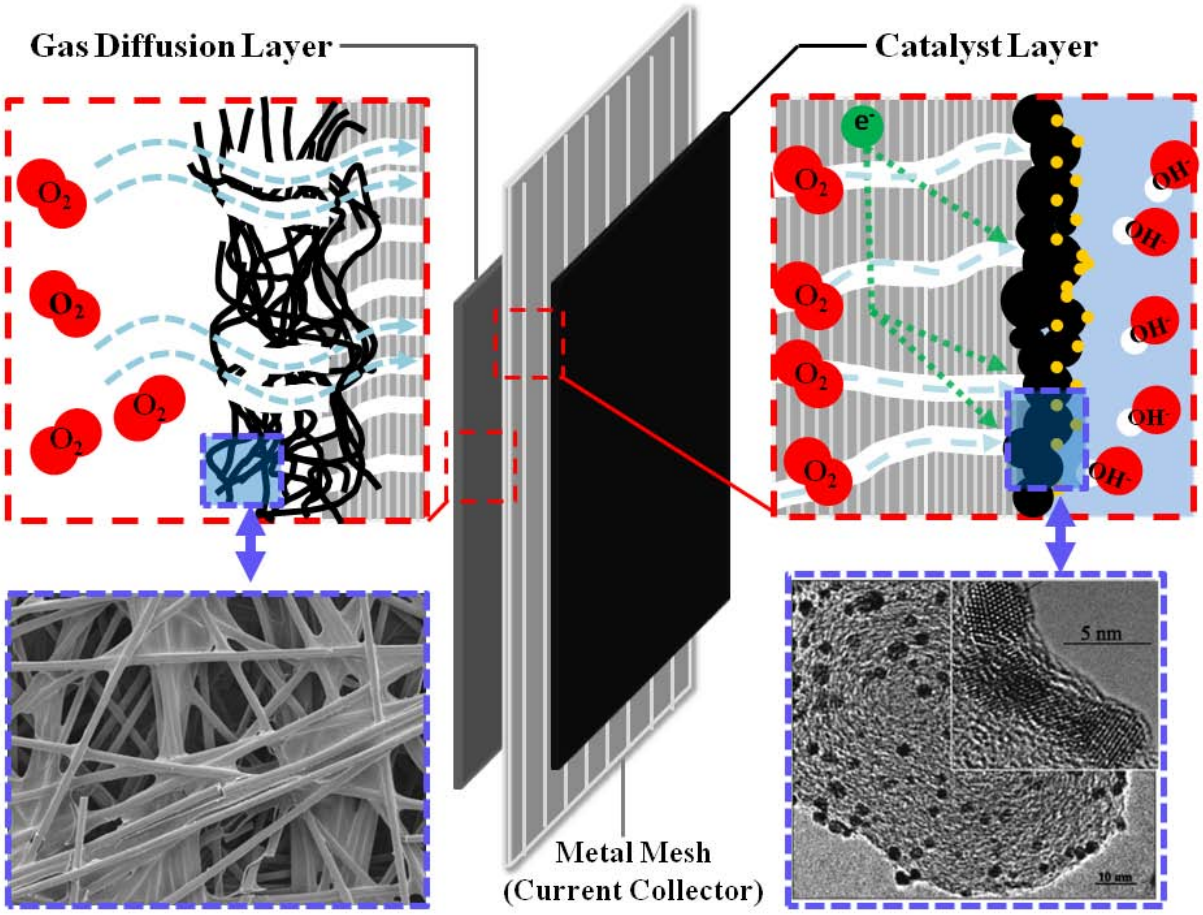

Figure 6 Structure and function of a typical air electrode for zin-air battery.

The air electrode is usually composed of three components, a gas diffusion layer, a current collection and a catalyst layer[35, 82-85]. The gas diffusion layer is side of the air electrode that faces the outside environment and it consists of carbon fibers bond together with PTFE polymer. Due to the property of carbon fiber and PTFE binder, the gas diffusion layer is hydrophobic which

promotes air transport. At the same time, the hydrophobic nature prevents electrolyte from penetrating the gas diffusion layer and leak from the battery. Next to the gas diffusion layer is the metal mesh, the main function to conduct electrons for the electrochemical reaction. The last component of the air electrode is the catalyst layer which often consists of catalysts particles, or other morphologies, supported on high surface area conductive carbon. The selection of high surface area carbon results in two advantages. First advantage is the creation of micropores which allows the formation of gas pockets leading to the formation of TPB for ORR. Second advantage is the hydrophilic property arises from the fine texture and microporosity which promotes electrolyte wetting of the catalyst layer.

The most critical component of the air electrode is the ORR catalyst itself. The ORR is very complex, it involve multiple molecular adsorption-desorption events; plethora of elementary reaction steps; several reaction pathways; and formation of different reaction product, some of which are highly reactive radicals. In alkaline solutions, ORR is believed to proceed via four-electron transfer reaction (equation 1) and two-electron transfer reaction according to equation 4[86].

$$O_2 + H_2O + 2e^- \leftrightarrow HO_2^- + OH^- \qquad E^0 = -0.065\,V \qquad (4)$$

The two-electron transfer reaction is the less efficient alternative of the ORR as it produces hydroperoxide ion ($HO2^-$) and use only two electrons. Fortunately, the HO_2^- can be reduced further to hydroxyl ions by equation 5[86].

$$HO_2^- + H_2O + 2e^- \leftrightarrow 3OH^- \qquad E^0 = 0.867\,V \qquad (5)$$

This reaction presents a large overpotential and a catalyst is required to improve the kinetics and efficiently couple this reaction to the one in equation 4. As a result of the two possible reaction

pathways, two solutions are possible for ORR catalysis. First solution involves the direct four-electron reduction of the oxygen molecule and second approach involves the use of two catalysts, where the first one reduces the oxygen according to equation 4, and a second catalyst to complete the reaction by equation 5. A plethora of catalyst exists for ORR. The most active ORR catalysts belong to precious metals such as platinum, palladium, and silver. Of these catalysts, uniform nanostructures of platinum and platinum alloys (PtNi, PtFe, PtCo) supported on high surface area carbon represent the state-of-the-art technology for ORR catalyst[37-45]. Other catalyst such as chalcogenides[87, 88], transition metal alloys and oxides[46-57] have been studied extensively; however, the ORR activity and stability are inferior compared to that of platinum catalysts.

1.1.2 Technical challenges

Cost reduction and performance improvement are two aspects requiring continuous development for zinc-air batteries. Besides this however, there exists other issues that negatively affect zinc-air battery performance and lifetime. The major challenge associated with the metal electrode relates to the thermodynamic stability of the metal in aqueous electrolyte, whereby they reaction with water to form hydroxide and hydrogen gas according to the reaction below[60],

$$M + nH_2O \rightarrow M(OH)_n + \frac{n}{2}H_2 \qquad (6)$$

This reaction is known as the parasitic corrosion reaction, or self-discharge reaction which greatly degrades the columbic efficiency of the anode[89]. As for the separator, zinc cation can permeate through the separator and reach the air electrode side which can lead to reduction of the battery capacity and contamination of the air electrode catalysis and lower battery performance. With regards to the electrolyte, the use of potassium hydroxide, although showing high ion

conductivity, is susceptible to the carbonation by the CO_2 from the air. The carbonation reactions proceed following the below reactions[90, 91].

$$CO_2 + OH^- \rightarrow CO_2^{-3} + H_2O \qquad (7)$$

$$CO_2 + 2KOH \rightarrow K_2CO_3 + H_2O \qquad (8)$$

The major challenge faced by the air cathode is the sluggish ORR kinetics in conjunction with large activation energy for the reaction which can be tackled using an effective catalyst. However, the seemly simply ORR involves a collection of elementary steps and alternative reaction pathways making the task difficult to achieve. Besides the direct four-electron reaction pathway showed in equation 1, two electron reaction pathway leading to the production of hydroperoxide (equation 4 and 5) followed by further reduction or chemical decomposition (equation 9).

$$HO_2^- \leftrightarrow \frac{1}{2}O_2 + OH^- \qquad (9)$$

The production of hydroperoxide can affect the catalyst performance and the chemical decomposition can lower the total energy extracted from the reaction. Besides the air electrode and metal electrode capacity loss, other contributions to the loss of performance are showed in Table 3.

Table 3 Factors affecting the performance of metal-air battery[60]

Performance degradation	**Description**
Polarization	• Large diminish in voltage with increasing current • Limits to low- to mid-power requirement applications
Electrolyte carbonation	• Carbon dioxide in air reacts with electrolyte forming carbonate • Carbonates crystallization leads to:

	1. Blockage in porous air electrode 2. Mechanical damages to battery 3. Decrease electrolyte conductivity
Water Transport	• Loosing water leads to battery drying-out, premature failure • Gaining water leads to dilution of electrolyte and pore flooding

Among all the technical challenges faced by zinc-air battery, the air cathode catalyst is the upmost critical obstacle preventing the technology from being commercialized. The air cathode constitutes about 30-50 % of the total cost of the zinc-air battery[31, 34, 92]. Within this cost, about 80 % of the cost is associated with the use of precious metals such as silver, silver oxide and platinum-based catalysts[31, 34, 92]. As a result, the catalyst alone will account for approximately 24-40 % of the total cost of the zinc-air battery. In addition, air electrode catalyst greatly influences the battery performance as the ORR is the bottleneck in the electrochemical reaction of the battery. The sluggish ORR kinetics compared to the relatively facial zinc oxidation places great constraint to the maximum power output of the device. Furthermore, the radical (hdyroperoxidse or superoxide radicals) created during the ORR synthesis can lead to catalyst degradation which will have great impact on the overall lifetime of the zinc-air battery. As a result, the mainly purpose of this thesis is to advance the understanding of ORR catalysis in alkaline medium on carbon based materials and to develop affordable, active and stable catalyst for ORR.

1.2 Nitrogen-doped carbon nanotube

One emerging class of catalyst for ORR is the nitrogen-doped carbon materials. These materials have been showing excellent activity and stability in acid and alkaline conditions for polymer

electrolyte membrane fuel cells (PEMFC) and alkaline fuel cells (AFC)[93-103]. Recently, nitrogen-doped carbon nanotubes have catch the attention of fuel cell and battery communities where superior ORR performance compared to that of carbon supported platinum was reported[93, 101, 102, 104]. This thesis is aimed to study the properties of nitrogen doped carbon nanotubes of different structural/chemical properties and their effect towards ORR catalysis.

Carbon nanotubes (CNT) were first discovered in 1991 by Sumio Iijima[105] which has since generated unprecedented interest based on the superior mechanical[106], thermal[107, 108], electrical[109], optical[110, 111] and chemical properties[112-117]. The carbon nanotubes are cylindrical-structured allotropes of carbon created by rolling up single layer, double layers and multiples layers of graphene sheet to form single-walled carbon nanotube (SWNT), double-walled carbon nanotube (DWNT), and multi-wall carbon nanotube (MWNT), respectively (Figure 7). Depending on the number of graphene sheets involve in the formation of CNT, the diameter of CNT can vary from a few nanometers to hundreds of nanometers. Meanwhile, the length of CNT ranges from several micrometers to several millimetres resulting in extremely high aspect ratio.

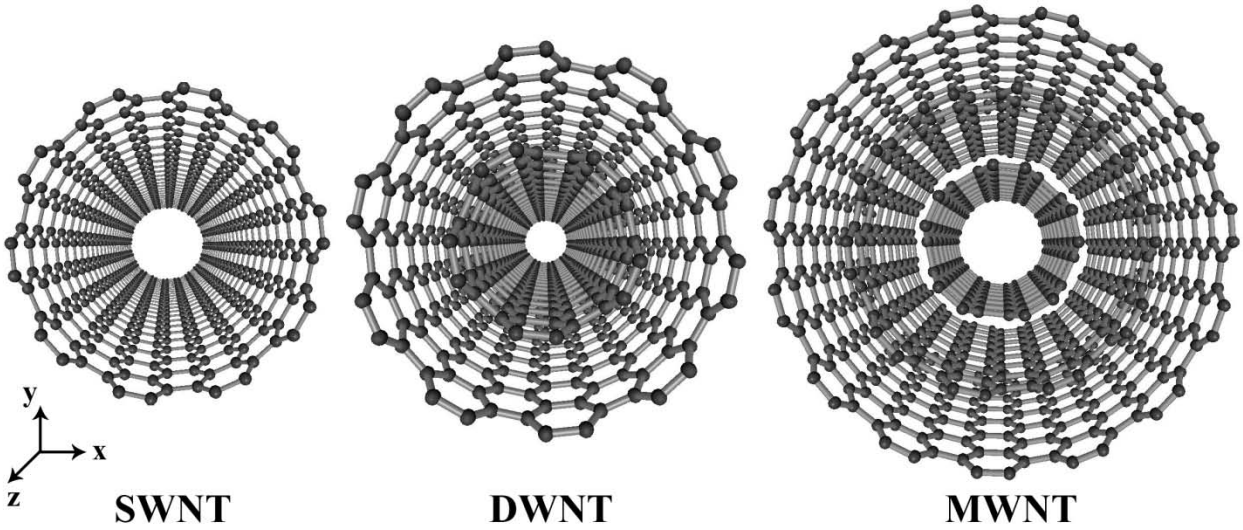

Figure 7 Ball-and-stick model of SWNT, DWNT and MWNT.

The crystal structure of the CNT is the hexagonal lattice resulting from the graphene sheets. The fold folding of these graphene sheets results in different chirality of the CNT[118]. From Figure 8, different methods of folding graphene sheet are illustrated. The vector T indicates the tubular axis; a_1 and a_2 represent the primitive translational vectors of the hexagonal lattice; and C_h denotes the chiral vector of the CNT[118]. The shaded area in Figure 8 indicates the possible chirality of a CNT, while the dashed-lines represent two unique chiralities defined as armchair and zigzag[112, 115-118].

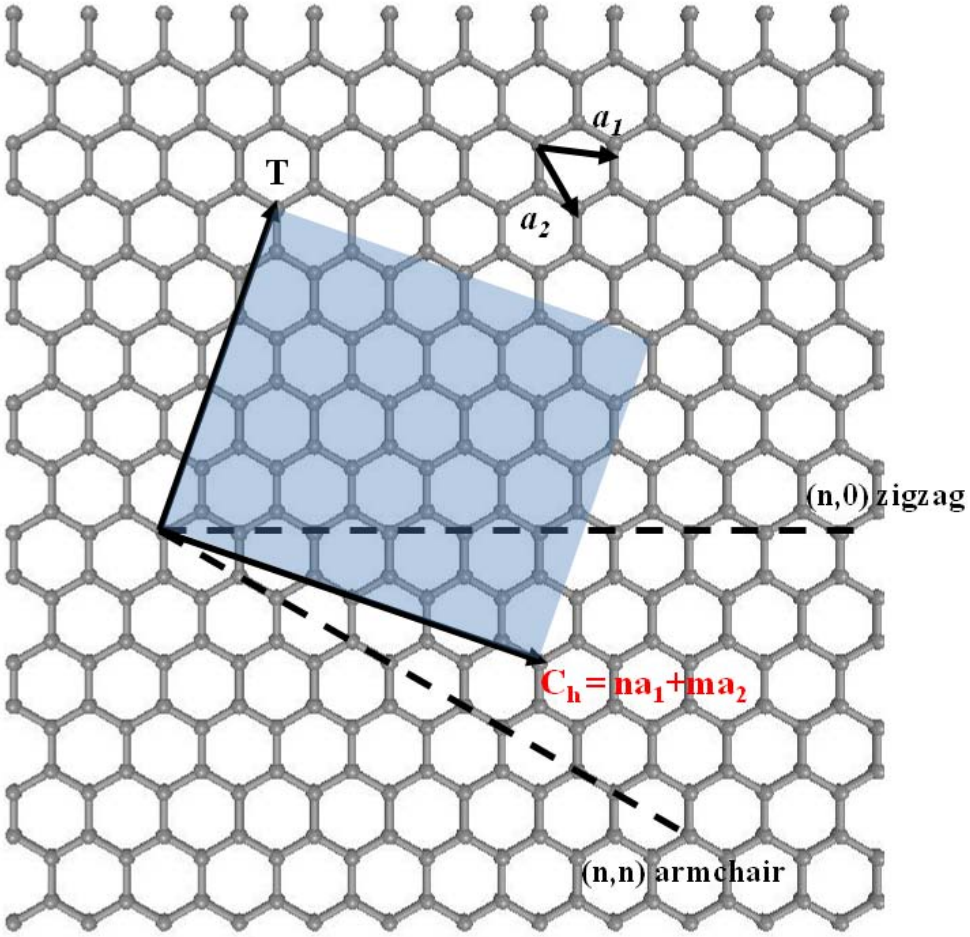

Figure 8 Hexagonal lattice of the graphitic wall in CNT.

The chirality of CNT can be easily visualized when the CNT are viewed from the side (Figure 9). Changes to the diameter and configuration of CNT can leads to drastic alternation in the properties such as from being metallic to semiconducting. In general zigzag and armchair CNT are metallic whereas the conductivity of chiral CNT depend on the chiral vector indices (n, and m) and the diameter[112, 115-117].

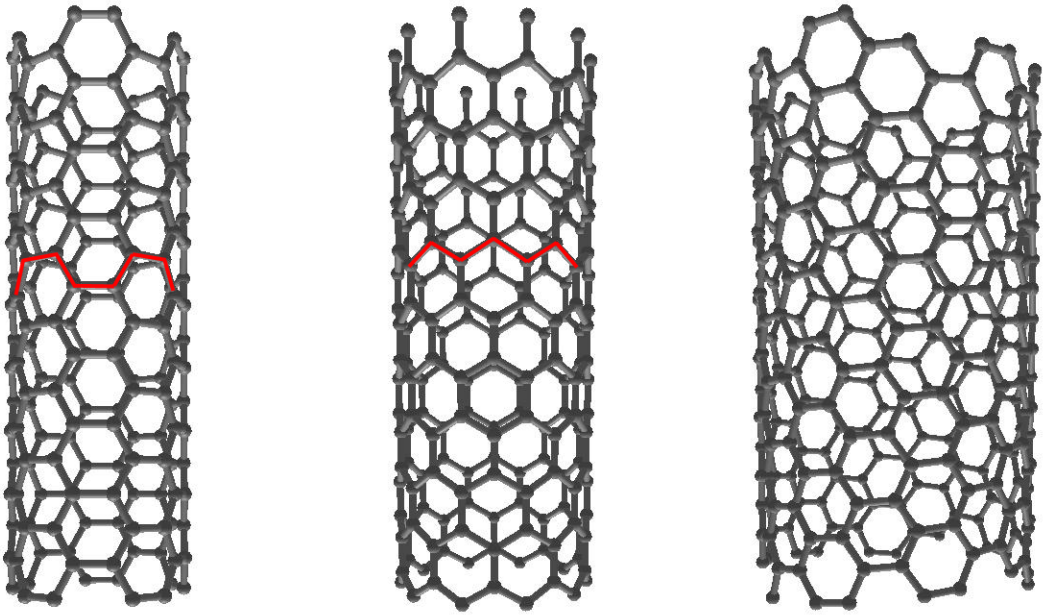

Figure 9 Chirality of CNT. The bonds in red denote the 'armchair'- and 'zigzag'-like patterns.

The thermal properties of CNT have been found to exceed that of copper by nearly an order of magnitude reaching approximately 3500 W/mK along the tubular axis due the negligible electrical resistance from scattering[107]. The thermal stability of CNT can be as high as 2800 °C in vacuum and 750 °C in air[108]. The mechanical properties of CNT have been found to be superior to stainless steel showing Young's Modulus of 0.2-0.9 TPa for MWNT and 1-5 TPa for SWNT[106]. Comparatively, stainless steel exhibits Young's modulus ranging from 0.18 to 0.21 TPa. However, the most appealing aspect of CNT towards electrocatalysis is the excellent chemical and electrical properties. The ballistic model of electron transport allows extremely high electric current density, reaching 4×10^9 A/cm^2, about 1000 greater than metals such as copper[109]. Additionally, CNT is consider to be chemical inert in acid and alkaline condition due to the stable sp2 hybridized covalent bonds. As a result of the superior properties, CNT have

been used as catalyst support for electrocatalysis. However, the inherently low affinity of CNT toward binding of dioxygen molecule renders this material inactive towards ORR catalysis. The lower affinity for dioxygen can be caused by several factors, one of them being the near neutral charge distribution at equilibrium[119, 120]. Figure 10 illustrate the end-on and side-on adsorption of dioxygen to CNT surface.

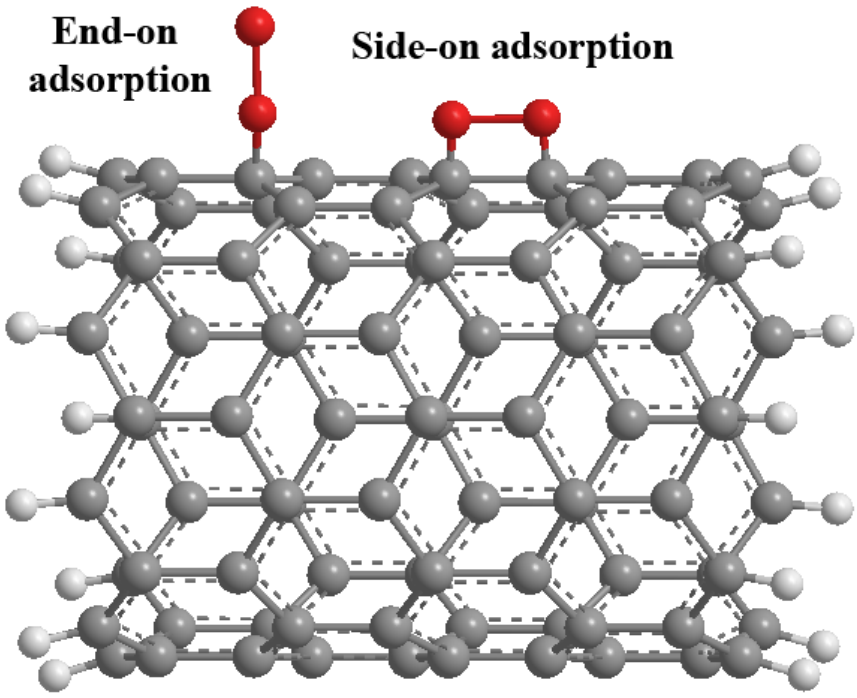

Figure 10 Adsorption of dioxygen onto the surface of (9,0)-SWNT.

The lack of charge distribution of CNT does not promote the adsorption of dioxygen. Computational studies have shown that the chemisorptions energy of dioxygen molecules on the surface of a (8,0)-SWNT is less than 0.04 eV[120]. The weak interaction results in small charge transfer between the two species (~0.01 electron)[120]. Since the ORR is an outer-sphere charge

transfer reaction where the donation of electron density and subsequent back-bonding dominate the cleavage of dioxygen bond, the small electron transfer hinders ORR catalysis by pristine CNT.

To solve this problem, heterogeneous dopants can be introduced into the graphitic network to create charge delocalization in the proximity of the dopant atoms. Different atoms can be doped into the graphitic matrix including, boron[121, 122], nitrogen[102, 123], and phosphorous [124, 125, 126]. Among these dopant, incorporation of boron leads to p-type doping and nitrogen and sulphur leads to n-type doing. Nitrogen doped carbon nanotube is of particular interest to ORR catalysis as previous studies on transition metal macrocyclic molecules have illustrated the importance of nitrogen atoms in the graphitic network towards ORR catalysis[95, 97, 98, 103]. Computational studies have elucidated the effect of nitrogen doping, whereby charge delocalization in the vicinity of the nitrogen atom leading to improved affinity for dioxygen molecule[100, 102, 126]. Additionally, the increase in delocalized charge allows for better charge transfer between the two species and more efficient back-bonding (Figure 11).

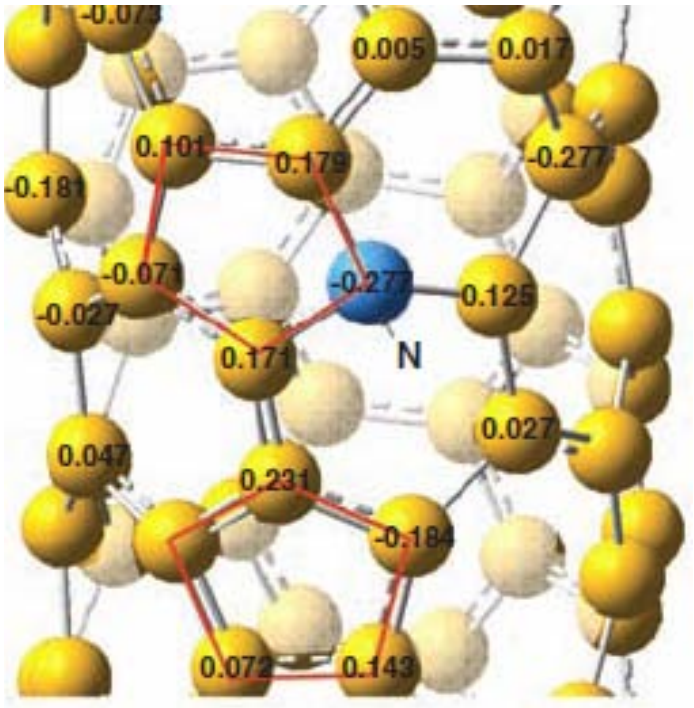

Figure 11 Charge density delocalization as a result of nitrogen doping. Reprinted with permission from [102], Copyright 2009, American Chemical Society.

Synthesis of NCNT can be achieved using the same methods adopted for their pristine counterpart. High temperature methods, such as laser ablation and arc-discharge can rapid evaporation of nitrogen and carbon precursor can lead to the formation of NCNT. Less energy intensive methods such as chemical vapour deposition (CVD) an also be used. In CVD methods, a plume containing the carbon and nitrogen precursors reacts in vapour phase and precipitates to form NCNT in a constant flow of inert gas (i.e., N_2 or Ar). In most cases, a synthesis catalyst, usually metals such as iron, nickel, and copper is required. However, recent reports on the growth of CNT on plasma treated SiO_2 surface have showed the possibility of elimination of metal synthesis catalyst. The growth of NCNT is illustrated in Figure 12[126].

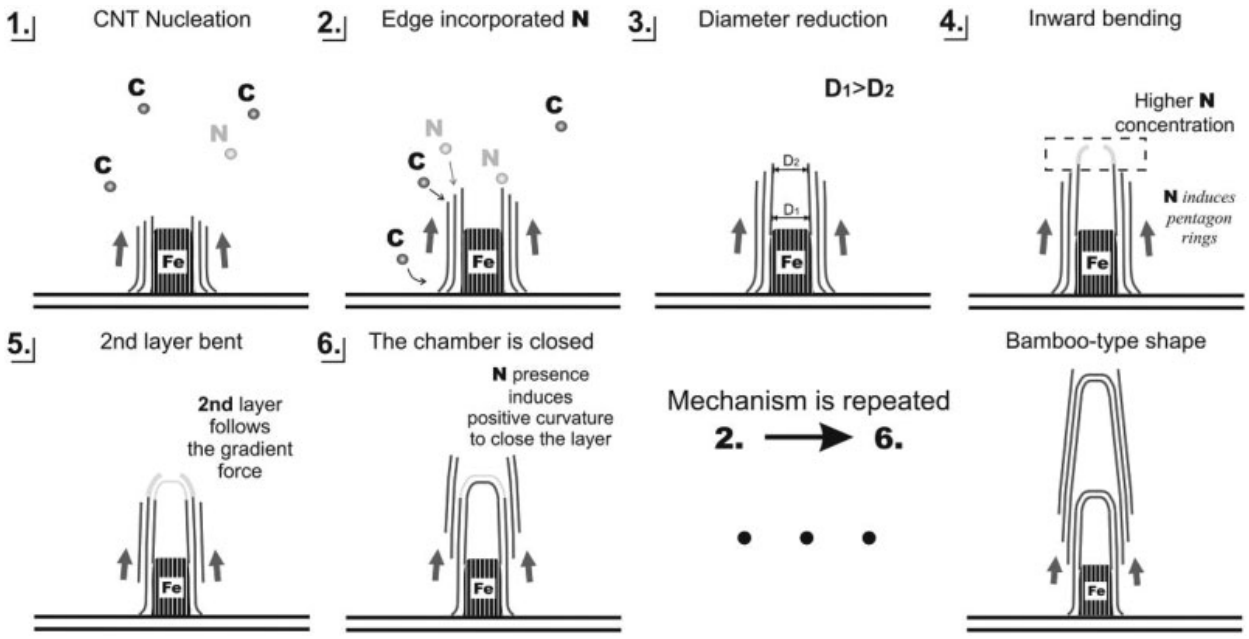

Figure 12 Growth mechanism of the NCNT by CVD method. Reprinted with permission from [126], Copyright 2008, Wiley Periodicals.

With the presence of carbon and nitrogen precursor and metal synthesis catalyst the growth of NCNT is initiated when the temperature of the CVD setup reaches the sublimation point of the precursor materials. At this point, the synthesis catalysts form into small droplets on the substrate. As the plume of precursors is carried downstream they precipitate on to the catalyst droplets, in this case it is Fe according to Figure 12. The molten Fe droplets can only accommodate limited amount of precursor before it supersaturates, at which point the carbon atoms start to self-assembly onto the surface of the catalyst droplets in hexagonal fashion. For pristine CNT only hexagonal networks will form where all the carbon atoms are connected by sp2 bonds. In the case of NCNT however, incorporation of nitrogen atoms disrupts the hexagonal network as it requires one less bond according to the octave rule. As a result, formation of penta-rings can result. Penta-rings provide negative curvature to the otherwise nearly-planar hexagonal network leading to the formation of bamboo compartments within the nanotubes (diagram on the lower

right corner in Figure 12). As a result, high nitrogen concentration can be found at the fullerene-like caps in the NCNT. A transmission electron micrograph showing the bamboo structure of NCNT is showed in Figure 13. In addition to the bamboo compartments, incorporation of nitrogen introduces localized defects and structural disorders. Different configurations of nitrogen-to-carbon bond can result depending on the local interactions of atoms. Depending on the bonding configuration, the commonly observed surface nitrogen groups in NCNT include pyrrolic, pyridinic, quaternary and pyrrolidone groups. Figure 13 illustrate the surface of NCNT with different nitrogen groups. Identifying the presence of different nitrogen groups and controlling the formation in favour of certain nitrogen groups will be critical to the ORR activity based on previous reports correlating surface nitrogen groups of carbon-based NPMC to the ORR activity.

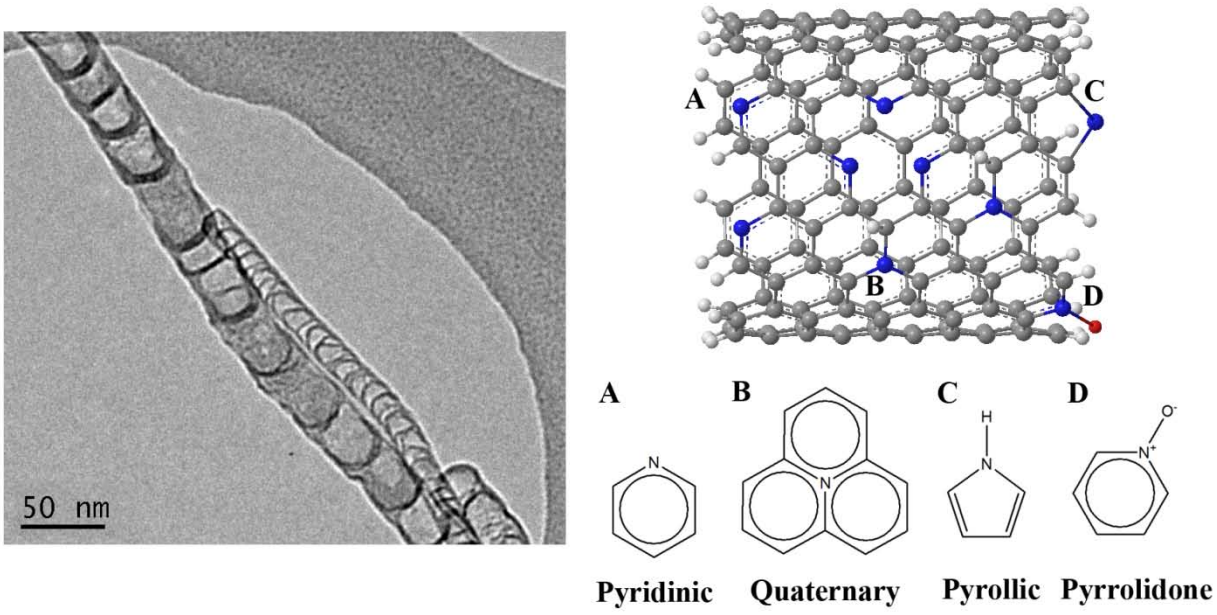

Figure 13 Left, electron micrograph of NCNT and right, schematic of NCNT.

1.3 Scope and objectives

Metal-air battery is a board subject and there are multiple aspects requiring improvement before commercialization can be realized. The scope of this study will focus mainly on tailoring NCNT properties to achieve the desirable ORR catalytic affect as oppose to conduct a complete design and analysis of air electrode or anode design. The objectives of this thesis are to report the results of a series of investigations on the fundamental properties of NCNT and the practical application of this novel material towards the ORR catalysis of zinc-air battery. To achieve these objectives, the novel approach used to synthesize the NCNT catalysts followed by detailed materials characterizations and performance evaluation will be presented. This work will provide insights regarding the correlation between NCNT properties and ORR activity as well as forming a basis for future investigation of NCNT.

2 Materials synthesis and characterization

Fundamental understanding of the catalyst structure, morphology and activity is required for the design and development of the NCNT catalyst. The synthesis methodology of NCNT is presented to establish a basis for the formation of the NCNT and the possible avenue of future improvement. Physical characterization of the NCNT is discussed in detailed in this section to provide an understanding of the materials properties and to predict the ORR activity. Electrochemical characterizations will be provided to validate the prediction and evaluate the feasibility of the novel NCNT catalyst.

2.1 Chemical vapour deposition synthesis

Chemical vapour deposition was used to synthesize the NCNT. The setup of the CVD system is shown in the figure below. Component A represents the inert gas source. Argon is the most commonly used inert gas in a CVD synthesis. Component B is the inlet tubing connecting the gas source to Component E, the heating furnace. Component C is the syringe pump and it was used to inject the carbon and nitrogen precursor solution into the heating furnace when the temperature reaches the reaction set-point. The advantage of using a syringe pump is to provide better control over the CVD synthesis. The syringe pump allows precise control over the injection rate of the precursor solution and it provides a steady feed of precursor over the duration of the synthesis. This is unlike the conventional flowing catalyst CVD synthesis where a sudden release of the precursor material in the form of a plume of gas can result when the temperature of the furnace is higher than the sublimation point of the precursor. However, the use of syringe pump requires the carbon and nitrogen precursor materials to be in liquid form.

Component D is the connection between the syringe pump and the heating furnace. Component F is the bubbler which is filled with mineral oil to trap the organic components from the exhaust gas.

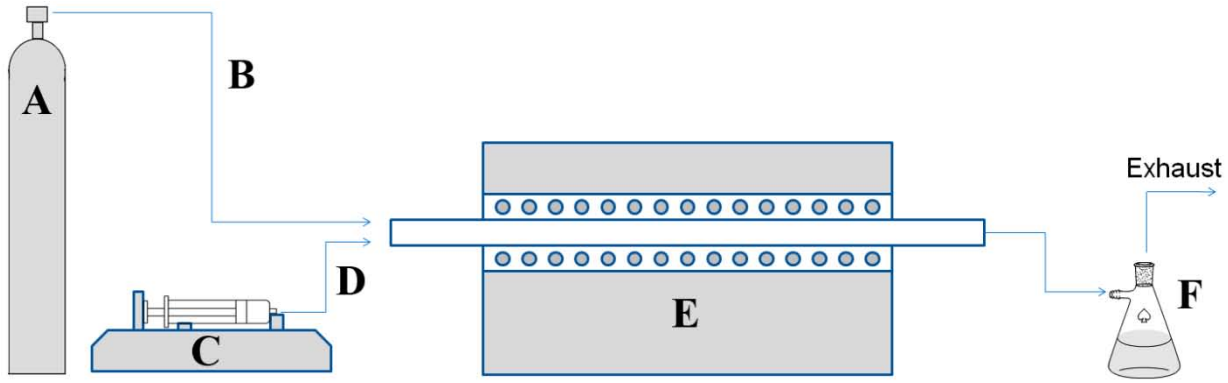

Figure 14 CVD setup used for the synthesis of NCNT.

The chemical structure of the carbon precursors, nitrogen precursors and synthesis catalysts used in the preparation of NCNT as well as the heating profile employed are showed in Figure 15. In general organic compounds were used for the NCNT synthesis since it contains the richest carbon amount. As a result, compounds such as ferrocene which was used mainly as the synthesis catalyst also contains some carbon materials which can contribute to the synthesis of NCNT. To reduce the reaction complexity, compounds containing both carbon and nitrogen atoms were selected to act as both the carbon and nitrogen precursors. For all the NCNT synthesis carried out in this series of studies, the carbon and nitrogen content are in liquid state and the catalyst can be dissolved in the precursor materials unless stated otherwise.

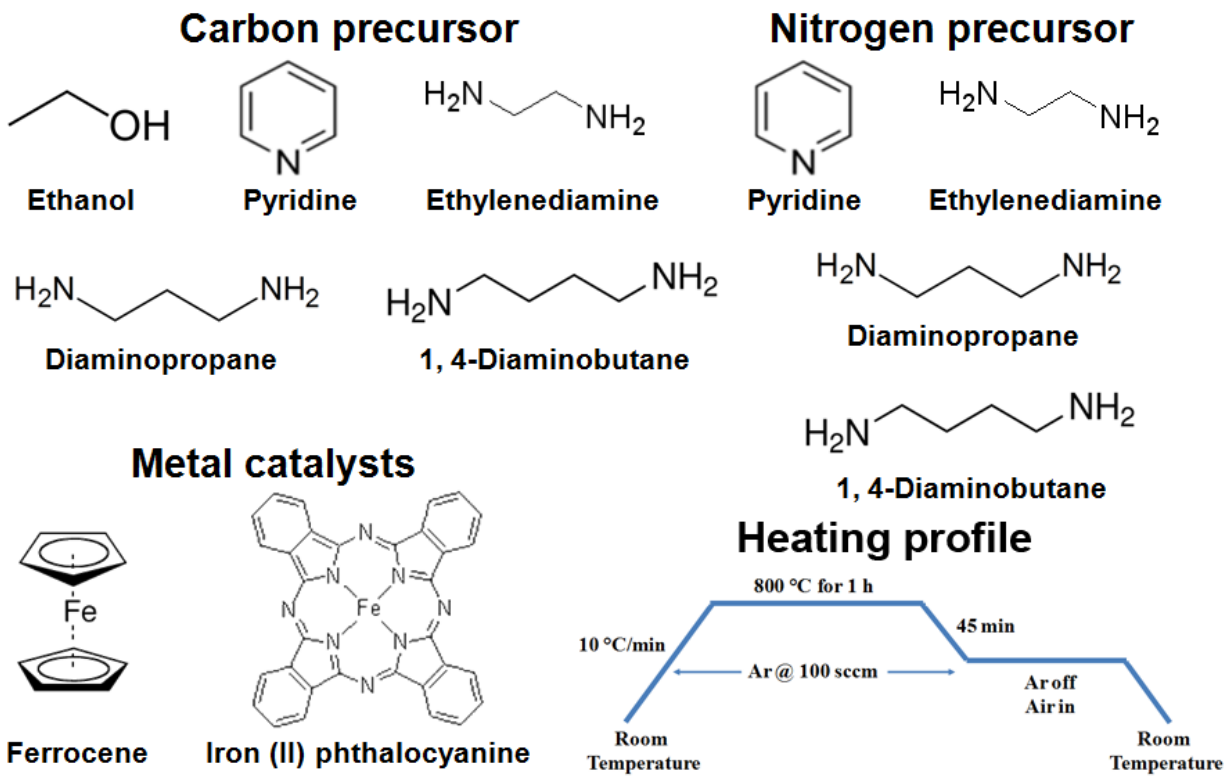

Figure 15 Chemical structure of carbon/nitrogen precursors and metal catalysts.

For a typical synthesis of NCNT, ferrocene was used as a catalyst and pyridine was used as the carbon and nitrogen precursors. A piece of small quartz tubes (O.D 18 mm, length 100 mm) was used as the substrates for NCNT growth. Ferrocene was dissolved in pyridine solution at 2.5 wt.% concentration. The mixture was stirred until complete dissolution and drawn into a 10 mL plastic syringe. The syringe is fitted onto a syringe pump and positioned in a configuration such that about 5 cm of the stainless steel needle that extended out from syringe is in the heating zone. A small quartz tube was used as the substrate for NCNT growth and it was loaded into the center of an alumina tube (1" outer diameter) surrounded by a single zone furnace system. For the entire duration of the synthesis, argon gas flowing at 100 sccm purged the system. The temperature of the furnace was heated from room temperature to 800 °C at a rate of 10 °C/min. The synthesis

temperature of the NCNT was chose to be 800 °C as it is above the sublimation point of the synthesis catalyst and the carbon and nitrogen precursors. Once the furnace temperature reaches 800 °C, the syringe pump was started which injects the precursor solution at a rate of 0.05 mL/min. After the synthesis is completed, the furnace is allowed to cool down to 450 °C. At this temperature, the exhaust end of the CVD system is open to air and the furnace temperature was maintained at 450 °C for 1 h. The reason behind the treatment in air was to remove the amorphous carbon to improve the purity of the product. The NCNT were obtained from the soot deposited on the surface of the quartz tube after growth. In a typical synthesis where a total 5 mL of precursor solution was injected, the approximate yield of NCNT is 100-150 mg. The obtained NCNT were subjected to acid treatment by boiling in 0.5 M sulfuric acid for 5 h and were dried in an oven overnight.

2.2 Scanning electron microscopy

Scanning electron microscopy (SEM) was used to investigate the topology of the NCNT. This characterization technique is especially useful for in collecting morphological information due to the fast turnaround time and simple sample preparation. SEM was used extensively to study the microstructure of the NCNT catalyst and with the addition of an X-ray detector and analysis software, simple compositional analysis of NCNT was also performed using this technique.

The operation principle of SEM is based on the interaction of electron with the sample. Figure 16 show the schematic of a typical SEM. The primary electron comes from emission source (i.e., a sharp tungsten tip) whereby the large potential difference between the emitter and the biased cathode results in the formation of a beam of electron with kinetic energy ranging from 0.2 to 40

kV. The highly energetic electrons travelling through the microscopy column is focused by several sets of magnetic coil to achieve a spot size of 0.4 nm to 5 nm. [127]

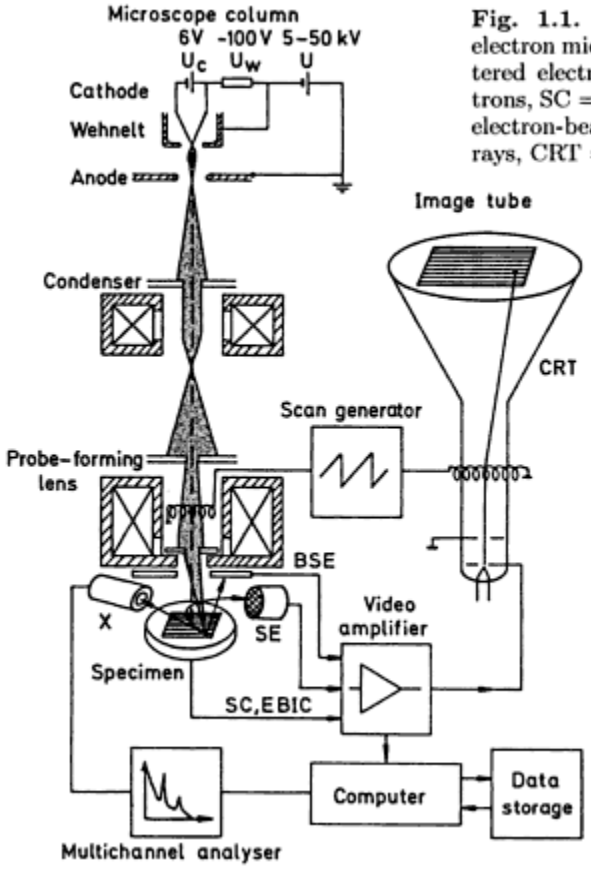

Fig. 1.1. Principle of the scanning electron microscopoe (BSE = backscattered electrons, SE = secondary electrons, SC = specimen current, EBIC = electron-beam-induced current, X = x-rays, CRT = cathode-ray tube)

Figure 16 Schematic drawing of SEM. Reprinted with permission from [127], Copyright 1998, Springer.

As the electron beam impinges on the sample, several types of radiation can be emitted. The first type of signal is called secondary electron, it is generated from the ionization effect of the initial electron beam. This type of electron is generated very close to the surface of the materials. As a result, secondary electrons carry rich information regarding surface topology. Backscattered electron can also be generated which is caused by the direct inelastic scatting of the incident

electron by the atomic nuclei of the sample. As a result, the backscattered electrons carry rich information regarding the atomic number (Z number) of the sample. The auger electrons can also be generated in SEM and it can be used to identify the elements and the chemical states present in the sample. X-ray is another radiation resulting from the interaction between the sample and the primary electron beam. Using the characteristic X-rays, elemental composition can be obtained from the energy dispersive X-ray spectroscopy (EDX). [127]

The secondary electrons and backscattered electrons are used to construct SEM images whereby the beam of electron is scanned over the sample in a raster fashion (line-by-line) and the emitted electron signals are collected and their relative strength are recorded. The final image is produced based on the different in the strength of electron signal. The resolution of the SEM images depends on the spot size of the electron beam. Typically, a field emission SEM can produce image with resolution of 10 nm. The major limitation of the SEM is that conductive samples must be used to avoid sample charging during imaging.

2.3 Transmission electron microscopy

Transmission electron microscopy (TEM) was used to investigate the structure of the NCNT catalyst with greater details. This characterization technique is especially useful for in collecting lattice and surface structural information due to the high resolution capabilities. TEM was used extensively to study the graphitic structure of the NCNT catalyst and with the addition of an X-ray detector and analysis software, compositional analysis of small areas (micrometer-scale) of NCNT sample was also performed using this technique.

The operation principle of TEM is based on the interaction of electron with the sample. Figure 17 show the schematic of a typical TEM. The primary electron comes from a emission source (i.e., lanthanum hexaboride, or series of sharp tungsten wires) whereby the large potential difference between the emitter and the biased cathode results in the formation of a beam of electron with kinetic energy ranging from 100 to 400 kV. The highly energetic electrons travelling through the microscopy column is focused by several sets of magnetic coil to achieve a spot size of tens of angstrom. [128]

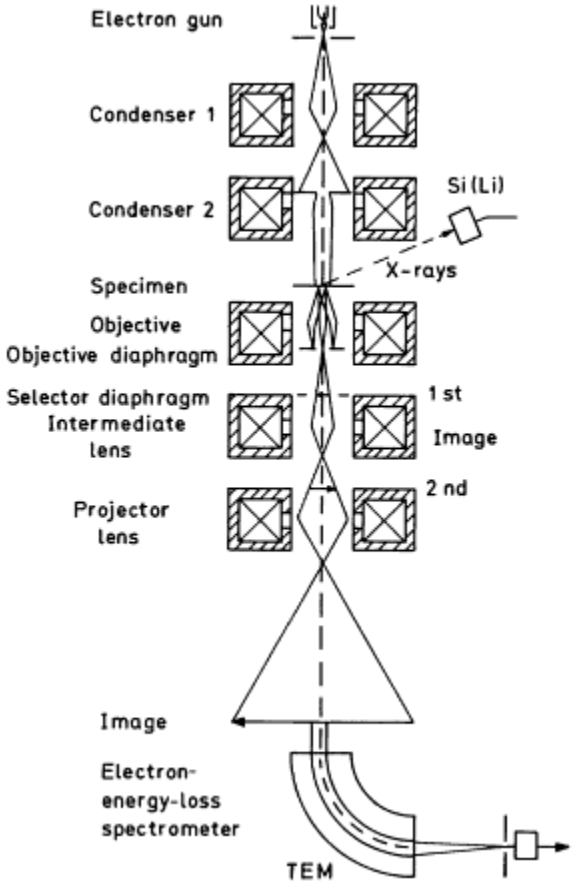

Fig. 1.1. Schematic ray path for a transmission electron microscope (TEM) equipped for additional x-ray and electron energy-loss spectroscopy.

Figure 17 Schematic drawing of TEM. Reprinted with permission from [128], Copyright 2008, Springer.

Unlike the SEM, the electron beam penetrates the sample in TEM. The sample for TEM is usually very thin, and is prepared onto a copper grid. The TEM samples are partly transparent to electron and partly scatters electron. When the electron beam emerges from the sample the difference in the energy of the beam provides the contrast required for imaging purposes. Highly energetic electrons from TEM can be used to probe the crystal structure of materials due to the interaction of electron wave with the material's valence electron and the positively charge nucleus. The selected area electron diffraction (SAED) study carried out by TEM has advantage over the X-ray diffraction technique in that it has shorter wavelength thus able to review more reciprocal lattice point from the Ewald Sphere. Furthermore, electron energy loss spectroscopy (EELS) can also be performed by the TEM when fitted with the correct detectors. EELS detects the energy loss of a beam of electrons with narrow kinetic energy distribution and provides information regarding the material composition, valence, chemical bonding and electronic band structure. Additionally, X-ray is a common radiation from the TEM emission. As a result, energy dispersive X-ray spectroscopy can be performed during TEM imaging which complements to the EELS study. [128]

Perhaps the most commonly used feature of TEM is the high resolution imaging where the resolution can reach 0.5 nm. Hgh resolution TEM (HRTEM) allows the imaging of crystallographic information of the sample. Imaging in HRTEM mode is not based on electron amplitude contrast, rather it operates on the interference of the existing wave of the incident electron beams. Currently, the factor affecting the resolution of TEM is the spherical aberration. The limitation of TEM is the relatively more time consuming sample preparation and longer turnaround time.

2.4 X-ray diffraction

X-ray diffraction (XRD) is a common techniques used to identify the crystal structure of the materials. In this study, XRD was used to study the spacing between the graphitic planes of the CNT and NCNT as well as to detect the formation of residual iron compounds after the NCNT synthesis.

X-ray diffraction operates based in the interaction of the X-ray with the electron density of sample atoms. The wavelength of X-ray used is very small, typically in the range of 0.01-50 angstrom which allows the X-rays to interact with atoms to obtain information about their long range orders. In a typical XRD setup (Figure 18), the sample is mounted on a goniometer which rotates as the monochromic X-rays impinge on the surface of the sample. As the angle between the X-ray and the sample changes, the diffraction event will occur only at certain angles known as the Bragg angle, where the distance traveled by the reflected X-rays from successive planes differs by a complete number n of wavelengths. Under such condition, constructive interferences can lead to the formation of diffraction patterns called reflections. When the diffraction pattern intensity is plotted with respect to the Bragg angle, the XRD pattern is formed which is specific to different materials.[129]

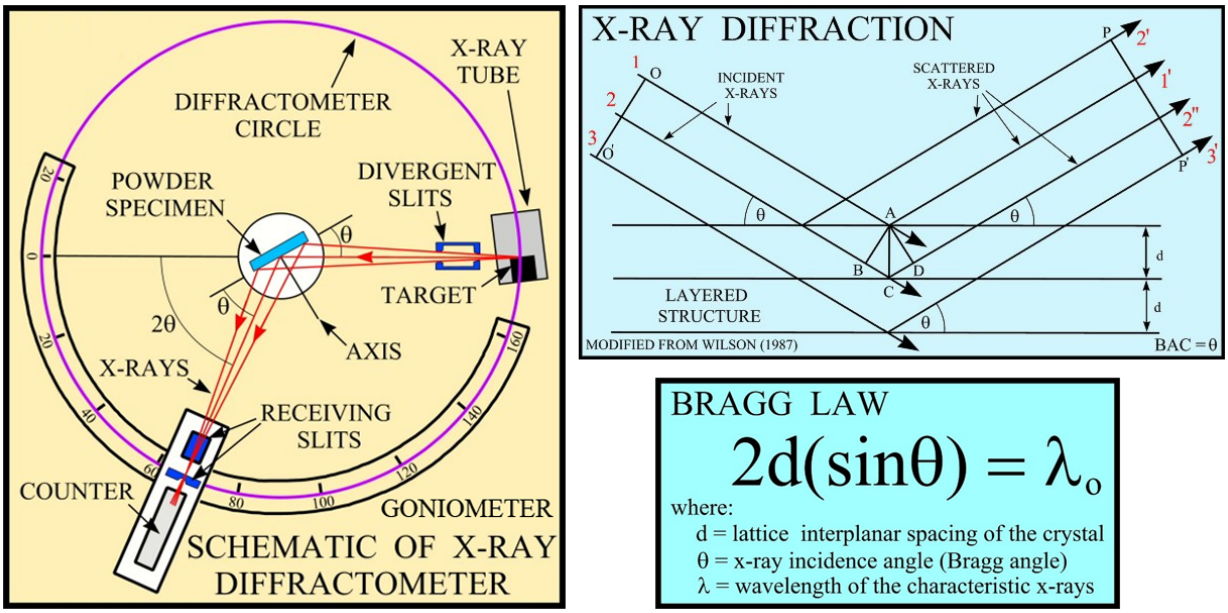

Figure 18 Experimental setup of XRD, Bragg diffraction and Bragg law. Reprinted from [129], Copyright 2010, Spectrum 2000 Mindware.

X-ray with specific energy can be produced from a monochromatic source. In this study, the X-ray used is generated by the Copper K-α X-ray radiation with a wavelength of 1.54 Angstrom. Using this information, the interplanar spacing of the graphitic layers in NCNT and CNT can be calculated. Given first order diffraction maximum and two theta value of 26 ° (or 0.454 radian), the interplanar distance is

$$2 * d * \sin(2\theta) = \lambda \qquad (11)$$

$$d = \frac{\lambda}{2 * \sin(2\theta)} = 1.54 * \frac{10^{-10}}{2 * \sin(\frac{0.454}{2})} = 0.342\ nm$$

This interplanar distance corresponds to the distance between the graphene sheet in the (002) crystallographic plane of the graphite materials. From theoretical calculation a value of 0.344 nm is expected which matches very closely to the value from XRD[130].

2.5 X-ray photoelectron spectroscopy

X-ray photoelectron spectroscopy (XPS) is a surface characterization tool used to study the elemental composition, surface bonding configuration, valence and electronic state of a sample. In this study, the XPS was used to study the elemental composition of NCNT. Among the different elements in the NCNT, nitrogen signal is of special interest. As a result, high resolution XPS (HR-XPS) spectrum focusing on collecting fine details of the N 1s spectrum was employed to establish correlation between the surface nitrogen groups and ORR activity. Deconvolution of the HR-XPS allows the identification of different chemical state of N atom on the surface of NCNT.

The operating principle of XPS is based on the interaction of incident X-ray photon and the sample electrons in ultrahigh vacuum conditions. In XPS, unlike the XRD or EDX, the emitted radiation is only from the 1-10 nm of the sample surface making this technique very surface sensitive. As the X-ray interacts with the samples, the energy transfer from X-ray photons to the electron occupying different energy state is showed in the equation below.[131, 132]

$$E_{photon} = E_{binding} + E_{kinetic} + \varphi \qquad (12)$$

From the equation, E_{photon} represent the energy of incident X-ray; $E_{binding}$ represents the binding energy of the electron at different energy state, for example 1s, 2s and 2p; $E_{kinetic}$ represent the kinetic energy of the excited electron and φ represent the work function of the spectrometer. By counting the number of electron at different binding energy, an energy spectrum specific to different elements can be precisely produced. HR-XPS can be achieved using additional monochromator in the XPS setup to achieve X-ray source of reduced energy width dispersion and improve chemical state selectivity by narrowing spectral peaks. Additionally, lower spectral

background and the elimination of unwanted x-rays from satellites and anode impurities can also be accomplished.[131-133]

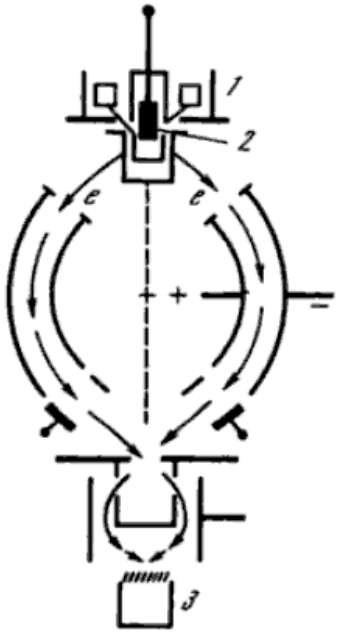

Figure 1.3. Schematic illustration of the VIEE-15 Varian spectrometer.
1 = X-ray tube; 2 = specimen; 3 = photoelectron multiplier.

Figure 19 XPS setup showing the X-rays irradiation and photo-emitted electrons detection. Reprinted with permission from [133], Copyright 1988, VSP BV Publishers.

A typical XPS can detect element with atomic number of 3 or above making it more sensitive compared to other elemental analysis methods such as EDX which cannot distinguish smaller elements with similar atomic number, for example carbon and nitrogen. The detection limit for the XPS is usually at parts per thousand range. However, high resolution can be achieved under extended signal collection time and higher surface concentration of species of interest.

2.6 Raman spectroscopy

Raman spectroscopy is used to study the vibrational and rotational modes of the sample. Raman spectroscopy was used in the study to provide qualitative measure of the degree of defects introduced to the otherwise pristine graphitic network as a result of nitrogen incorporation. Two bands are of particular interest from the Raman spectrum of NCNT. A lower wavenumber band at approximately 1350 cm^{-1} corresponds to the presence of disorder in the NCNT which can be related to defects or the reduced symmetry at the graphite plane edge[130, 134, 135]. The other band at approximately 1550-1600 cm^{-1} relating to the inherent E_{2g} optical mode of and is observed in all sp2 bonds in graphite network[134-136]. The intensity ratio of D- to G-band provides qualitative information regarding the defects presence in the NCNT samples. In addition, CNT shows characteristic radial breathing modes under Raman scattering condition which provides an estimate of the average diameter of the CNT. However, in this study the radial breathing mode portion of the Raman shift was not surveyed and diameter estimation was rely solely on the SEM and TEM which have shown to be sufficient.

The operating principle of Raman spectroscopy is based on the inelastic (Raman) scattering of monochromatic light (from laser, in the near infrared to near ultraviolet range) by the sample. The Raman effect occurs when the energy of the incident light after interacting with the vibratoinal or phonon modes of the sample is shifted up or down by the sample (Figure 20). The Rayleigh scattering mode in a Raman spectrometer is filtered out to prevent skewing and improve the resolution of the Raman active bands. The end output of the Raman spectroscopy is a spectrum plotting the Raman scattering intensity (arbitrary unit) to the wavenumber (unit of cm^{-1}). The position of the Raman band is a result of the shift in light energy which can be defined by the below equation.[137]

$$\Delta w = \left(\frac{1}{\lambda_0} - \frac{1}{\lambda}\right) \qquad (13)$$

The Raman shift is represented by Δw, the incident light wavelength is represented by λ_o and the scattered radiation wavelength is represented by λ. From the spectrum, the incident light wavelength has a wavenumber of zero and the scattered radiation can be shifted towards positive or negative direction. The main limitations of Raman spectroscopy is the weak Raman scattering signal and the strong lasers used prevents its application towards sensitive materials.[137]

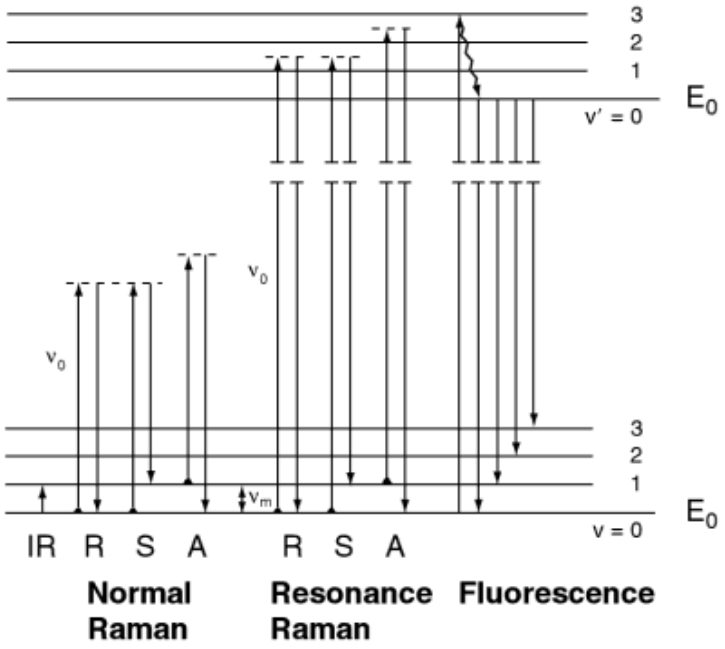

Figure 1-8 Comparison of energy levels for the normal Raman, resonance Raman, and fluorescence spectra.

Figure 20 Scattering events encounter in Raman spectroscopy. Reprinted with permission from [134], Copyright 2003, Academic Press.

2.7 Thermogravimetric analysis

Thermogravimetric analysis is used to study the weight change of sample as a function of temperature. In this study, TGA was used to determine the thermal stability of the NCNT as well as to estimate the metal and amorphous carbon content. By deconvolution of the TGA profile, the decomposition temperature of NCNT can be determined. The TGA experiment is performed by heating the sample of known mass in a platinum pan either in pure N_2 or N_2/air (50/50 mixture) environment. The temperature setpoints, ramp rate and dwell time can be controlled by the software. In a typical experiment, the NCNT was heated up to 900 °C in N_2/air environment at a ramp rate of 5 °C/min.

2.8 Half-cell electrochemical evaluation

Half-cell electrochemical test is a very useful technique for the fast evaluation and screening of electrocatalysts. For the series study reported in this thesis, rotating ring disk electrode (RRDE) voltammetry was employed to carry out different electrochemical protocols. The basic setup of the RRDE voltammetry is showed in the Figure 21. A three neck flask was used as the half-cell reactor and it was filled with 0.1 M potassium hydroxide (KOH) which is the electrolyte used for all the half-cell evaluations. The working electrode (RRDE electrode) consists of a glassy carbon electrode (5 mm OD) and a platinum ring electrode (99.99 % Pt, 6.5 mm ID, 7.5 mm OD) separated by a thin layer of Teflone. This electrode is fixed onto a rotating shaft and controlled by a rotator. A double junction Ag/AgCl and a platinum wire were used at the reference and counter electrodes, respectively. The three electrodes are connected to a biopotentiostat which biases the RRDE system and reads the current from the working electrode. Prior to RRDE voltammetry, 2 mg of bifunctional catalyst was suspended in 1 mL of 0.5 wt% Nafion solution. The resulting solution is referred to as the “catalyst ink” and was sonicated until excellent

dispersion was achieved. For each RRDE experiment, 10 µL of catalyst ink was deposited onto the glassy carbon electrode and allowed to dry (loading of 0.2 $mgcm^{-2}$). After the ink was dried, the electrode was visually inspected to ensure uniform film formation.

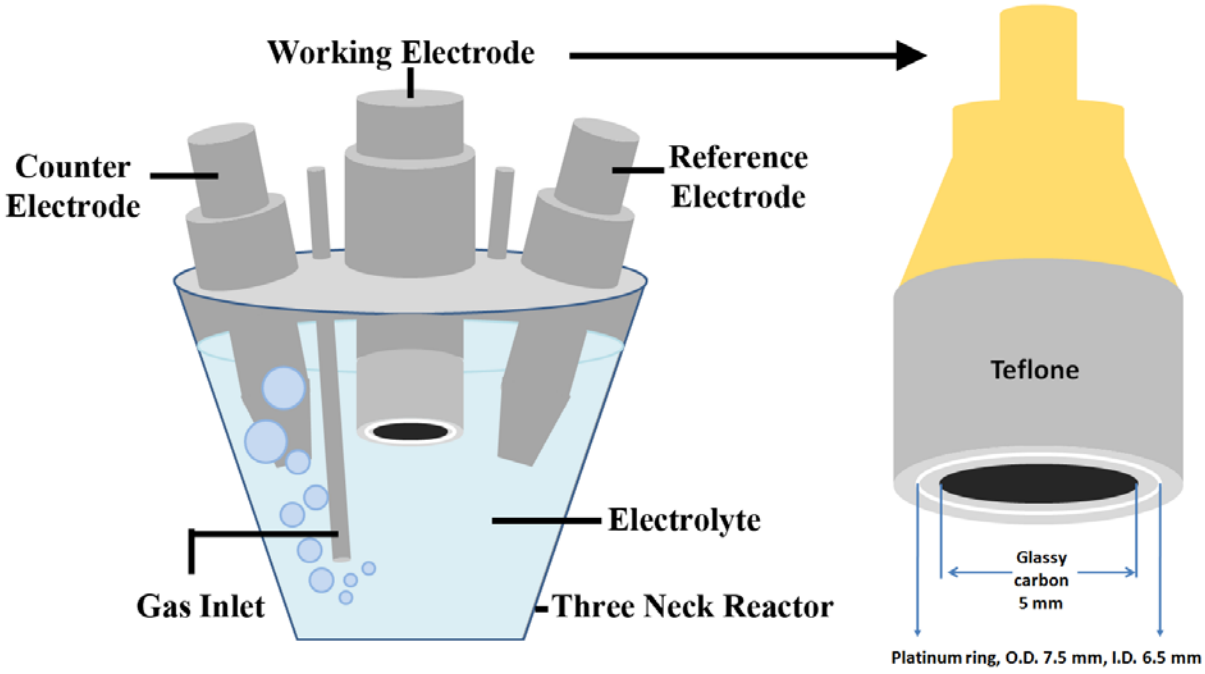

Figure 21 RRDE voltammetry setup and RRDE electrode schematic.

The advantage of using a RRDE system is to create a laminar flow of electrolyte which delivers the dissolve reactants to the surface of the RRDE electrode. The rotating speed of the RRDE can be correlated to the rate of convention of the reactants.

Several electrochemical protocols can be carried out using the RRDE setup. The first of which is linear scan voltammetry (LSV). In LSV the potential of the working electrode, versus the reference is swept from one high to lower potentials and the current from the working electrode

is recorded. In a typical experiment, the potential range of the LSV experiments is from 0.2 to -1 V vs. Ag/AgCl reference electrode and the potential sweeping rate is 10 mVs^{-1}. Under N_2 saturated electrolyte, LSV experiment measures the capacitive current of the active materials and it is considered to be the background current which is required to be corrected. In oxygen saturated electrolyte, the LSV experiment is carried out with different working electrode rotation speeds (100 rpm to 1600 rpm). The saturation condition for the electrolyte is achieved by bubbling the solution with desirable gas for 30 min. The resultant current from the LSV reflects the electrochemical reaction taking place on the working electrode. Typical polarization curves of Pt/C are showed in Figure 22. Three regions can be defined on the polarization curve. Region A corresponds to the initial stage of electrochemical reaction whereby the kinetics of the reaction limits the rate of reaction. For an excellent catalyst, the kinetically controlled region would be minimized. Region B corresponds to the mixed control region where mass transfer of oxygen and the kinetic limitation both influence the overall rate of reaction for an active catalyst, the slope of the pseudo-linear region would be very steep. Region C corresponds to the mass transfer limited region where the working electrode is biased to a very high potential and the reaction kinetics is faster such that the rate of oxygen consumption is greater than the rate of transfer. As the rotation speed of the working electrode increases, the rate of oxygen transfer will increase which in turn increase the mass transfer limited current.

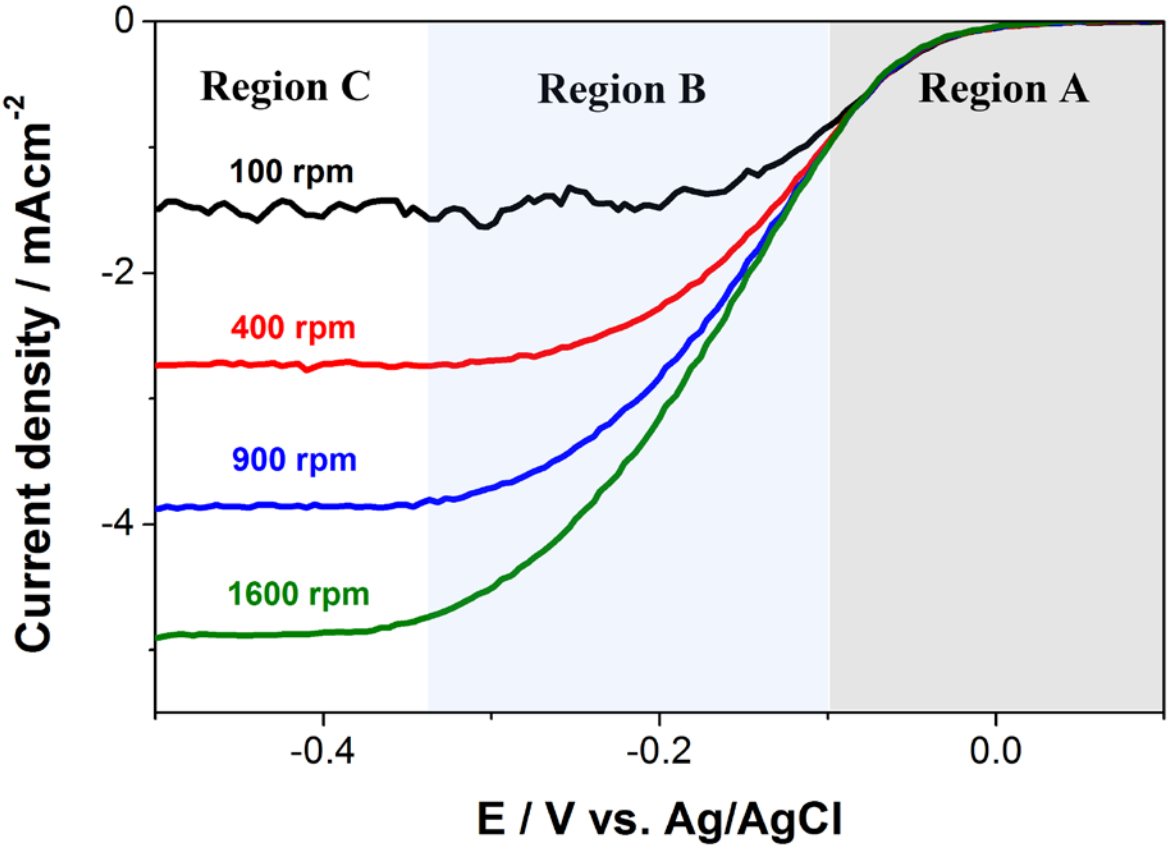

Figure 22 ORR polarization of NCNT under four different rotation speeds.

The Koutecky-Levich (K-L) equation can be used to further examine the reaction kinetics. The K-L equation relates the observed current density (j) with the kinetic current (j_K) and limiting current density (j_L) through the Levich slope (B) and electrode rotation speed (ω). From this relationship, the number of electrons transferred (n) can be calculated using the following equation,

$$\frac{1}{j} = \frac{1}{j_K} + \frac{1}{j_L} \qquad (14)$$

$$j_L = B\omega^{\frac{1}{2}} \qquad (15)$$

The Levich slope can be further defined as,

$$B = 0.2nFD_o^{\frac{2}{3}}C_o\upsilon^{-\frac{1}{6}} \qquad (16)$$

In the above equation, F is the Faraday constant, D_o is the diffusion coefficient of O_2 (1.9×10^{-5} cm^2s^{-1}), C_o is the concentration of O_2 in the electrolyte (1.1×10^{-6} $molcm^{-3}$) and υ is the kinematic viscosity of the solution (0.01 cm^2s^{-1}). The K-L plots can be constructed by plotting the reciprocal value of j versus ω at different working electrode potentials. The Y-intercept of the K-L plot will represent the j_K and the slope of the K-L plot can be used to determine the number of electrons transferred. For an active ORR catalyst, the number of electron transfer will be four or very close to four indicating the catalysis of ORR by the more efficient four-electron pathway.

Cyclic voltammetry (CV) can be used to identify the capacitance and surface electrochemical species of the catalyst sample. For the CV experiment, the potential of the working electrode is swept repeatedly between two values. The potential sweep rate is 10 mVs^{-1} and the experiment is carried out in N_2 saturated electrolyte. The capacitance can be calculated from the CV voltammogram by the integrating the area enclosed by the CV curve.

RRDE electrode is design to facilitate the detection of by-products by using the platinum ring. In the case of ORR, one of the possible by-products detectable to platinum is the HO_2^- (or H_2O_2 if the reaction takes place in acid media). In a typical LSV experiment, the platinum ring is commonly biased to 0.5 V vs. Ag/AgCl when the electrolyte is alkaline. Under such condition, the ring current can be used to calculate the number of electrons transferred (equation 17).

$$n = \frac{4 * I_D}{I_D + \frac{I_R}{N}} \qquad (17)$$

In this equation, I_D represents the current obtained from the glassy carbon disk and I_R represents the current obtained from the platinum ring. N represents the collection efficiency of the platinum ring. Similarly, the selectivity towards OH^- formation (equation 18) can also be calculated.

$$\% \, selectivity = \left(\frac{I_D + \frac{I_R}{N}}{I_D + \frac{I_R}{N}} \right) * 100 \qquad (18)$$

2.9 Zinc-air battery evaluation

Zinc-air battery tests of the NCNT catalyst will complement the electrochemical kinetics information obtained from the half-cell evaluations. Zinc-air battery testing of the catalyst was performed using a multichannel potentiostat (Princeton Applied Research, VersaSTAT MC) and a home-made zinc-air battery. The prototype zinc-air battery and the components of the battery is shown in Figure 23. A polished zinc plate and a piece of catalyst-coated gas diffusion layer (Ion Power Inc., SGL Carbon 10 BB, 2.5 cm by 2.5 cm) were used at the anode and cathode, respectively. Microporous membrane (25 μm polypropylene membrane, Celgard 5550) was used as a separator and stainless steel mesh was used as current collectors. The electrolyte used in the zinc-air battery was 6 M KOH.

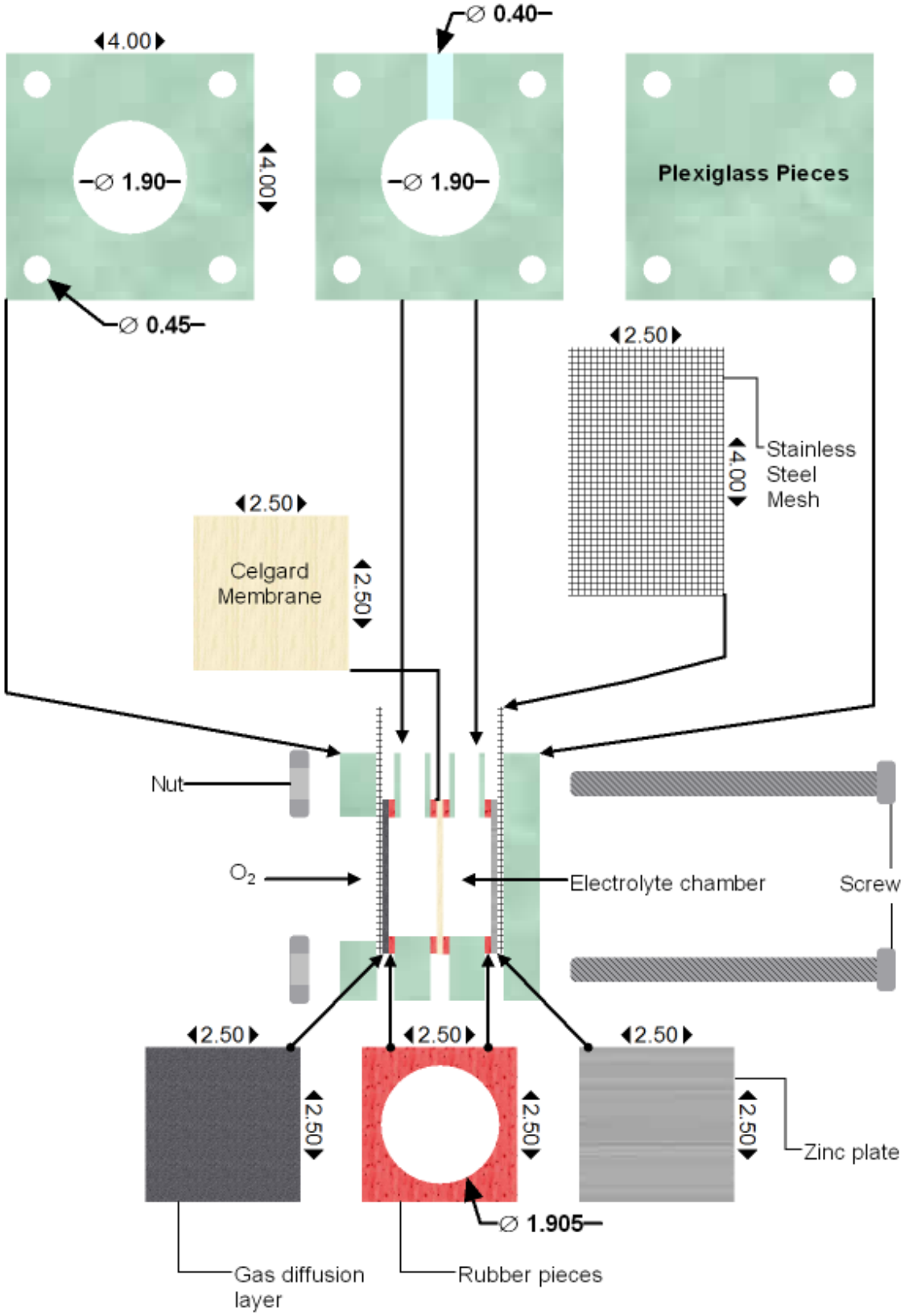

Figure 23 Design of prototype zinc-air battery.

Based on the battery design, the actual area of the gas diffusion layer being exposed to the electrolyte is 2.84 cm^2. All the catalysts studied in this work were coated onto the gas diffusion layer using an airbrush to achieve a loading of ca. 0.72 $mgcm^{-2}$. Briefly, 9.4 mg of catalyst was dispersed in 1 mL of isopropanol and sonicated for 30 minutes. Following this, 67 μL of 5 wt. % Nafion solution was added and the mixture was sonicated for 30 minutes to form the catalyst ink. The catalyst ink was sprayed onto the gas diffusion layer with a conventional airbrush. After spraying, the gas diffusion electrode is dried at 80 °C for 1 h. The catalyst loading is determined by the difference in the weight of the gas diffusion layer before and after spraying.

A galvanodynamic method was used to discharge and charge the battery to 200 mA. The potential difference between the cathode and the anode was determined to be the open circuit voltage. Electrochemical impedance spectroscopy was performed from 100 kHz to 0.1 Hz with AC amplitude of 20 mV.

3 Effects of precursor structure on the ORR activity of NCNT

Chen, Z., Higgins, D., Tao, H., Hsu, R.S., and Chen, Z. Highly active nitrogen doped carbon nanotubes for oxygen reduction reaction in fuel cell applications. Journal of Physical Chemistry C. (2009) 113: 21008-21013

3.1 Purpose of the study

Tremendous efforts have been made towards the development of non-noble metal catalysts to replace the expensive platinum catalysts for ORR—a critical reaction for not only metal-air battery but also fuel cells. Nitrogen doping of CNTs have shown great promise as contender to the platinum based catalyst for ORR catalysis based on computational and experimental studies. It has been demonstrated that nitrogen on the surface of the carbon was an essential requirement to obtain non-noble metallic-based catalytic sites; however, their ORR mechanism is poorly understood. It has been proposed that the catalytic activity observed on NCNT may be attributed to two different active sites. Specifically, one relates the origin of the ORR activity in NCNT with the transition metal-nitrogen groups (FeN_4), similar to those found in transition-metal macrocycles.[138, 139] The other attributes the source of the ORR activity in NCNT to surface nitrogen in the form of pyridinic and pyrrolic/pyridone-type nitrogen groups.[140, 141] Consequently the nature of nitrogen groups and overall content in NCNT is expected to be a governing factor with respect to the ORR activity. Thus, using different nitrogen precursors for NCNT synthesis could lead to varying nitrogen content and chemical states which are hypothesized to affect the ORR activity of the resultant NCNT.

This paper presents the synthesis of NCNT using ethylenediamine (EDA) and pyridine (Py) as different nitrogen precursors, and ferrocene (Fc) as a catalyst through a single step CVD process. The NCNT grown from the Fc/EDA mixture (EDA-NCNT) will be used for the first time as a non-noble ORR catalyst. The difference in the ORR activity between EDA-NCNT and NCNT grown from Fc/Py mixture (Py-NCNT) will be discussed. Furthermore, the effect of different nitrogen precursors on the nitrogen content and the ORR electrocatalytic activity of NCNT will be investigated by comparing EDA-NCNT and Py-NCNT.

3.2 Experimental methods

NCNT synthesis methodology is outlined in section 2.1. Briefly ferrocene (98%, Aldrich) was used as a catalyst and pyridine (99% Caledon Laboratory Chemicals) or ethylenediamine (98% EMD Chemicals) was used as a carbon and nitrogen precursor. After synthesis, SEM (LEO FESEM 1530, 20 eV) was used to investigate the overall morphology of NCNT. TEM (PHILIPS CM300) was used to examine the graphitization of the NCNT walls and to observe defected sites. XPS (Thermal Scientific K-Alpha XPS spectrometer, 150 eV) was used to investigate the relative content of different elements and the intensity of different nitrogen groups in the NCNT. EDX was used to evaluate the elemental composition of the NCNT samples. Electrocatalytic activity was evaluated using RRDE voltammetry. The instruments used include a biopotentiostat and a rotation speed controller (Pine Research Instrumentation). The RRDE experiments were carried out according to the protocols outlined in section 2.8. The only variation used was the concentration of nafion solution during the preparation of the catalyst ink. In this particular study, 0.2 wt% Nafion solution was used for the catalyst ink preparation.

3.3 Results and discussions

The morphology of EDA-NCNT and Py-NCNT was investigated by SEM. Nanotube alignment was observed for both EDA-NCNT and Py-NCNT (Figure 24). Along the nanotube growth axis, a zigzag pattern was observed for EDA-NCNT (Figure 24a inset), whereas a relatively more straight geometry was observed for Py-NCNT (Figure 24b inset).

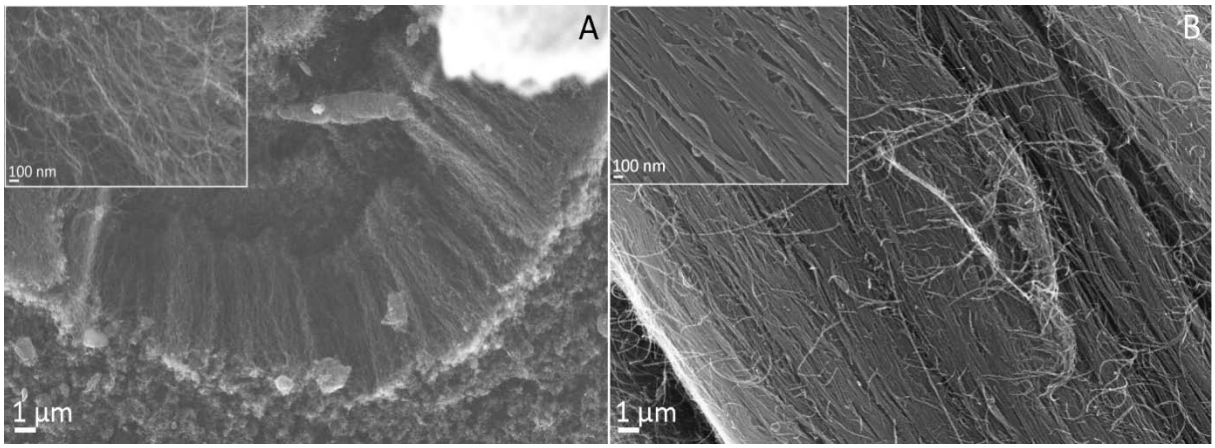

Figure 24 SEM image of a) EDA-NCNT and b) Py-NCNT.

EDX was performed simultaneously with SEM imaging. EDX analysis showed that the atomic composition from highest to lowest in the EDA-NCNT and Py-NCNT was carbon, oxygen, nitrogen and iron. These results and their respective compositions can be found in Table 4. This shows that nitrogen was successfully incorporated into both catalyst samples. A more detailed study on the nitrogen content and its bonding with the native carbon atoms by XPS will be presented later in this paper. The presence of oxygen was observed in both samples, which could be attributed to the fact that air was allowed to enter the furnace at 400 °C for the purpose of burning off amorphous carbon after the growth was completed.

Table 4 Summary of the elemental compositions of EDA-NCNT and Py-NCNT from EDX.

Composition	**EDA-NCNT (at. %)**	**Py-NCNT (at. %)**
Carbon	84.48	89.65
Nitrogen	5.58	3.41
Oxygen	8.33	5.18
Iron	1.61	1.77

The NCNT formed were observed using TEM which show bamboo-like structures for EDA-NCNT (Figure 25a) and Py-NCNT (Figure 25b), a common feature of NCNT published in many literature.[142-145] The formation of the bamboo-like structure is attributed to the more energetically favourable formation of a positive curvature surface during the substitution of nitrogen atoms into the graphitic structure.[126] More rounded compartments were observed for EDA-NCNT, whereas Py-NCNT demonstrated more rectangular compartments. Apart from the difference in compartments, the graphitic walls of the nitrogen rich EDA-NCNT are thinner compared to the relatively nitrogen deficient Py-NCNT which correlates to the increase in overall nitrogen content.[142, 143]

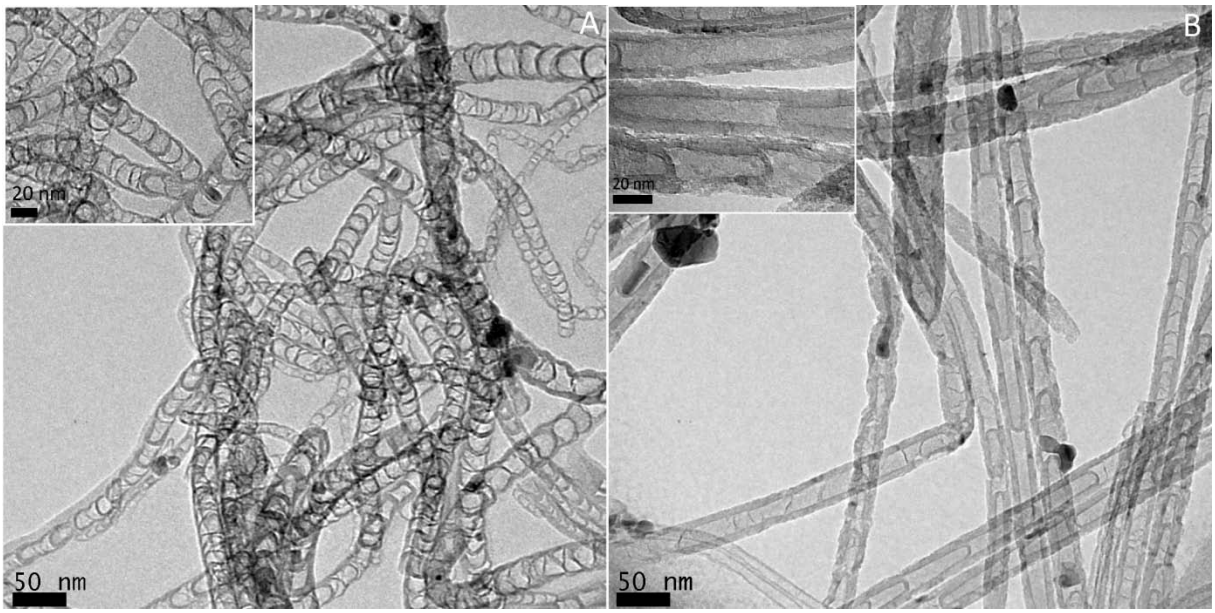

Figure 25 TEM image of a) EDA-NCNT and b) Py-NCNT. The scale bar in the inset is 20 nm.

RRDE voltammetry was used to evaluate the electrocatalytic activity of NCNT in the ORR (Figure 26). Compared to Py-NCNT, a three-fold increase in limiting current density was observed in EDA-NCNT. In addition, a 0.17 V improvement in HWP is observed for EDA-NCNT (onset potential of 0 V vs. Ag/AgCl) compared to that of Py-NCNT (onset potential of -0.2 V vs. Ag/AgCl), and the number of electrons transferred was improved by 12.6% at -0.3 V.

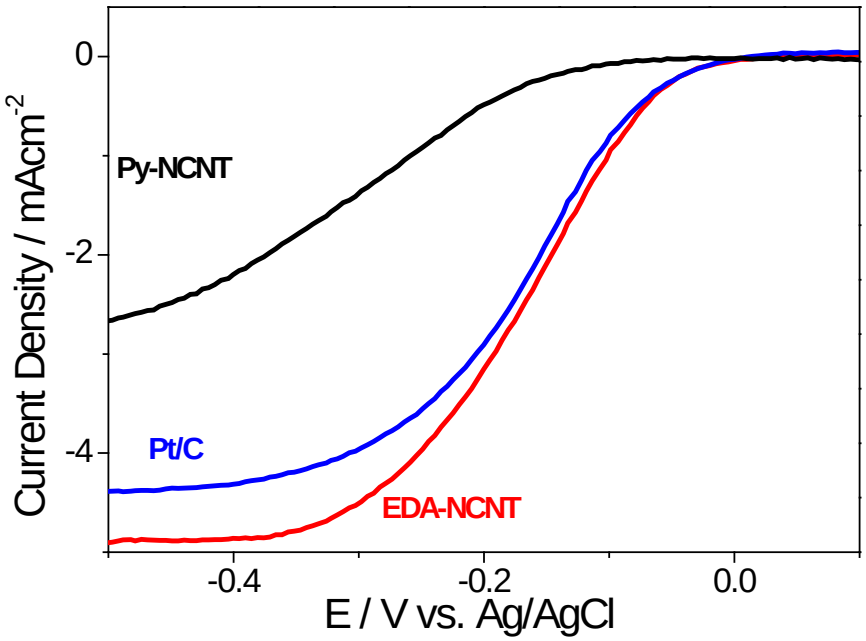

Figure 26 Polarization curve of EDA-NCNT, Py-NCNT and Pt/C at 1600 rpm.

Similarly, with respect to H_2O selectivity EDA-NCNT showed a significant 21.6% improvement compared to Py-NCNT. With regard to EDA-NCNT and Pt/C, EDA-NCNT displayed slight improvement in HWP, number of electrons transferred and H_2O selectivity. However, a 12% increase in limiting current density was observed in EDA-NCNT compared to Pt/C. The half-wave potential (HWP), limiting current density, number of electrons transferred in reaction and H2O selectivity are summarized in Table 5. It is clear that the ORR activity of EDA-NCNT is similar to commercial Pt/C catalyst and superior to Py-NCNT with respect to every parameter investigated (Table 5).

Table 5 Summary of the important performance indicators of ORR catalysis. Starred (*) entries indicate values taken at -0.1 V and the double daggered entries (‡) indicates values taken at -0.3 V.

	Half Wave Potential (V)	**Limiting Current Density (mA cm^{-2})**	**Number of Electron Transferred (at 1600 rpm)**		**H_2O selectivity (%) (at 1600 rpm)**	
EDA-NCNT	-0.15 V	-4.91	3.63*	3.85‡	84.69*	92.62‡
Py-NCNT	-0.33 V	-1.57	---	3.42‡	---	71.02‡
Pt/C	-0.16 V	-4.39	3.55*	3.82‡	81.33*	91.82‡

The kinetic analysis of the ORR performance of EDA-NCNT, Py-NCNT and Pt/C can be carried out by the K-L equation. The K-L relationship is valid in the mixed diffusion and kinetic limited regime. From the K-L plots of EDA-NCNT and Pt/C, similar slopes are an indication of the first order reaction kinetics of the ORR (Figure 27).[146, 147]

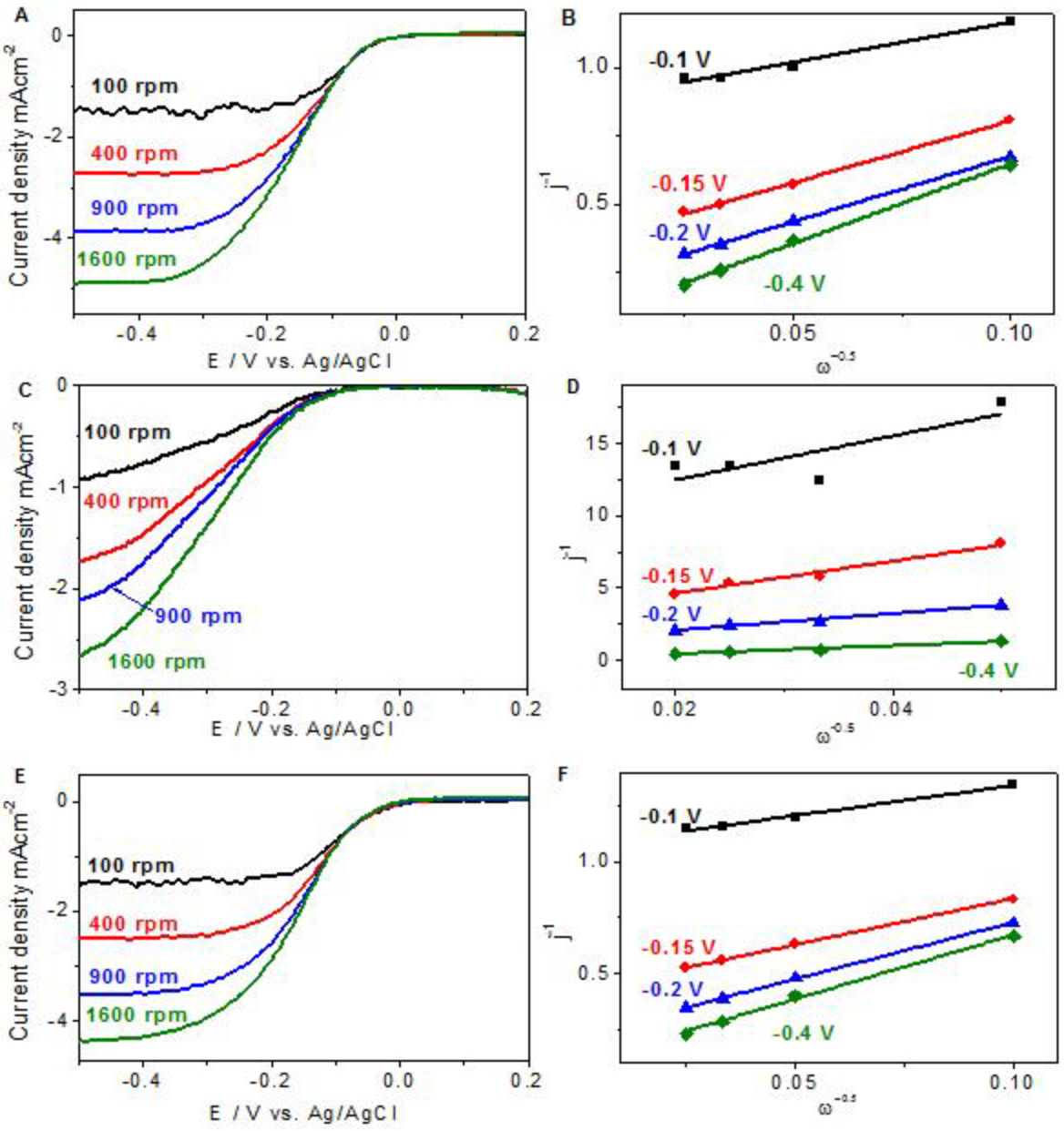

Figure 27 Koutecky-Levich plot of a) EDA-NCNT, c) Py-NCNT and e) Pt/C at different potential. Polarization curve of b) EDA-NCNT, d) Py-NCNT and f) Pt/C at different electrode rotation speed.

The slope of the K-L plots of Py-NCNT at different potentials varies greatly, indicating the kinetics of the ORR catalysis by Py-NCNT may differ from the first order kinetics observed by both Pt/C and EDA-NCNT. From equation (14), values of j_K at different potentials can be

obtained by taking the inverse of the Y-intercept in the respective K-L plots. The highest calculated kinetic current density was observed for EDA-NCNT showing a 46% increase compared to Pt/C and 123% increase compared to Py-NCNT (Table 6).

Table 6 Kinetic current of EDA-NCNT, Py-NCNT and Pt/C at different potentials.

	EDA-NCNT	**Pt/C**	**Py-NCNT**
E / V vs Ag/AgCl	**j_k / mAcm^{-2}**	**j_k / mAcm^{-2}**	**j_k / mAcm^{-2}**
-0.1	1.15	0.93	0.11
-0.15	2.85	2.37	0.42
-0.2	5.07	4.56	1.11
-0.4	15.06	10.31	6.76

Information regarding the mechanism of O_2 adsorption can be obtained through the Tafel slopes in the generated Tafel plots (Figure 28). The interval used to determine the Tafel slopes in low and high current density regions are from -1.2 to -0.7 and -0.4 to 0.1 respectively in the log scale. The use of fixed intervals for Tafel slope determination is necessary for a fair comparison between different samples. The Tafel slope in the low and high current density region of the Pt/C sample is -0.064 Vdec^{-1} and 0.120 Vdec^{-1} respectively (Figure 28d). The presence of two different slopes corresponds to the switch between Langmuir adsorption and Temkin adsorption of oxygen on the Pt/C catalyst. The Tafel plot of EDA-NCNT shows a similar profile with a Tafel slope of -0.066 Vdec-1 in the low current density region and -0.114 Vdec-1 in the high current density region (Figure 28b), indicating similar adsorption kinetics of EDA-NCNT

compared to Pt/C. The Tafel slope of Py-NCNT is -0.097 $Vdec^{-1}$ and -0.252 $Vdec^{-1}$ at low and high current densities respectively (Figure 28c). This large variation of Tafel slope of Py-NCNT indicates much different adsorption kinetics of Py-NCNT compared to EDA-NCNT and Pt/C.

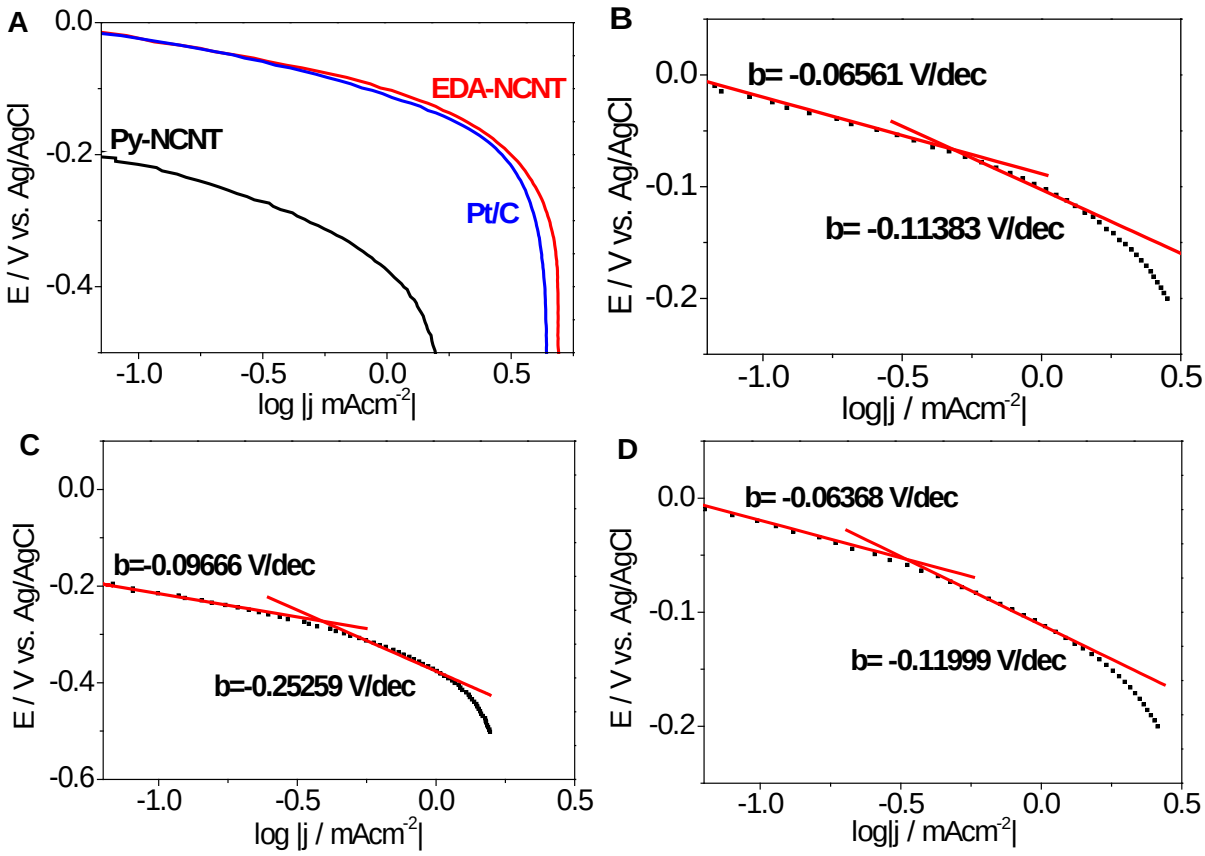

Figure 28 a) Tafel plots comparison. Tafel plot of b) EDA-NCNT, c) Py-NCNT and d) Pt/C

The elemental composition and different structural groups of nitrogen in EDA-NCNT and Py-NCNT was obtained using XPS (Figure 29).

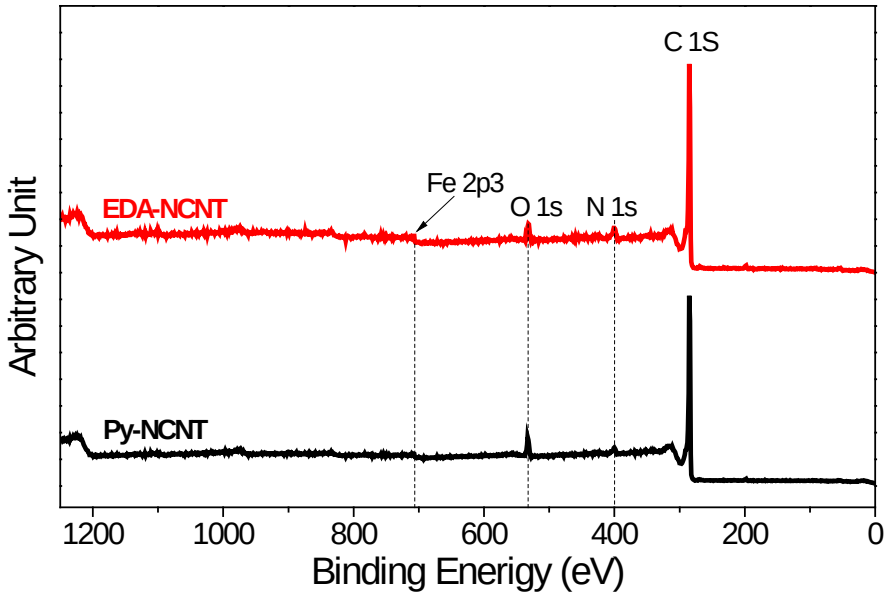

Figure 29 XPS spectrum of EDA-NCNT and Py-NCNT.

From XPS results, EDA-NCNT showed higher nitrogen content compared to Py-NCNT (Table 7). Higher nitrogen content in EDA-NCNT were expected as each EDA molecule contains two nitrogen atoms whereas only one nitrogen atom is present in each Py molecule. Consequently, higher nitrogen to carbon ratio in the growth environment was achieved during CNT synthesis when EDA was used. This result agrees with the literature which shows a positive correlation between NCNT nitrogen content and the number of nitrogen atoms in the precursor molecules.[148]

Table 7 XPS analysis of the elemental composition of EDA-NCNT and Py-NCNT.

	EDA-NCNT		**Py-NCNT**	
	Peak Position (eV)	**At. %**	**Peak Position (eV)**	**At. %**
Carbon	284.69	91.50	284.64	92.70

Nitrogen	400.84	4.74	399.88	2.35
Oxygen	531.65	3.38	532.57	4.75
Iron	707.28	0.38	708.01	0.20

From the analysis of the N 1s signal (Figure 30), peaks centered at 398.47 eV, 400.75 eV and 404.87 eV were observed for Py-NCNT. Similar peaks centered at 398.60 eV, 401.05 eV and 404.69 eV were observed for EDA-NCNT. The peaks at around 398.6 eV and 404.6 eV refer to pyridinic nitrogen and pyridinic N^{+}-O^{-} groups respectively. There is some ambiguity towards the peaks at 401.05 eV and 400.75 eV from EDA-NCNT and Py-NCNT respectively since they are close to the peak of the pyrrolic nitrogen group at 400.5 eV but also close to quaternary nitrogen at 401.3 eV. Hence, it is proposed that the peaks at 401.03 eV and 400.75 eV indicate the co-existence of quaternary and pyrrolic nitrogen groups. The peak from EDA-NCNT at 401.03 eV is much closer to the quaternary nitrogen peak position (401.3 eV) and the peak of Py-NCNT at 400.75 eV is much closer to the pyrrolic nitrogen peak position (400.5 eV). Therefore, it is concluded that EDA-NCNT contains more quaternary nitrogen whereas Py-NCNT contains more pyrrolic nitrogen. In addition, since the NCNT synthesis was carried out in ambient conditions, the reaction between oxygen and nitrogen during synthesis results in the formation of pyridinic N^{+}-O^{-}.

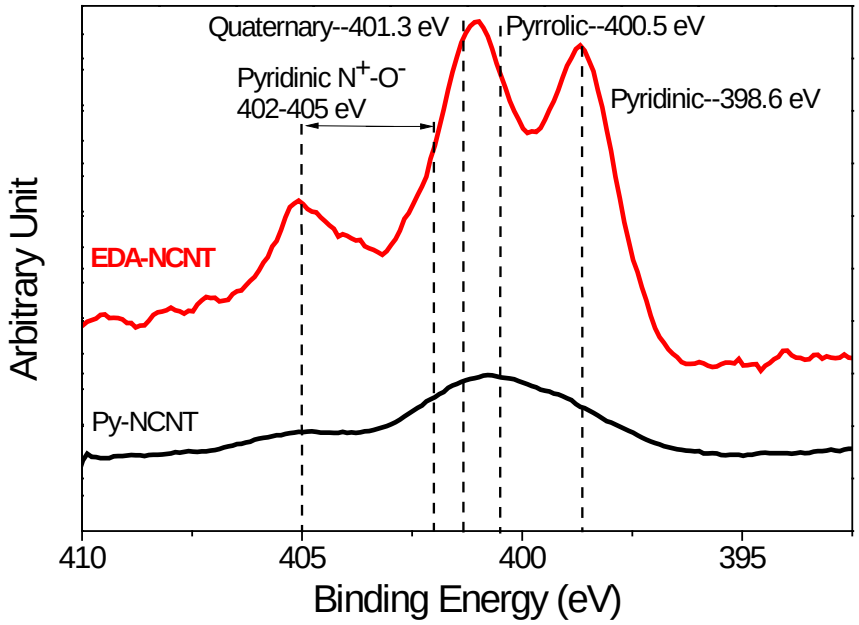

Figure 30 HR-XPS of N 1s signal of EDA-NCNT and Py-NCNT.

More pyridinic nitrogen groups were observed in EDA-NCNT than seen in Py-NCNT (Table 8), which agrees with the results of other studies where at higher overall nitrogen content, the formation of pyridinic nitrogen is preferred.[142, 149] On the contrary, for Py-NCNT containing less overall nitrogen, quaternary nitrogen was the dominant product, similar to results obtained by Terrones et al.[142, 143] In NCNT there is a tendency for substituted nitrogen atoms to form on the inner walls of MWNT.[126] Hence the amount of quaternary nitrogen on the outermost graphite wall could be lower than the total amount reported from XPS analysis which reduces the amount of quaternary nitrogen available for ORR. Since the nitrogen group on the outermost graphite wall is most important for ORR, it suggests that quaternary nitrogen does not have a big impact on the ORR. From XPS, EDA-NCNT contains a significantly higher pyridinic nitrogen content of 1.7 at.% compared to Py-NCNT at 0.3 at.%. Formation of pyridinic nitrogen groups is often observed on the edge of the graphite plane and the lone pair of electrons from pyridinic nitrogen

groups has been attributed be ORR acitive.[150] The higher exposure of the planar edges of graphite in EDA-NCNT due to the more rugged surface structure is expected to expose more pyridinic nitrogen which enhance the ORR activity. This explains the significant improvement in the ORR activity of EDA-NCNT over Py-NCNT.

Table 8 HR-XPS analysis of the N 1s signal of EDA-NCNT and Py-NCNT.

	EDA-NCNT		**Py-NCNT**	
	Peak Position (eV)	**%**	**Peak Position (eV)**	**%**
Quaternary / Pyrrolic	401.05	45.91	400.75	68.20
Pyridinic	398.60	35.09	398.47	14.83
Pyridinic N^+-O^-	404.69	19.00	404.87	16.96

Raman spectroscopy was also used to provide information on the degree of structural defect of NCNT (Figure 31). For EDA-NCNT the peak centered at 1311 cm^{-1} is the Raman active D-band and the other centered at 1564 cm^{-1} is the Raman active G-band. The D- and G-bands are also present in Py-NCNT centered at 1307 cm^{-1} and 1581 cm^{-1} respectively. The D-band is ascribed to the finite sized crystals of graphite, which become active due to a reduction in symmetry near or at the crystalline edges.[151] The G-band is due to the E_{2g} vibration mode and is observed in all sp2 bonds in a graphitic network.[151] The intensity ratio of the D- to G-band (I_D/I_G) gives qualitative information comparison for the degree of defects in NCNT. A higher ratio indicates more defects present in the nanotubes. From Raman spectra, the I_D/I_G ratio of Py-NCNT and EDA-NCNT is 1.87 and 2.07 respectively, indicating a higher degree of defects in EDA-NCNT

which could be caused by the higher nitrogen content. This conclusion is consistent with the TEM images and XPS data. With respect to Py-NCNT, the Raman spectrum of EDA-NCNT showed a slight downshift of the G-band, possibly caused by the change in electronic structure of NCNT due to the higher nitrogen content.[152]

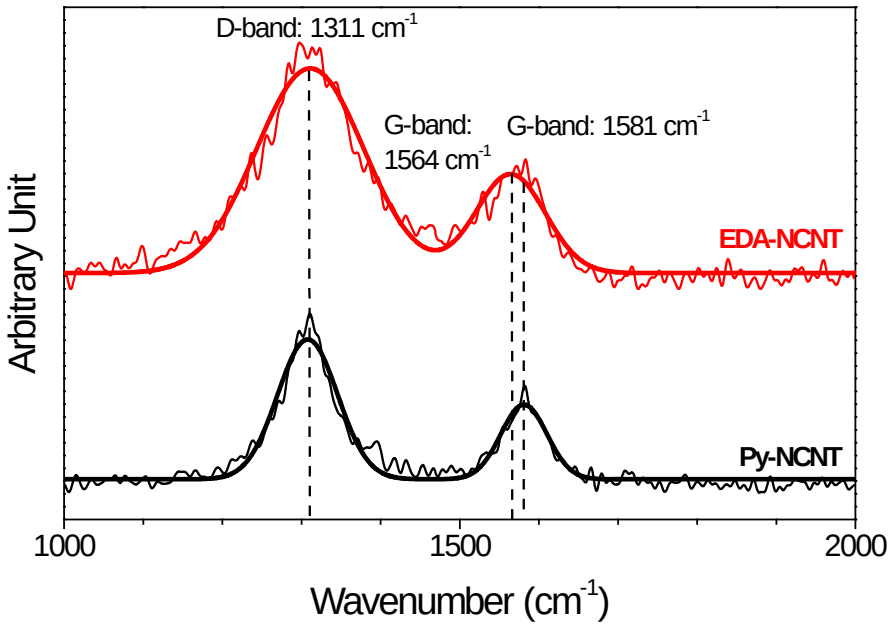

Figure 31 Raman spectrum of EDA-NCNT and Py-NCNT.

3.4 Conclusions and remarks

The high ORR activity observed for EDA-NCNT and additional benefits of CNT such as superior mechanical[153] and thermal properties[154] and low cost make EDA-NCNT a potential material to replace platinum based catalysts in the air electrodes. Through the comparison of EDA-NCNT and Py-NCNT, the effect of nitrogen precursors on nitrogen content and the fundamental role of surface nitrogen groups in the ORR activity were demonstrated. As a

conclusion, EDA-NCNT containing high nitrogen content is a promising material for the ORR catalysis in metal-air battery.

4 Effects of precursor composition on the ORR activity of NCNT

Investigation 2

Higgins, D., Chen, Z., and Chen, Z. Nitrogen doped carbon nanotubes synthesized from aliphatic diamines for oxygen reduction reaction. Electrochimica Acta. (2011) 56: 1570-1575.

Investigation 3

Chen, Z., Higgins, D., and Chen, Z. Nitrogen doped carbon nanotubes and their impact on the oxygen reduction reaction in fuel cells. Carbon. (2010) 48: 3057-3065.

4.1 Purpose of the study

Investigation 2

Based on the study presented in Chapter 3, the structure of the carbon and nitrogen precursors are confirm to be influential towards the ORR activity of the NCNT. To recapitalize, the use of different in carbon precursor leads to the formation of NCNT with varying nitrogen content. The difference in nitrogen content was attributed to the structure of the precursor molecules used was vastly different, with Py having a cyclic hydrocarbon ring and EDA having a linear hydrocarbon chain. The different in the precursor molecular structure can influence the decomposition of the molecule and how the decomposed hydrocarbon fragments rearrange and self-assemble. To confirm this hypothesis would be very difficult and is outside of the scope of this study. As a result, the use of precursor with similar structures but varying carbon to nitrogen composition

was used to observe the effect on NCNT formation. Specifically, EDA, 1, 3-diaminopropane (DAP) and 1, 4-diaminobutane (DAB) are used as carbon and nitrogen precursors. The resultant NCNT are name accordingly as, EDA-NCNT, DAP-NCNT and DAB-NCNT. Note, ED-NCNT and EDA-NCNT are used interchangeably in this section.

Investigation 3

In a separate study, Py were mixed with ethanol to reduce the overall nitrogen content in the precursor solution hoping to control the final nitrogen content of the NCNT. The purpose of this study was to further elucidate the influence the dependence of nitrogen content on the precursor solution and the effect on final ORR activity. Although ample studies investigated the effect nitrogen content on the NCNT morphology and microstructures[157, 158], a systematic study on the direct effect of nitrogen content on ORR activities has not been reported. In this study the impact of nitrogen content on the ORR activities of NCNT is investigated. The synthesis of NCNT was carried out by a single step CVD technique using a solution containing pyridine, ethanol and ferrocene. Through changing the pyridine to ethanol ratios of the stock solution, the relative amount of nitrogen in the growth environment during synthesis can be controlled. This approach allowed the direct comparison of the ORR activities of NCNT possessing different nitrogen contents.

4.2 Experimental methods

In the first study, the NCNT synthesis was carried out by the same methodology as described in section 2.1. Briefly ferrocene (98%, Aldrich) was used as a catalyst and ethylenediamine (98% EMD Chemicals), 1, 3-diaminopropane (99%, Aldrich) or 1, 4-diaminobutane (99%, Aldrich)

was used as the carbon and nitrogen precursor. In the second study the NCNT synthesis, the precursor solution was prepared by mixing the pyridine and ethanol at certain volume ratio followed by the dissolution of the ferrocene. The remainder of the synthesis is the same as described in section 2.1. Briefly ferrocene (98%, Aldrich) was used as a catalyst and pyridine (99% Caledon Laboratory Chemicals) mixed with ethanol (reagent grade) was mixed to form the precursor solution. After synthesis, SEM (LEO FESEM 1530, 20 eV) was used to investigate the overall morphology of NCNT. TEM (PHILIPS CM300) was used to examine the graphitization of the NCNT walls and to observe defected sites. XPS (Thermal Scientific K-Alpha XPS spectrometer, 150 eV) was used to investigate the relative content of different elements and the intensity of different nitrogen groups in the NCNT. EDX was used to evaluate the elemental composition of the NCNT samples. Electrocatalytic activity was evaluated using RRDE voltammetry. The instruments used include a biopotentiostat and a rotation speed controller (Pine Research Instrumentation). The RRDE experiments were carried out according to the protocols outlined in section 2.8.

4.3 Results and discussions

Investigation 2

TEM studies were carried out for the NCNT synthesized from EDA, DAP and DAB, respectively having a carbon to nitrogen ration of 1:1, 3:2 and 2:1 (Figure 32). The diameter of EDA-NCNT and DAP-NCNT are similar while DAB-NCNT showed larger diameter (around 40 nm). Additionally, with increasing number for carbon to nitrogen ratio, the graphitic wall of the NCNT showed fewer defects. For EDA-NCNT, small and round bamboo compartments are apparent, whereas the compartments became smaller and adapt a wedge-like appearance for

DAP-NCNT. The DAB-NCNT however, showed fewer well-defined bamboo apartments and the interior of NCNT were divided in the small compartments by few layers of graphitic sheets.

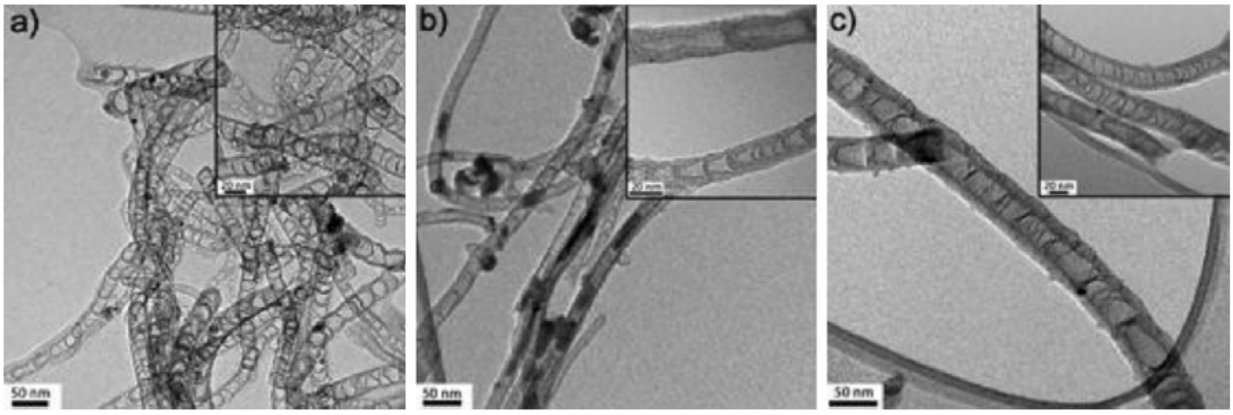

Figure 32 TEM image of the EDA-NCNT, DAP-NCNT and DAB-NCNT.

The decrease in structural defects was confirmed by Raman spectroscopy whereby the intensity ratio of the Raman active D- to G-bands was highest for the EDA-NCNT (2.07) and decreases to 1.41 for DAP-NCNT and 1.35 for DAB-NCNT. From the XPS analysis (Figure 33), the EDA-NCNT showed highest nitrogen content of 4.74 at. % followed by DAP-NCNT (2.48 wt. %) and DAB-NCNT (1.20 at. %).

Element	ED-CNT (at.%)	DAP-CNT (at.%)	DAB-CNT (at.%)
Carbon	91.50	92.77	94.66
Nitrogen	4.74	2.48	1.20
Oxygen	3.38	4.48	4.08
Iron	0.38	0.27	0.06

Figure 33 Elementary composition of the NCNT samples by XPS analysis.

HR-XPS study of the N 1s signal illustrates three contributions towards the surface nitrogen species by deconvoluting the N 1s spectrum. In all cases, the quaternary/pyrrolic nitrogen

constitutes over half of the surface nitrogen species followed by the pyridinic for EDA-NCNT and the pyrrolidone for DAP-NCNT and DAB-NCNT.

The ORR performance of NCNT synthesized in this study was investigated by the RRDE voltammetry. The polarization curves of the NCNT samples are showed in Figure 34. The apparent improvement in the ORR activity of EDA-NCNT over the other species can be attributed to the surface defects and the higher nitrogen content. The H_2O selectivity of EDA-NCNT is also higher compared to the other sample showing the greatest difference around -0.4 V vs. Ag/AgCl.

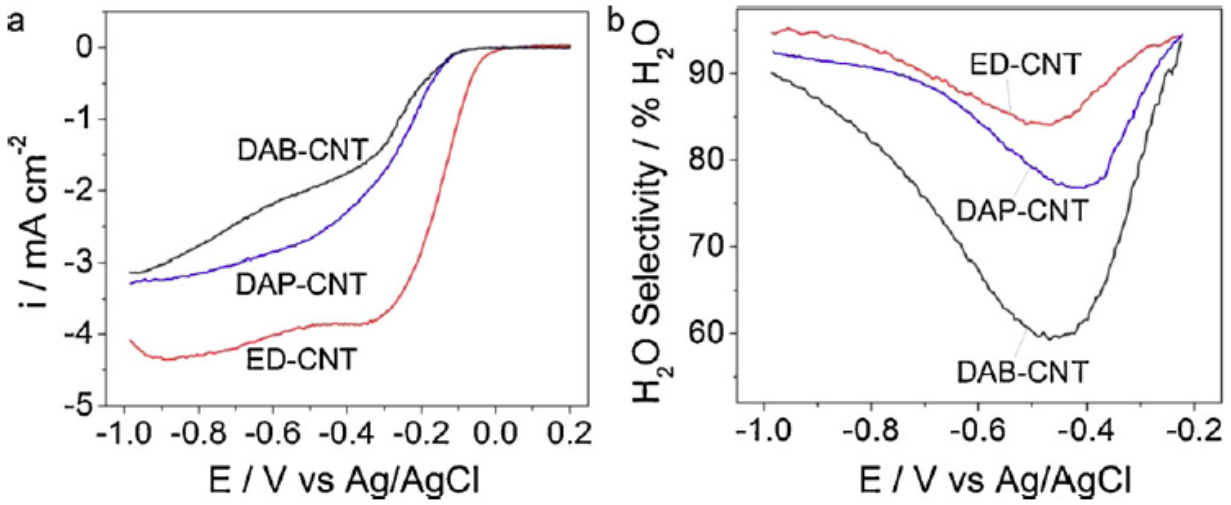

Figure 34 ORR polarization (a) and % H_2O selectivity (b) of EDA-, DAP- and DAB-NCNT.

Investigation 3

SEM images of the NCNT samples are shown in Figure 35. The SEM images showed similar morphology of the NCNT samples with high degree of alignment. However, increase in diameter

is observed with NCNT sample with lower nitrogen content similar to results from literatures[142, 143].

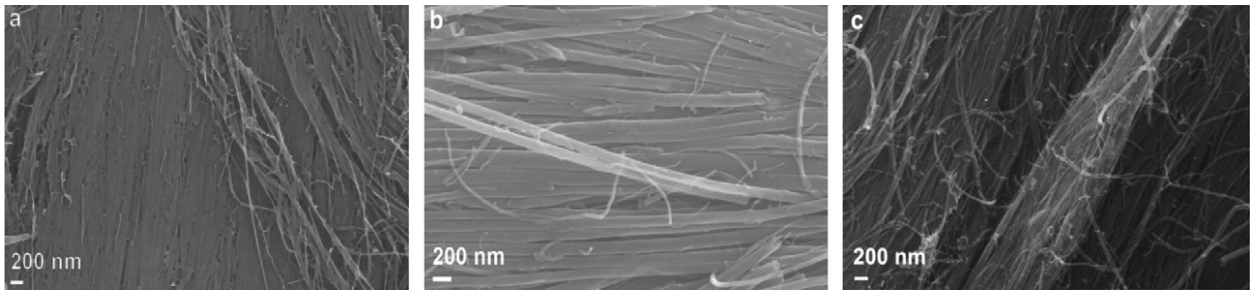

Figure 35 SEM of a) NCNT-a, b) NCNT-b and c) NCNT-c.

From Figure 36, TEM analysis carried out on the NCNT-a sample illustrates the formation of bamboo structures, a common feature found in NCNT[144, 145]. The formation of bamboo like compartments is caused by the presence of pentagon structures in the graphite network due to nitrogen doping[126]. Additionally, surface defects in the form of graphite plane edges are clearly visible from Figure 36, resulting from the incorporation of nitrogen atoms.

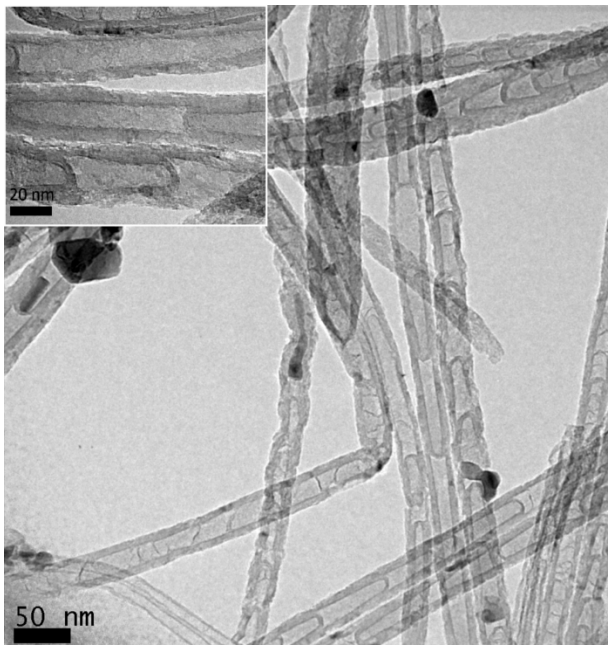

Figure 36 TEM images of NCNT-a showing bamboo structure and surface.

EDX was used to investigate the elemental compositions of the NCNT samples. From EDX analysis, the elemental compositions from highest to lowest in NCNT samples is carbon, oxygen, nitrogen and iron. The presence of oxygen is owing to the sample exposure to air after growth at 400 °C for the purpose of amorphous carbon removal. The residual iron catalyst after acid treatment contributed to the iron detected by EDX. Results from EDX analysis are summarized in Table 9. A more detailed analysis on the surface elemental compositions of the NCNT samples using XPS analysis will be presented later in this paper.

Table 9 Elemental composition NCNT samples by EDX.

Composition	NCNT-a (at. %)	NCNT-b (at. %)	NCNT-c (at. %)
Carbon	92.75	92.34	88.57
Nitrogen	3.28	2.84	2.51
Oxygen	3.96	3.92	8.20
Iron	N/A	N/A	0.72

The electrocatalytic activities of NCNT were evaluated by the RRDE voltammetry in alkaline conditions. Higher disc current density and lower ring current density are observed in Figure 37 for samples with higher nitrogen content.

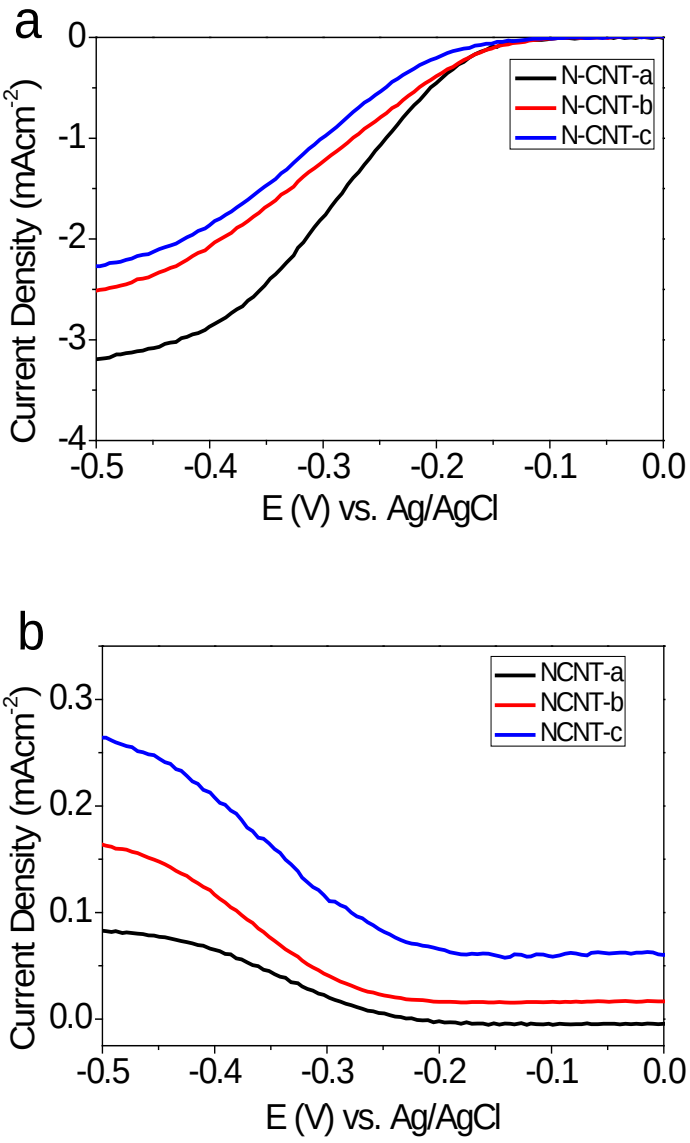

Figure 37 Polarization disk current (a) and ring current (b) of NCNT-a, NCNT-b and NCNT-c.

A summary of the ORR performance indicators is showed in Table 10. The half wave potential and limiting current density were obtained from the polarization curves. The number of electrons transferred and H_2O selectivity can be calculated using equation (17) and (18) from section 2.8.

.

In general an improvement to ORR performance is observed as nitrogen content in NCNT samples increases based on the data presented in Table 10. However, only minor improvement on half wave potential (~0.01 V) is observed for NCNT samples with higher nitrogen content. Additionally, the onset of the reduction does not vary much with an increase in nitrogen content. These minor improvements of onset and half wave potentials can be explained by the slight increase in nitrogen content between the samples. For example, comparing NCNT-b to NCNT-a, only 0.44 at. % difference in nitrogen content was observed (based on Table 10).

Table 10 Summary of the important ORR performance indicators.

	Half Wave Potential (V)	Limiting Current Density ($mAcm^{-2}$, at 2500 rpm)	No. of Electrons Transferred (at 2500 rpm, -0.5 V)	H_2O Selectivity (%, at 2500 rpm, -0.5 V)
NCNT-a	-0.29	-3.19	3.63	81.82
NCNT-b	-0.30	-2.52	3.20	59.88
NCNT-c	-0.31	-2.26	2.76	38.16

In terms of H_2O selectivity, significant improvement from 38.16% (NCNT-c) to 81.82% (NCNT-a) is observed. H_2O selectivity provides information on the reduction mechanisms the molecular oxygen follows during the electrochemical reaction. As proposed by Yeager *et al.*, ORR can occur through a four electron pathway where molecular oxygen is reduced to form H_2O or, a two electron pathway where molecular oxygen is reduced to hydrogen peroxide—an intermediate that will be further reduced to form H_2O[159]. Consequently, a higher H_2O selectivity

value is an indication of the more efficient four electron pathway being the dominant reaction mechanism during the electrochemical reaction. For conventional carbon electrodes in acidic and alkaline conditions, the ORR generally follows the two electron pathway[160]. Based on the observed H_2O selectivity values, the NCNT-c sample containing the lowest nitrogen content behaved in this manner with the two electron pathway being the dominant mechanism during ORR. On the contrary, ORR followed the four electron pathway for the NCNT-a sample containing the highest nitrogen content.

In terms of limiting current density, a higher value was obtained with higher nitrogen concentration. In particular, the limiting current density of NCNT-a increased 41% compared with NCNT-c for a only a small increment in nitrogen content. This result suggests that NCNT-a sample contains more active sites for ORR compared with NCNT-c. Such a conclusion is expected as nitrogen containing sites have been considered as active sites for ORR, thus higher nitrogen content can be correlated with higher limiting current densities. Based on the analysis of limiting current density and H_2O selectivity, significant improvements to these parameters suggests that nitrogen doping has a significant effect in influencing the ORR reaction pathway and catalytically active sites. On the contrary, minor improvements to onset and half wave potentials suggest a minimal influence of nitrogen doping on ORR in the kinetically limited regime.

ORR performance of the NCNT catalysts in the diffusion and kinetically limited regime can be evaluated using K-L plots. Figure 38 shows the K-L plots and polarization curves of NCNT catalysts at different potentials and rotation speeds respectively. Based on Figure 38, a linear

relationship is observed for 1/j and $\omega^{-1/2}$. In addition, for all NCNT samples the Levich slope showed minor variations at applied potentials, which is an indication of first order kinetics of ORR[161, 162].

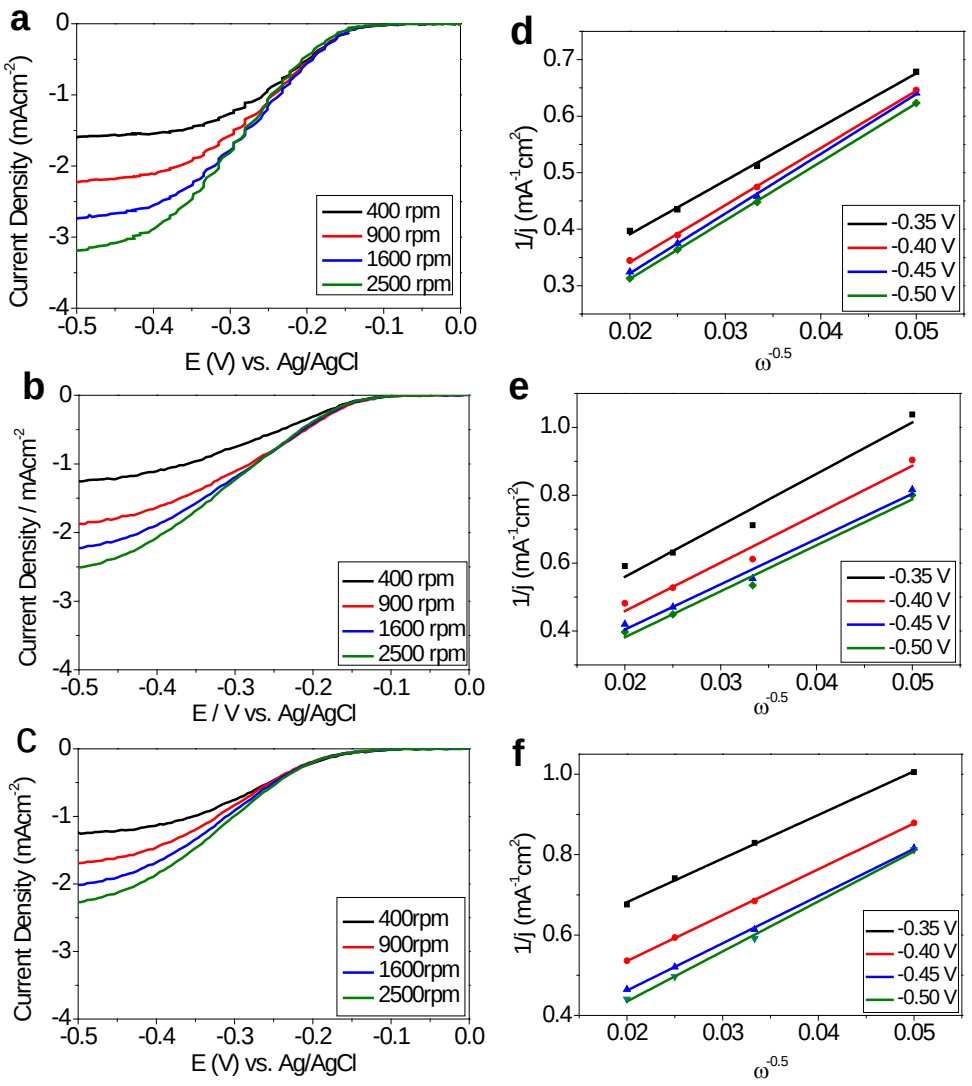

Figure 38 Polarization curve of a) NCNT-a, b) NCNT-b, c) NCNT-c for oxygen reduction in 0.1 M of potassium hydroxide saturated with O_2, and Koutecky-Levich plot of d) NCNT-a, e) NCNT-b and f) NCNT-c.

By extrapolation of the linear K-L lines to the origin of the plot, or as ω approaches∞, the Y - intercept yields the kinetic current density. The kinetic current densities of different NCNT samples at various potentials are tabulated in Table 11 where higher kinetic current density is observed for higher nitrogen content samples.

Table 11 Kinetic current density of different NCNT samples at various potentials

Potential	NCNT-a	NCNT-b	NCNT-c
E (V) vs. Ag/AgCl	j_k ($mAcm^{-2}$)	j_k ($mAcm^{-2}$)	j_k ($mAcm^{-2}$)
-0.35	4.97	3.90	2.15
-0.40	7.19	5.77	3.26
-0.45	9.04	7.27	4.40
-0.50	9.53	9.02	5.37

Tafel analysis can be used to evaluate the ORR kinetics and adsorption mechanisms of oxygen on the NCNT catalysts. By plotting the applied potential versus the logarithm of measured current density, a Tafel plot can be generated. The linear regions in the Tafel plot can be modelled by the empirical Tafel equation as shown below.

$$\eta = \alpha + \beta * \log|j| \qquad (19)$$

In equation 19, η is the overpotential, j is the measured current density, b is the Tafel slope and α is a constant. The Tafel plots of different NCNT samples are showed in Figure 39. Two distinct linear regions are displayed in the Tafel plots in the low and high current density regions. The double Tafel slopes is often observed for platinum based electrocatalysts where the value of these Tafel slopes at low and high current density is -0.06 V per decade and -0.12 V per decade respectively[163, 164]. The Tafel slopes of NCNT-a are close to that of platinum based catalysts whereas the Tafel slopes of NCNT-b and NCNT-c showed greater values. Since a lower value of Tafel slope is desirable, high Tafel slope values indicate inferior ORR activities. Within the three

NCNT samples, NCNT-a, with the highest nitrogen content showed the smallest Tafel slopes indicating positive impacts of nitrogen content on ORR kinetics, consistent with analysis from the previous sections. From the Tafel plots, by extrapolation of the linear Tafel relationships to zero potential, the X-intercept obtained is the exchange current density. Owing to the negative sloping nature of Tafel slopes, a higher Tafel slope would generate a lower exchange current density. Hence for NCNT samples, NCNT-a having the highest nitrogen content will have the highest exchange current density.

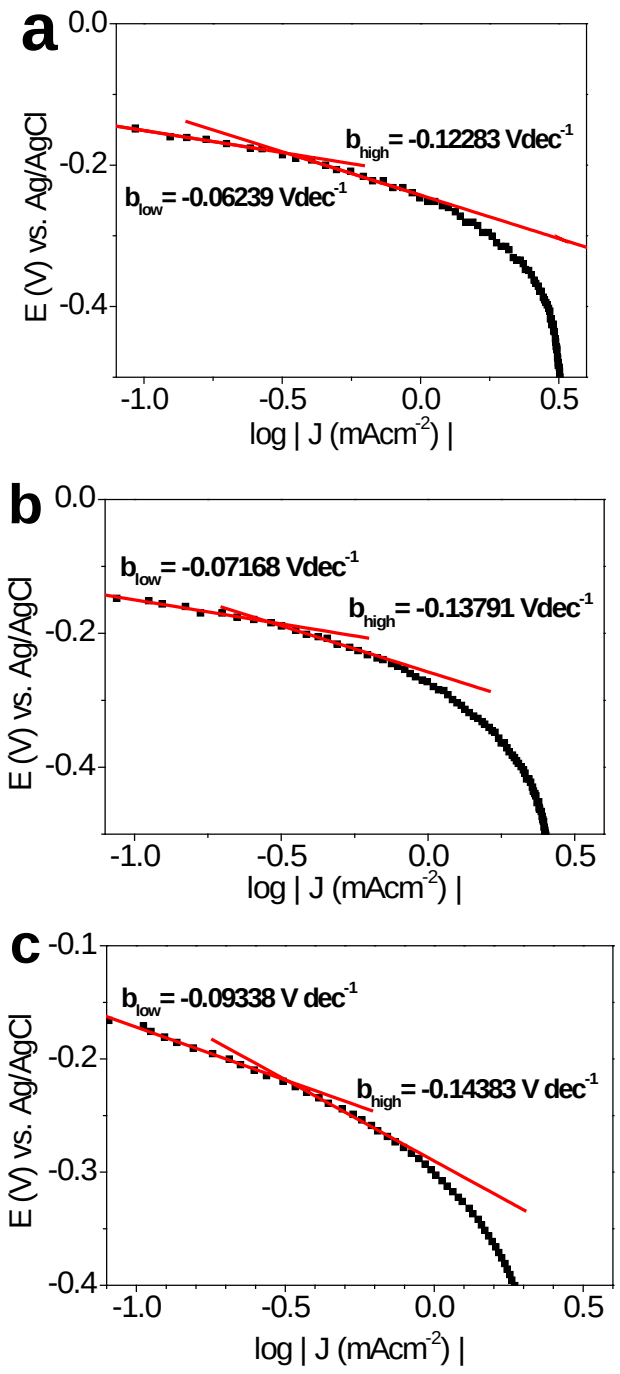

Figure 39 Tafel plot of a) NCNT-a, b) NCNT-b, c) NCNT-c.

In terms of the oxygen adsorption mechanism, molecular oxygen adsorbs onto the oxide containing platinum surfaces following the Temkin adsorption isotherm in the low current

density region, whereas in the high current density region, molecular oxygen adsorbs onto the pure platinum surface following the Langmuir adsorption isotherm[163, 164]. The existence of two Tafel slopes for NCNT samples indicates the existence of similar oxygen adsorption mechanism compared to platinum based catalysts.

ORR typically occurs on the surface active sites of catalysts, thus understanding the distribution of surface nitrogen atoms and the bond formation with carbon atoms of the graphite network is critical. The surface nitrogen groups were identified with XPS due to the high surface sensitivity of the catalyst materials. A summary of elemental composition of NCNT sample is shown in Table 12 where NCNT-a displayed higher nitrogen content compared to the other two NCNT samples. The trend of increasing nitrogen content with respect to increasing nitrogen precursor proportion in the stock solution was expected as a higher nitrogen precursor proportion creates a nitrogen rich environment during synthesis. The observed trend agrees with reported literature where higher nitrogen content in the NCNT was correlated with higher nitrogen proportion in the growth environment[165].

Table 12 Elemental compositions of NCNT samples from XPS analysis.

	NCNT-a		NCNT-b		NCNT-c	
	Peak Position (eV)	At. %	Peak Position (eV)	At. %	Peak Position (eV)	At. %
Carbon	284.61	92.70	284.68	95.04	284.66	97.06
Nitrogen	400.41	2.35	400.94	1.27	400.59	0.70
Oxygen	532.40	4.75	532.70	3.61	532.09	2.21
Iron	707.39	0.20	707.34	0.08	708.20	0.04

The formation of different surface nitrogen groups was revealed by detail analysis of the N 1s spectra showed in Figure 40.

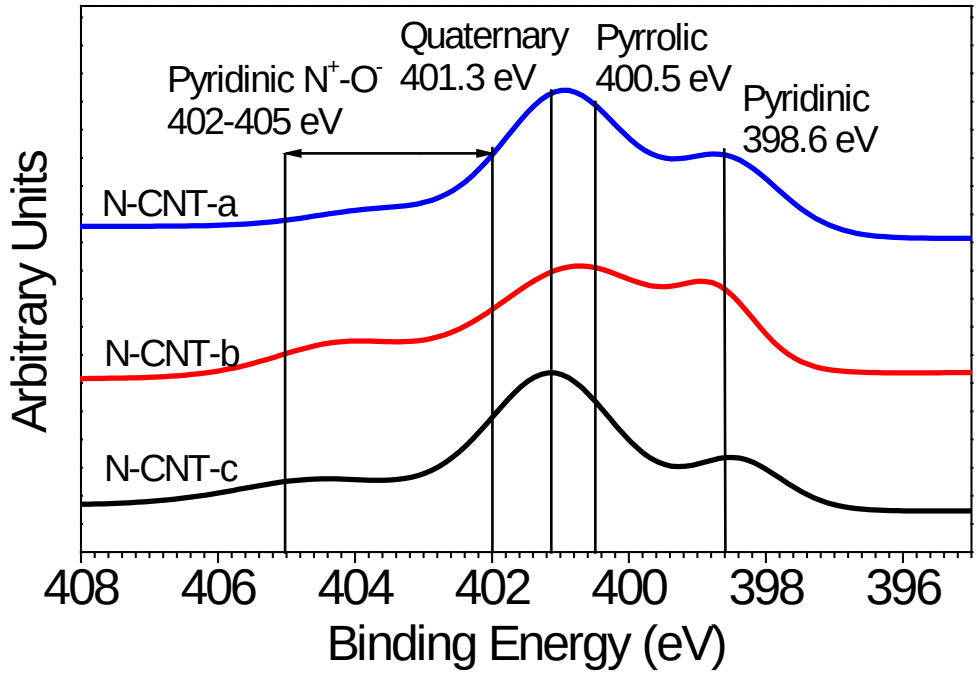

Figure 40 HR-XPS of the N 1s signals of NCNT.

Table 13 summarized the peak position of different types of surface nitrogen group and corresponding contributions to the total surface nitrogen content.

Table 13 HR-XPS analysis of the N 1s signal.

	NCNT-a		NCNT-b		NCNT-c	
	Peak Position (eV)	At. %	Peak Position (eV)	At. %	Peak Position (eV)	At. %
Quaternary / Pyrrolic	400.75	68.20	400.74	66.28	401.12	65.94
Pyridinic	398.47	14.83	398.70	17.69	398.42	17.41
Pyridone	404.87	16.96	404.20	16.02	404.49	16.65

The quaternary/pyrrolic nitrogen group with binding energy of 400.7 eV (NCNT-a and NCNT-b) and 401.1 eV (NCNT-c) constituted greater than 65 % of the total N 1s signals is considered the dominant surface nitrogen group. The preferred formation of quaternary/pyrrolic nitrogen groups at low nitrogen content is commonly observed in literature[142, 143]. In close proximity the binding energy of pyrrolic and quaternary nitrogen groups at 400.5 eV and 401.3 eV respectively forms a peak, which suggests the coexistence of pyrrolic and quaternary nitrogen groups. However, pyrrolic nitrogen groups are considered the dominant nitrogen group for NCNT-a and NCNT-b as the corresponding N 1S signal at 400.75 eV and 400.74 eV is in closer proximity to the binding energy of pyrrolic nitrogen groups. Similarly, quaternary nitrogen groups are considered the dominant nitrogen group for NCNT-c as the corresponding N1s signal at 410.3 eV is in closer proximity to the binding energy of quaternary nitrogen groups. Through coupling the XPS and RRDE results, NCNT-a and NCNT-b containing more pyrrolic nitrogen groups showed better ORR performance compared to NCNT-c sample containing more quaternary nitrogen groups. The observed correlation of ORR activities with respect to nitrogen groups could be explained by the theory regarding the edge plane nitrogen groups (pyrrolic or pyridinic) being the active site for ORR due to the lone pair electrons[165]. Pyridinic nitrogen with a binding energy of 398 eV constitutes less than 20% of the total N1s signal which agrees with reported results regarding unfavourable formation of pyridinic nitrogen at low nitrogen concentration[142, 166]. When a nitrogen atom is added to the graphite network, it disrupts the normal bonding configuration between carbon atoms and there is an energy barrier associated with the energy cost of adding additional nitrogen atoms to the graphite network. This energy cost is realized in the form of heat of formation which shows an increasing trend with respect to overall nitrogen content until it reaches a high nitrogen content after which it decreases drastically. This trend is

observed for corrugated graphite network, which is closely related to the pyridinic nitrogen group formation. As a result, the pyridinic nitrogen group exhibits low heat of formation at higher nitrogen content, which explains its more favourable formation at higher nitrogen content[166]. According to literature, N 1s signals around 404 eV can be attributed to pyridone N^{+}-O^{-} groups which are formed when oxygen is present during the pyrolysis of nitrogen containing carbon materials[150, 167]. In this experiment, the reaction between oxygen and nitrogen during growth is possible as the synthesis was carried out in ambient pressure.

The C1s signal centred at 284.66 can be dissected into three peaks as showed in Figure 41. The dominant peak at 284.61 corresponds to sp2 hybridized graphitic carbon[157]. The symmetry of this peak indicates only a small amount of disruption to the perfect graphitic structure has occurred by nitrogen doping which is consistent with the low nitrogen content observed. Two small peaks centred at 285.47 eV and 286.29 eV correspond to the binding energy of the carbon to quaternary nitrogen and carbon to pyridine nitrogen respectively[157]. The peak intensity of carbon to pyridinic nitrogen for NCNT-a, NCNT-b and NCNT-c indicates the similar pyridinic nitrogen group contents between the NCNT samples which agrees with the analysis of N 1s signals.

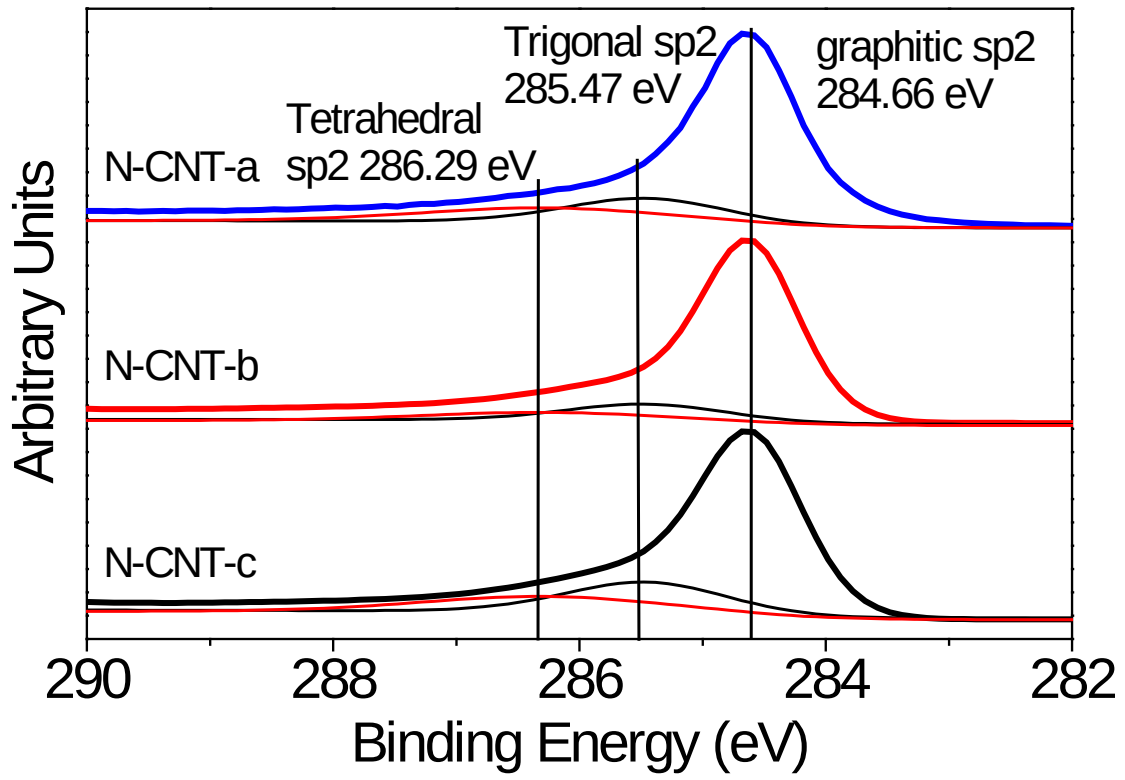

Figure 41 HR-XPS of the C 1s signals of NCNT samples.

4.4 Conclusions and remarks

NCNT with different nitrogen content were obtained by changing the proportion of nitrogen precursor in the stock solution. This goal was achieved via two approaches, one is to use precursor solution with varying carbon to nitrogen ratio; and second is to combine two hydrocarbons—one being solely the carbon precursor together at different proportions. Based on RRDE voltammetry studies, higher nitrogen content of the resultant NCNT was showed to be important for the improvement of ORR activities. While the highest ORR performance was achieved for the NCNT sample with the highest N content, there exist some discrepancies. Higher nitrogen content was showed to have significant impact on the limiting current density and H_2O selectivity for both investigations. Thus it is safe to conclude that, employing different

nitrogen ratios of the precursor molecule and in the precursor solution influence the nitrogen contents in NCNT which are important in attaining high ORR activities. However, the HWP improvement by the NCNT with highest N content in Investigation 2 was more significant compared to that observed in Investigation 3. Clearly, other factors must be influencing the ORR activity asides from the overall nitrogen contents.

5 Effects of surface structure on the ORR activity of NCNT

Chen, Z., Higgins, D., and Chen, Z. Electrocatalytic activity of nitrogen doped carbon nanotubes with different morphologies for oxygen reduction reaction. Electrochimica Acta. (2010) 55: 4799-4804.

5.1 Purpose of the study

NCNT synthesized by chemical vapor deposition have shown promising ORR activity by many studies [169-173]. In the paper by Gong et al.[102], NCNT were synthesized using CVD technique by the pyrolysis of iron (II) phthalocyanine either under the presence or absence of ammonia gas. The ORR activity of the synthesized NCNT was showed to be superior compared to platinum based materials in alkaline conditions. The observed ORR activity of NCNT has been directly attributed to increased nitrogen content and more edge plane exposure[102, 174, 175]. By using non-gaseous nitrogen precursors such as triazine and pyridine, a nitrogen content of 2-9 at. % has been obtained[141, 144]. Moreover, studies using a gaseous nitrogen species such as NH3 as nitrogen dopant have reported an improvement of the nitrogen content in NCNT[176-178]. Many researchers have hypothesized the catalytic effect of metals on the formation of nitrogen containing active sites in NCNT [126, 150, 179, 180]. Also, the impact of metal catalyst precursors on the morphology of carbon nanostructures has been investigated in many studies [181-185], with focus on the effects of different metals (i.e. Fe versus Co) and their supports (i.e. Fe/SiO_2 versus Fe/MgO) on the surface morphology of NCNT[186]. However, catalysts containing the same metal atom but

different molecular structures have received little attention towards their effect on surface structure and ORR activity.

In the present work, NCNT were prepared via a single step CVD technique, using either ferrocene or iron (II) phthalocyanine as catalyst and pyridine as a carbon and nitrogen precursor. This approach allowed the direct comparison of the effect of catalyst structure on the synthesized NCNT where the structural variations between ferrocene based NCNT (Fc-NCNT) and iron (II) phthalocyanine based NCNT (FePc-NCNT) were investigated using transmission electron microscope (TEM) and Raman spectroscopy. The electrocatalytic activity of Fc-NCNT and FePc-NCNT towards ORR in alkaline conditions has been evaluated using rotating ring disc electrode (RRDE) voltammetry and analysed based on the morphology of each sample. This study provides new insight regarding the improvement of ORR activity by modifying the structural properties of NCNT as opposed to the conventional method of increasing nitrogen content.

5.2 Experimental methods

NCNT synthesis methodology is outlined in section 2.1. Briefly ferrocene (98% Aldrich, FeC10H10) or iron (II) phthalocyanine (~90% Aldrich, C32H16FeN8) and the carbon and nitrogen precursor is pyridine (99% Caledon Laboratory Chemicals). After synthesis, SEM (LEO FESEM 1530, 20 eV) was used to investigate the overall morphology of NCNT. TEM (PHILIPS CM300) was used to examine the graphitization of the NCNT walls and to observe defected sites. XPS (Thermal Scientific K-Alpha XPS spectrometer, 150 eV) was used to investigate the relative content of different elements and the intensity of different nitrogen groups in the NCNT.

EDX was used to evaluate the elemental composition of the NCNT samples. Electrocatalytic activity was evaluated using RRDE voltammetry. The instruments used include a biopotentiostat and a rotation speed controller (Pine Research Instrumentation). The RRDE experiments were carried out according to the protocols outlined in section 2.8.

5.3 Results and discussions

Alignment between individual nanotubes from Fc-NCNT (Figure 42a) and FePc-NCNT (Figure 42b) was observed with SEM. The SEM images show similar length and diameter for the Fc-NCNT and FePc-NCNT.

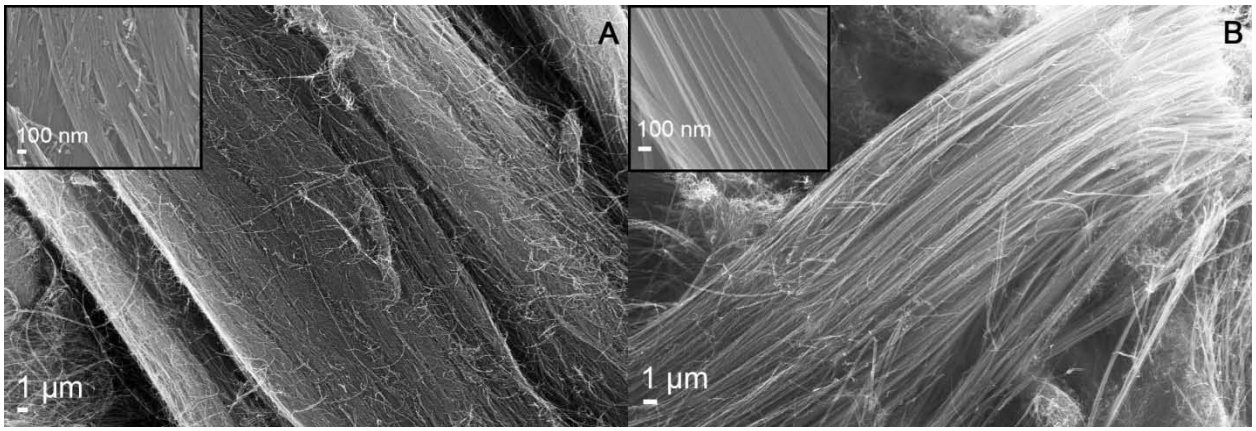

Figure 42 SEM image of A) Fc-NCNT and B) FePc-NCNT.

EDX was performed simultaneously with SEM. From EDX analysis, the elemental composition from highest to lowest in the Fc-NCNT and FePc-NCNT was carbon, oxygen and nitrogen. The values of the compositional contribution of each element are listed in Table 14. The presence of nitrogen indicates successful doping of nitrogen into the CNTs. The similar nitrogen content between the two NCNT samples indicates the minor effect of the selected catalysts on the

nitrogen content of NCNT. The presence of oxygen was observed in both samples, caused by the introduction of air into the reaction environment at 400 °C after synthesis was completed.

Table 14 Elemental composition of Fc-NCNT and FePc-NCNT after acid leaching from EDX

Composition	Fc-NCNT (at. %)	FePc-NCNT (at. %)
Carbon	93.87	92.16
Nitrogen	2.70	2.91
Oxygen	3.43	4.93

The TEM micrographs in Figure 43 display the bamboo structures in the two NCNT samples. The formation of bamboo structure is common in NCNT due to the formation of pentagons caused by nitrogen substitution in the graphite network. The FePc-NCNT is characterized by a smooth, thick outer graphitic wall and a narrow hollow interior channel. The Fc-NCNT are characterized by a more rugged, relatively thinner outer graphitic wall, and a wider hollow interior. Decrease in NCNT diameter and wall thickness could be caused by nitrogen doping in NCNT would[187, 188], hence similar nitrogen content of Fc-NCNT and FePc-NCNT obtained from EDX and XPS data suggest similar graphite wall thickness and diameter. Based on the TEM images, similar NCNT diameter were obtained however the large variation of with respect to the graphite wall thickness is observed. These results suggest possible effects of catalyst in the graphitic wall formation of NCNT.

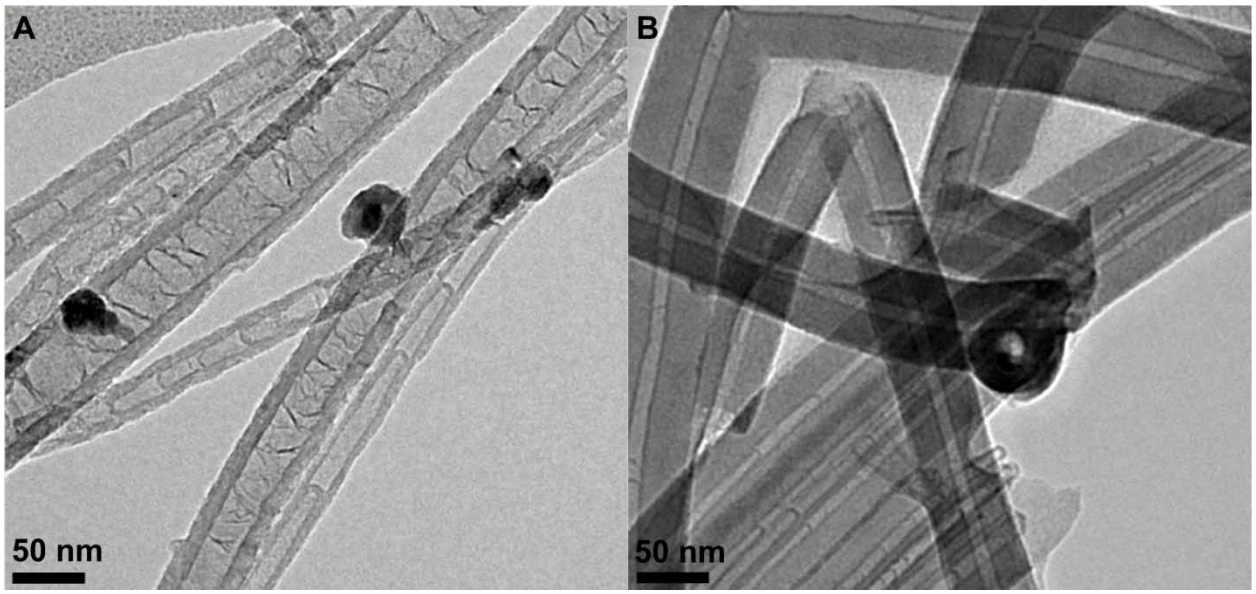

Figure 43 TEM image of A) Fc-NCNT and B) FePc-NCNT.

RRDE voltammetry was used to evaluate the electrocatalytic activity of the acid treated NCNT electrocatalysts (Figure 44).

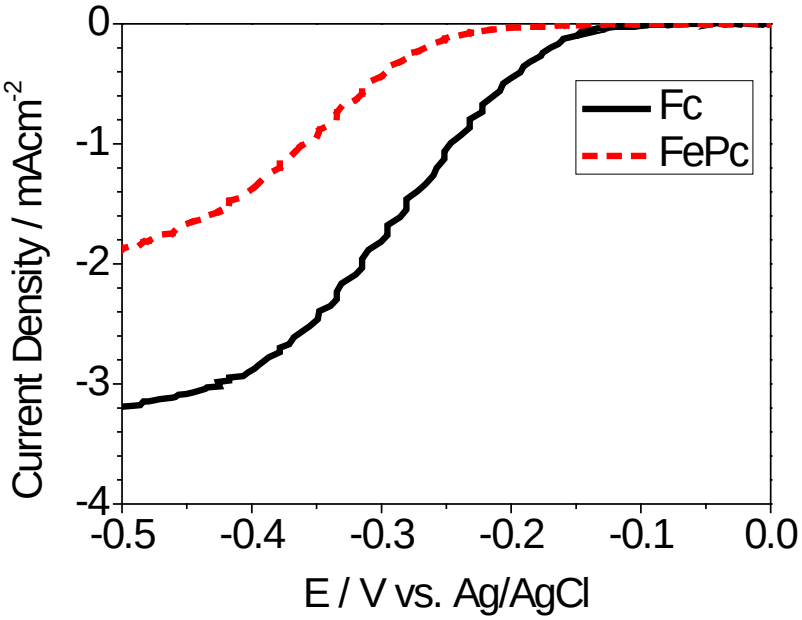

Figure 44 Polarization curve of Fc-NCNT and FePc-NCNT.

With respect to all the parameters investigated, Fc-NCNT having more defects showed superior ORR performance compared to the FePc-NCNT having fewer defects. Fc-NCNT with an OP of -0.12 V vs. Ag/AgCl compared to FePc-NCNT with an OP of -0.18 V vs. Ag/AgCl indicates a lower overpotential for the Fc-NCNT with respect to ORR. Furthermore, Fc-NCNT showed a 0.07 V improvement in HWP compared to FePc-NCNT indicating faster kinetics of Fc-NCNT which allows it to reach the limiting current density faster. With respect to the H_2O selectivity, a 12 % increase was observed in Fc-NCNT compared to FePc-NCNT at -0.5 V vs. Ag/AgCl. Higher H_2O selectivity of Fc-NCNT indicates a more effective ORR catalyst as it favors the formation of H_2O as opposed to the less efficient H_2O_2. The onset potential, HWP, limiting current density, number of electrons transferred in the reaction and H_2O selectivity are summarized in Table 2.

Table 15 Summary of the important performance indicator of ORR.

	Half Wave Potential (V)	Limiting Current Density ($mAcm^{-2}$)	Number of Electron Transferred (2500 rpm, -0.5 V)	H_2O selectivity (%) (2500 rpm, -0.5 V)
Fc-NCNT	-0.28 V	-3.19	3.63	81.82
FePc-NCNT	-0.35 V	-1.89	3.38	69.25

The K-L equation can be used to analyze the ORR kinetics of Fc-NCNT and FePc-NCNT. Based on the K-L plots of Fc-NCNT (Figure 45b) and FePc-NCNT (Figure 45d), similar slopes indicate the first order reaction kinetics of ORR in both NCNT electrocatalysts [149].

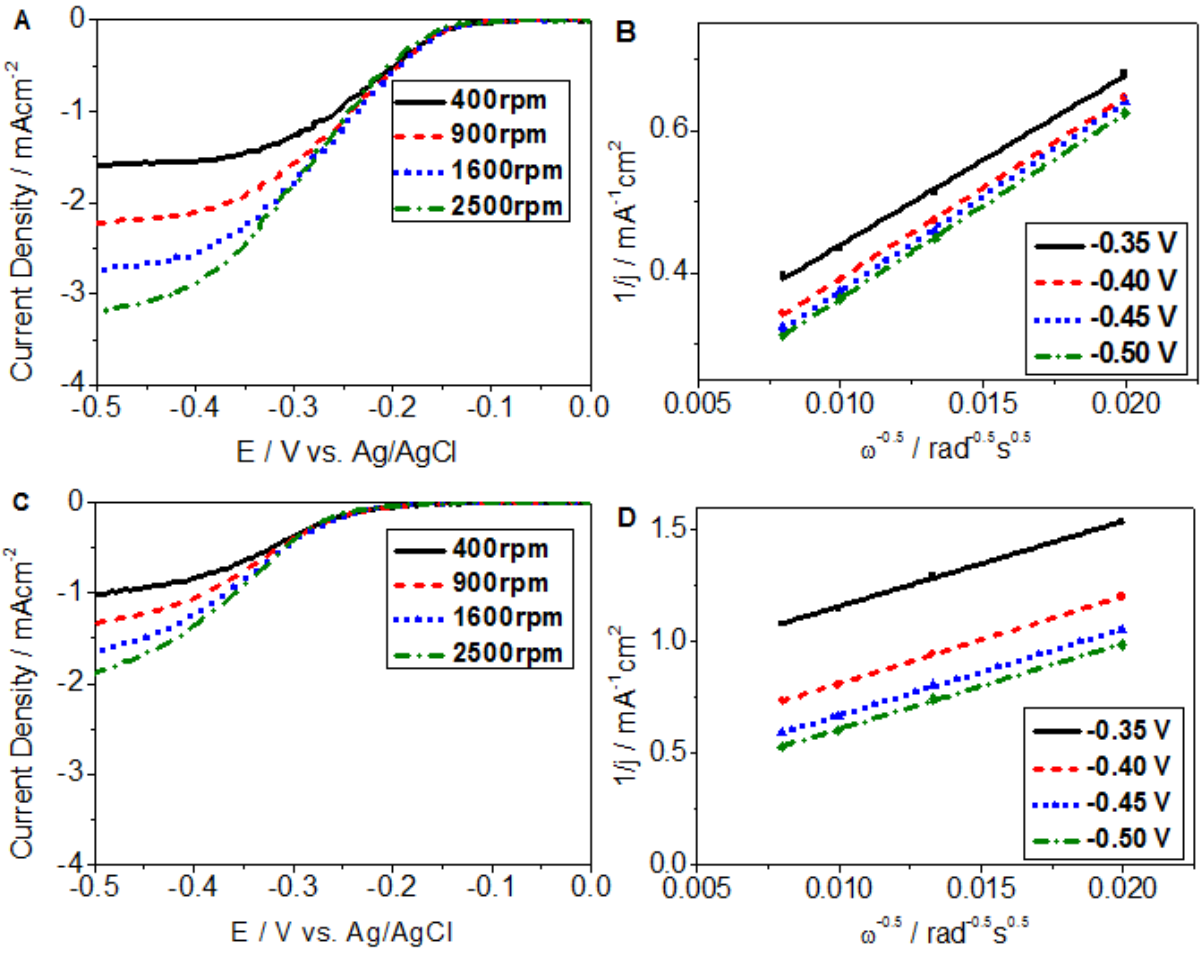

Figure 45 Polarization curves of A) Fc-NCNT and C) FePc-NCNT at different rotation speeds. K-L plots of B) Fc-NCNT and D) FePc-NCNT at different potential.

Furthermore, by taking the reciprocal of the Y-intercept of K-L plots at different potentials, the kinetic currents can be calculated. At the potential of -0.5 V, the kinetic current density of Fc-NCNT is 9.53 $mAcm^{-2}$, 115% higher compared to that of FePc-NCNT (Table 16).

Table 16 Kinetic current density of Fc-NCNT and FePc-NCNT at different potentials.

	Fc-NCNT	FePc-NCNT
E / V vs. Ag/AgCl	j_k / $mAcm^{-2}$	j_k / $mAcm^{-2}$
-0.35	4.97	1.29

-0.40	7.19	2.38
-0.45	9.04	3.51
-0.50	9.53	4.43

Tafel analysis can be used to analyze the kinetics of ORR and the adsorption of oxygen species on NCNT. The Tafel plots of Fc-NCNT and FePc-NCNT are characterized by two linear regions at low and high current density regimes due to the switching of oxygen adsorption mechanism followed by a sharp drop in the Tafel slope due to the impact of diffusion. For Pt/C the Tafel slope at low and high current density region is -0.06 $Vdec^{-1}$ and -0.12 $Vdec^{-1}$ respectively[142]. The Tafel slope of Fc-NCNT at low and high current density regime is -0.062 $Vdec^{-1}$ and -0.123 $Vdec^{-1}$ respectively (Figure 46a). The Tafel slope of FePc-NCNT at low and high current density regime is -0.08822 $Vdec^{-1}$ and -0.12364 $Vdec^{-1}$ respectively (Figure 46b). The two distinct linear regions of Tafel plot are caused by the switching between Langmuir adsorption and Temkin adsorption of oxygen on the Pt/C catalyst[142]. Hence, the similar Tafel slopes observed in Fc-NCNT showed similar oxygen adsorption mechanism compared to Pt/C catalyst. On other hand, FePc-NCNT having a Tafel slope of -0.088 $Vdec^{-1}$ at low current density region suggests a slightly different adsorption mechanism of oxygen species on FePc-NCNT.

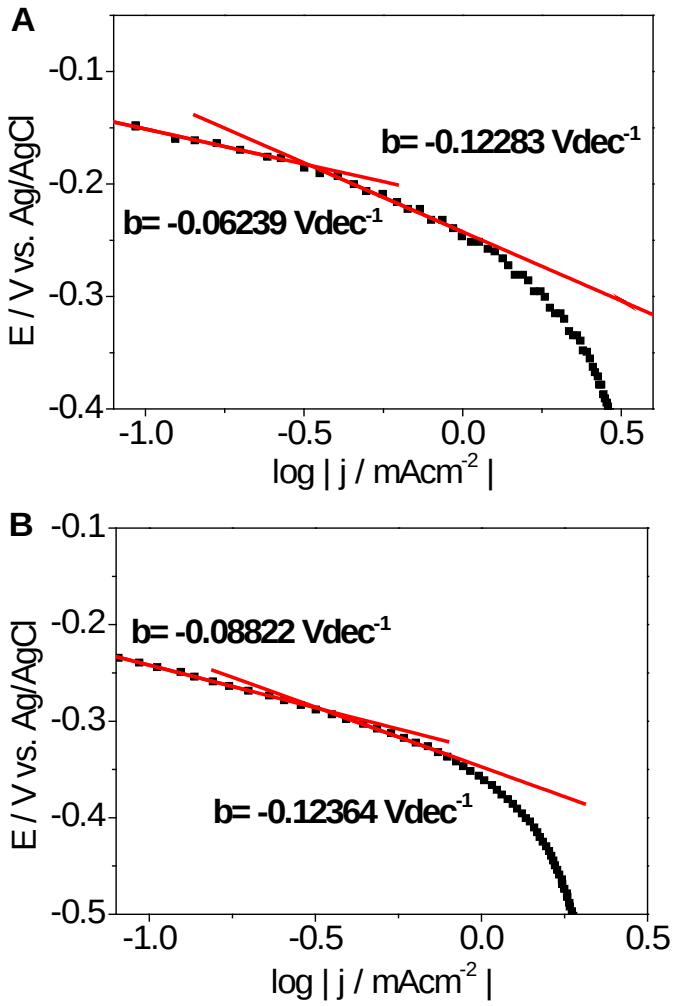

Figure 46 Tafel plot of A) Fc-NCNT and FePc-NCNT.

More accurate elemental composition and the identification of different nitrogen groups in Fc-NCNT and FePc-NCNT were obtained using XPS (Figure 47). Based on XPS results, Fc-NCNT showed similar overall nitrogen content compared to FePc-NCNT (2.35 at. % for the former and 2.48 at. % for the latter. The slightly higher nitrogen content of FePc-NCNT is due to the multiple nitrogen atoms in the structure of FePc catalyst which increased the amount of nitrogen available in the growth environment. Incorporation of nitrogen into the carbon network has been attributed to cause defect formation in NCNT [143, 178, 188], hence a slightly higher nitrogen content

of FePc-NCNT would suggest the formation of NCNT with more defects. This result is contradictory to the TEM results. This can be explained by the fact that at low overall nitrogen content (less than 3 at. %) the ordering of carbon atoms remains the dominant factor in forming the surface structure of NCNT. Since the only difference in the synthesis of Fc-NCNT and FePc-NCNT was the use of different catalyst, the formation of the surface structure of NCNT could be influenced by different catalyst structures. Furthermore, nitrogen content has been attributed to be a dominant factor influencing ORR performance [102, 174, 175], thus similar nitrogen content of Fc-NCNT and FePc-NCNT would suggest similar ORR performance. However, based on RRDE data, Fc-NCNT with more defects showed much superior ORR performance compared to FePc-NCNT containing lesser defects. Base on these ORR results, defects on the surface of NCNT can be very important towards ORR activity.

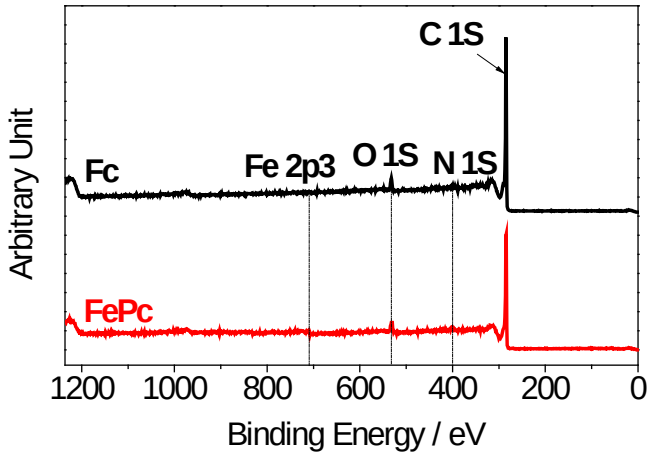

Figure 47 XPS spectrum of Fc-NCNT and FePc-NCNT.

Raman spectroscopy was used to investigate the degree of defects in the NCNT samples (Figure 48). Two peaks are found in the Raman spectrum of Fc-NCNT and FePc-NCNT centered at 1307.8 cm^{-1} and 1581.1 cm^{-1}. These two peaks correspond to the Raman active D and G-bands of NCNT. The D-band is attributed to the disorder in the NCNT structure[189] whereas G-band is

caused by the E_{2g} vibration mode of graphitic network[189]. As a result, the ratio of the intensity of the D- and G-band (I_D/I_G) reflects the degree of disorder in the NCNT where the disorder can be caused by defects due to nitrogen doping. From the Raman spectra, the I_D/I_G ratio of Fc-NCNT and FePc-NCNT was 1.87 and 1.22 respectively, indicative of a higher degree of defects in Fc-NCNT. This result is consistent with the structural characterizations and further illustrates the effect of catalyst structure on the surface structure of NCNT. In addition, similar electronic structure of the Fc-NCNT and FePc-NCNT is suggested by the similar position of the G-band in both samples[104].

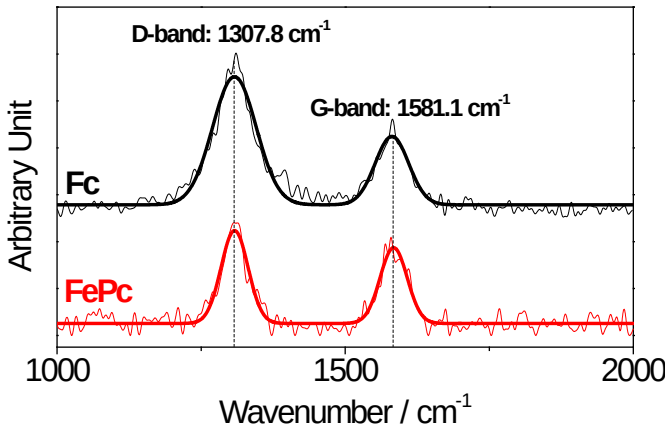

Figure 48 Raman spectrum of Fc-NCNT and FePc-NCNT.

5.4 Conclusions and remarks

Different catalyst structures were showed to have significant impact on the surface defects of the resultant NCNT as confirmed by various structural characterization techniques. The electrocatalytic activity of NCNT synthesized from catalysts with different structures was evaluated and significant differences were observed. Based on the difference in ORR kinetics,

the importance of surface defects towards ORR activity was confirmed. As a conclusion, increase the surface defects of NCNT using catalyst materials with different structures is a viable method to improve the electrocatalytic activity of NCNT

6 Evaluation of NCNT in prototype zinc-air battery

Zhu, S., Chen, Z., Li, B., Higgins, D., Wang, H., Li, H., Chen, Z. Nitrogen-doped carbon nanotubes as air cathode catalysts in zinc-air battery. Electrochimica Acta. (2011) 56: 5080-5084.

6.1 Purpose of the study

Previous sections, we have reported that highly active NCNT can be synthesized using an ethylenediamine/ferrocene precursor solution, with the resulting materials displaying superior ORR activity under alkaline conditions compared even with traditional platinum based catalyst materials [155, 156, 191]. Thus, we have adopted this strategy to utilize highly active NCNT based materials as air-cathode electrocatalysts in order to improve the performance of zinc-air batteries. The physiochemical properties of NCNT were extensively characterized by SEM and TEM. Electrochemical catalytic activity of NCNT was investigated by LSV using a RRDE system, which confirmed the excellent ORR activity in alkaline condition. Notably, the novelty of this work lies in the utilization of highly active NCNT as cathode catalyst materials in a single cell zinc-air battery setup. The single cell performance was investigated using electrochemical impedance spectroscopy (EIS) in different electrolyte concentrations. Utilization of NCNT has led to high zinc-air battery performance suggesting the great potential of NCNT as high performance catalyst for ORR on the air-cathode of zinc-air batteries.

6.2 Experimental methods

NCNT synthesis methodology is outlined in section 2.1. Briefly, ferrocene (98%, Aldrich) was used as a catalyst and ethylenediamine (98% EMD Chemicals) was used as a carbon and nitrogen precursor. After synthesis, SEM (LEO FESEM 1530, 20 eV) was used to investigate the overall morphology of NCNT. TEM (PHILIPS CM300) was used to examine the graphitization of the NCNT walls and to observe defected sites. XPS (Thermal Scientific K-Alpha XPS spectrometer, 150 eV) was used to investigate the relative content of different elements and the intensity of different nitrogen groups in the NCNT. EDX was used to evaluate the elemental composition of the NCNT samples. Electrocatalytic activity was evaluated using RRDE voltammetry. The instruments used include a biopotentiostat and a rotation speed controller (Pine Research Instrumentation). The RRDE experiments were carried out according to the protocols outlined in section 2.8. The zinc-air battery evaluation was carried out according to the procedure outlined in section 2.9.

6.3 Results and discussions

SEM images of the NCNT were taken to investigate the microstructure of the material as shown in Figure 49a, where bundles of aligned NCNT (30-50 nm diameter) are observed. TEM images presented in Figure 49b illustrate structural defects in the form of small and round bamboo-like compartments, which are consistently observed with NCNT due to the incorporation of nitrogen atoms into the graphitic structure[140, 192-194].

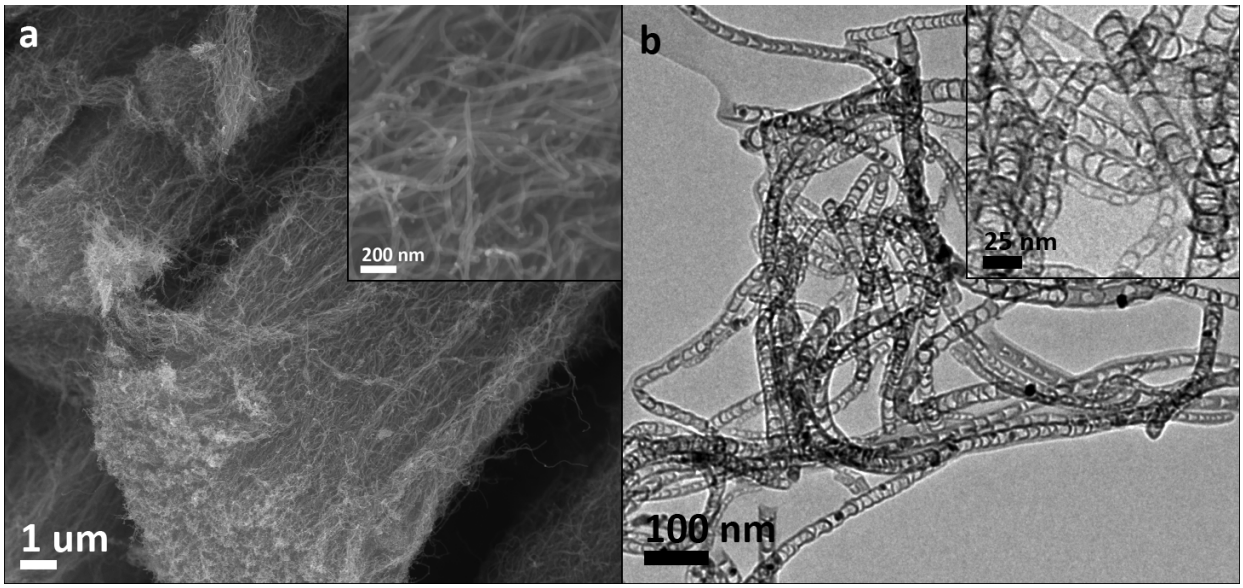

Figure 49 (a) SEM and (b) TEM images of NCNT samples.

RDE voltammetry was utilized in order to determine the half-cell ORR activity of the NCNT in 0.1 M KOH electrolyte. Figure 50 displays the RRDE current-voltage polarization curves obtained at different electrode rotation speeds (100, 400, 900, 1600 and 2500 rpm). NCNT displayed excellent catalyst activity as commonly observed with non-precious electrocatalyst materials in alkaline solution[156, 195]. The nitrogen content of the NCNT utilized in this study has a nitrogen content of approximately 4 at.% (determined by X-ray photoelectron spectroscopy which is not shown here). The overall nitrogen content plays an important role in the ORR activity of NCNT where increase in nitrogen content of the NCNT has been correlated with higher ORR activity [196]. Furthermore, heterogeneous incorporation of nitrogen atom into the graphitic structure of CNTs leads to the creating of many structural defects caused which could exposed edge and planar sites that facilitate the adsorption of molecule oxygen on catalyst surface for improved ORR activity [156, 191]. The ORR polarization curve of NCNT coated electrode can be separated into three regions, 1) kinetically controlled region from ca. -0.05 to -

0.25 V, 2) combined kinetic-diffusion controlled region from ca. -0.25 to -0.6V, and 3) mass diffusion controlled region at potentials greater than -0.6V.

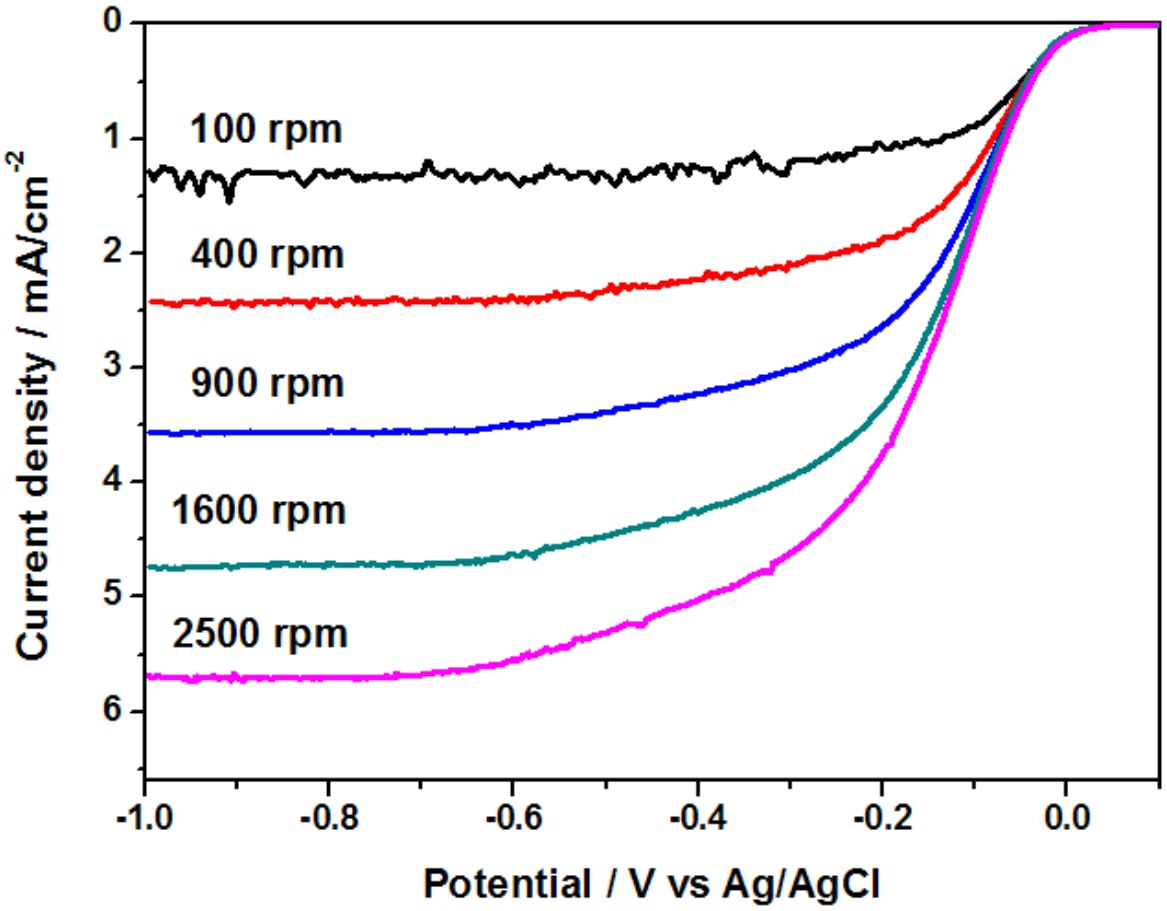

Figure 50 ORR polarization curves of NCNT in 0.1 M KOH.

For a kinetic-diffusion control process, ORR activity can be analyzed using K-L plots. From the K-L plots (Figure 51), the kinetic currents of oxygen reduction can be calculated from the intercepts of the linear K-L relationships. Additionally, the Levich slope and the number of the electrons exchanged in the reduction reaction can be obtained from the slope of the K-L relationships. The K-L plots of the NCNT at different electrode for the NCNT are presented in

Figure 51a showing linear and parallel characteristics in the kinetic-diffusion controlled region are observed, which indicates first-order ORR kinetics with respect to oxygen. The value of Levich slope is 0.116 $mAcm^{-2}rpm^{-1/2}$ according to the K-L plot, which is in good agreement with the theoretical value of 0.104 $mAcm^{-2}rpm^{-1/2}$ for a four-electron reduction of oxygen in 0.1 M KOH. This indicates four-electron reduction process by NCNT making it a promising and effective air-cathode catalyst for zinc-air battery.

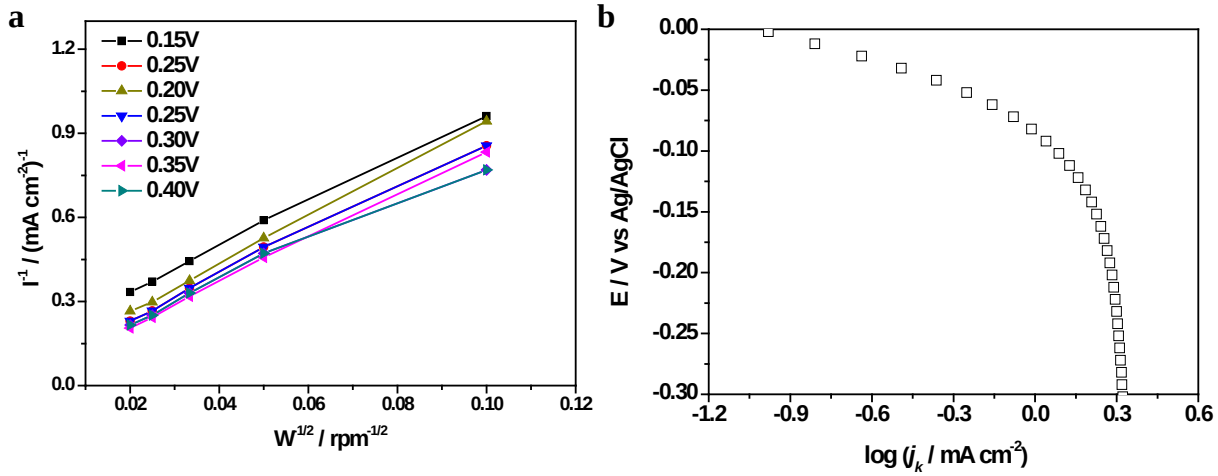

Figure 51 (a) Koutechy-Levich and (b) Tafel plots for NCNT normalized to the electrochemically active surface area for O2 reduction in 0.1 M KOH solution at a rotating speed of 1600 rpm.

Figure 51b presents the Tafel plots for the reduction of oxygen on the NCNT coated electrode. Two distinct Tafel regions with different slopes were obtained. The Tafel slope at low current density is -60 $mVdec^{-1}$, and the Tafel slope at high current density is from -260 to -500 $mVdec^{-1}$. These results indicate that the ORR kinetics on NCNT in alkaline solutions is described by the similar equation in the case of Pt, and the first charge transfer rate is the rate determining step[197]. The existence of two regions with different slopes in the Tafel plots for the NCNT coated

electrode can be explained in terms of the coverage of the electrode surface by adsorbed oxygen species. This coverage follows Temkin and Langmuir isotherm in different current density regions[197, 198].

The electrolyte concentration is one of the key factors affecting the zinc-air battery performance. Polarization and power density curves of NCNT coated cathode operated in different KOH electrolyte are displayed in Fig. 52. From the figures, improved cell performance is evident with increasing KOH concentrations from 1 to 6 M and reaches the optimal performance at 6 M.

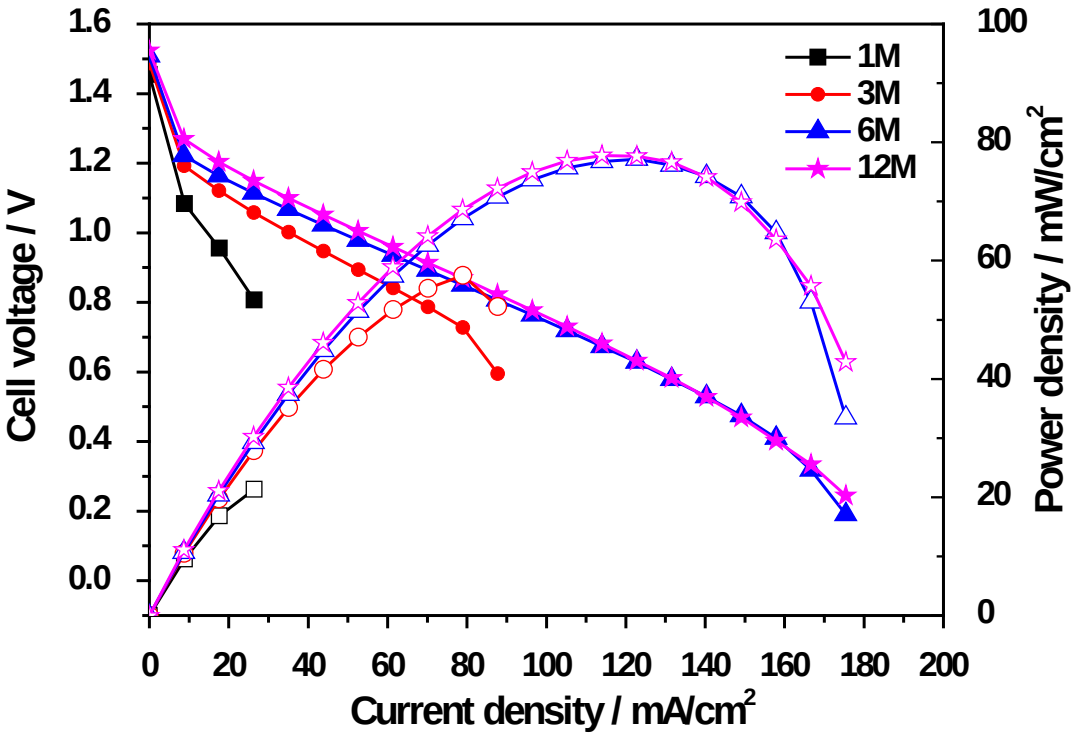

Figure 52 Zinc-air battery polarization and power density curves of NCNT coated electrode.

The observed trend is attributed to the increase in ionic conductivity of the electrolyte. Moreover, increasing KOH concentration is favourable for the anode reaction according to the Nernst

equation. Single cell current density of 24.8, 51.5, and 78.6 $mAcm^{-2}$ was obtained at 0.8 V using 1, 3, and 6 M KOH electrolyte, respectively (Table 17). Similarly, the maximum power density of the zinc-air battery increased from 19.7 to 69.5 $mWcm^{-2}$ when the KOH concentration increased from 1 to 6 M. However, a further increase in KOH concentration from 6 to 12 M did not cause an obvious increase in cell performance. This is attributed to an increase in the solution viscosity and a decrease in the mobility of ions[156, 195]. Based on Figure 52 (or Table 17), using 6 M KOH, which was optimum for the zinc-air battery used for this study.

Table 17 Oxygen electrode activities.

KOH	OCV	Current density at 0.8V	Peak power density	Cathode potential vs Ag/AgCl, I=0,	Peak power density of cathode
M	V	mA cm^{-2}	mW cm^{-2}	V	mW cm^{-2}
1	1.44	24.8	19.7	-0.036	37.2
3	1.43	51.5	46.9	-0.054	107.4
6	1.44	78.6	69.5	-0.084	129.0
12	1.45	78.6	68.8	-0.144	133.3

In order to evaluate the contribution of the cathode catalyst to the overall cell performance, in situ cathodic potentials under different KOH concentrations were tested in the zinc-air battery single cell system (Figure 53). The initial potential of the cathode decreased from -0.036 to -0.144 V vs. Ag/AgCl when the KOH concentration was increased from 1 to 12 M (Table 17). This is mainly attributed to the increasing OH^- concentration at the surface of the cathode taking part in the reaction according to the Nernst equation. The main reason of the difference of

cathode potential in ohmic and concentration loss regime is the change in solution conductivity and viscosity arising from different electrolyte concentration. The air-cathodes operating in 6 and 12 M KOH electrolyte showed very similar maximum power density of 129.0 and 133.3 mWcm^{-2}, respectively.

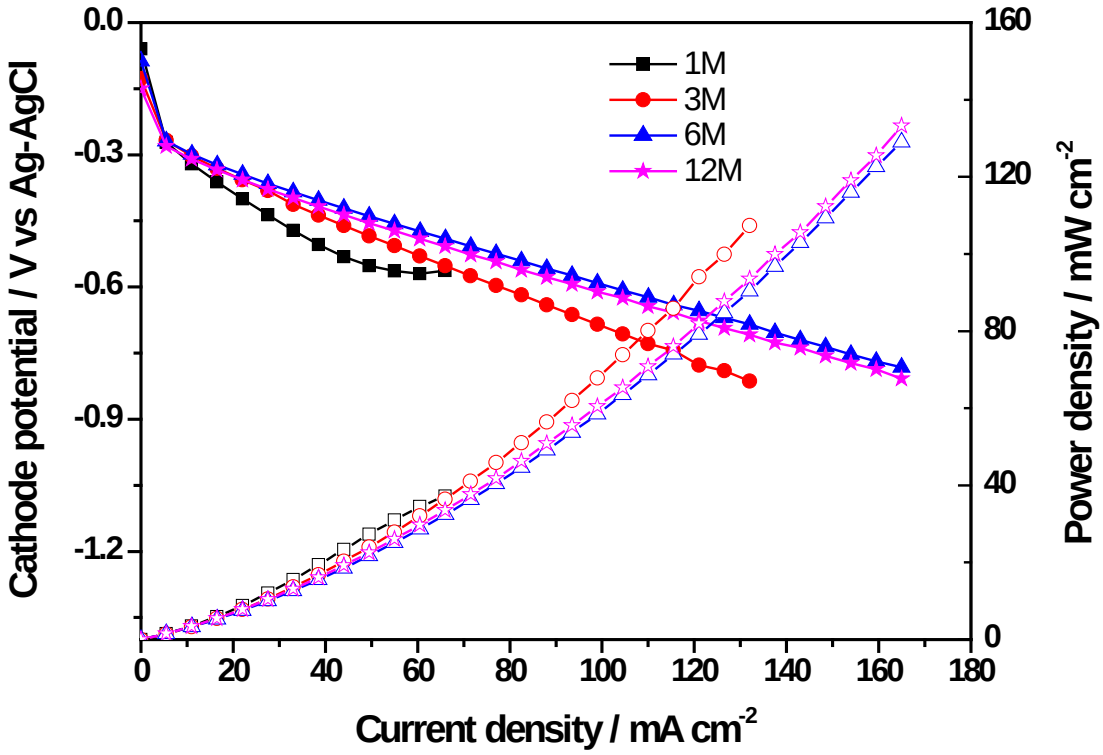

Figure 53 Cathodic potential and power density curves for NCNT coated electrode.

EIS was used to investigate the electrochemical reactions affecting the performance of zinc-air battery electrodes. Critical information such as, charge transfer process of the electrochemical reaction, catalyst conductivity as well as electrode porous structure can be determined by EIS. Compared with polarization occurred on the cathode of zinc-air battery, anode polarization is

often neglected owing to the smaller magnitude[199, 200]. Figure 54 illustrates the Nyquist plots of the zinc-air battery operated in different electrolyte concentration and battery voltage.

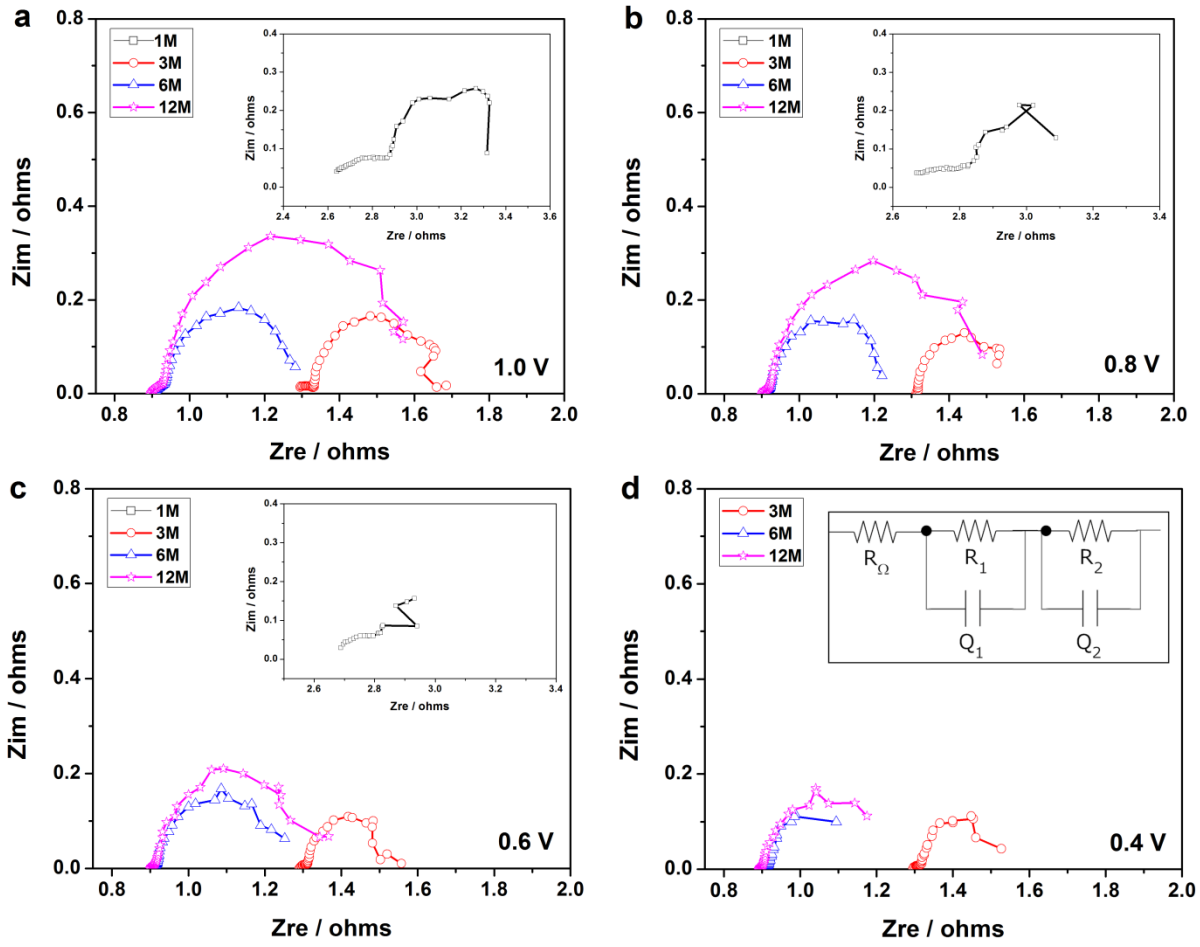

Figure 54 Nyquist plots of zinc-air battery single cells with NCNT catalyst at (a) 1.0, (b) 0.8, (c) 0.6, and (d) 0.4V. Inset of d, illustrates the equivalent circuit used to model the impedance data.

The impedance spectra obtained at 1 M KOH show significant deviation from the spectra obtained at higher electrolyte concentration which could be caused by the low ionic conductivity of the 1 M KOH electrolyte that hinders the discharge process during zinc-air battery operation. Apart from the impedance spectra obtained at high concentration shares similar shape where a

depressed arc at high frequency is preceded by a larger semicircle that spans from mid to low frequency. At the intercept of the impedance spectra at high frequency with the real axis is denoted RΩ, representing the internal resistance of the cell including total ohmic resistance which includes resistance arise from the electrolyte, catalyst layer, as well as contact resistances[201]. The equivalent circuit used to fit the data is showed in the inset of Figure 54d. Through extrapolation of the onset of the semicircle to the real axis, R_1 is obtained. R_1 is strongly related to electrolyte conductivity thus it could reflect the ionic ohmic drop inside the gas diffusion electrode[59, 201]. At the intercept of the impedance spectra a low frequency with the real axis is denoted R_2, representing the mass-transfer process. Based on the impedance data summarized in Table 18, several trends can be observed with respect to the difference resistances in of the equivalent circuit.

Table 18 Parameters evaluated from fit of EIS in zinc-air battery single cell mode

KOH	1.0V			0.8V			0.6V			0.4V		
M	R_Ω	R_1	R_2	R_Ω	R_1	R_2	R_Ω	R_1	R_2	R_Ω	R_1	R_2
1	2.64	0.23	0.67	2.67	0.16	0.42	2.68	0.1	--	--	--	--
3	1.29	0.04	0.38	1.26	0.05	0.27	1.29	0.02	0.27	1.29	0.02	0.24
6	0.91	0.03	0.37	0.91	0.01	0.31	0.91	0.01	0.34	0.91	0.01	0.18
12	0.89	0.04	0.68	0.9	0.02	0.59	0.9	0.01	0.47	0.89	0.01	0.28

Under increasing electrolyte concentration continuous decrease in R_Ω is observed as reflected by the shift in the intercept of the impedance spectra with the real axis at high frequency. This phenomenon is which is expected as R_Ω is correlated with the electrolyte resistance in the zinc-

air battery. Similar trend is observed in R_1 where the strong dependence on electrolyte conductivity leads to a decrease in its value with increase in KOH concentration. However, no further decrease in R_1 value was observed when KOH concentration is increased beyond 3 M. It should be noted that the value of R_1 beyond 3 M is rather small which could be influence by the experimental errors to a certain degree. Therefore, the treatment of the value of R_1 beyond 3 M should be approached with caution. Unlike the previously mentioned resistance, R_2 increase alongside with KOH concentration as reflected by the increase in the low frequency semicircle. This effect has been observed by others[201, 202] where deeper penetration of the porous electrode by highly concentrated KOH results in limited gas accessibility which in turn increases mass transport resistance. Further study of the correlation between of cell voltage and the resistance reveal a decreasing trend with respect to increasing overpotential, R_2 which has been observed previously[203].

6.4 Conclusions and remarks

In summary, NCNT materials possessing a high activity towards the ORR in alkaline solution were employed as air-cathode electrocatalyst material in a single cell zinc-air battery setup. Moreover, the effect of KOH concentration in the zinc-air battery electrolyte was investigated in order to determine the optimal concentration for cell performance, dependent on the ionic conductivity and viscosity of the liquid electrolyte solution. With an air-cathode catalyst loading of 0.2 $mgcm^{-2}$ and an optimal KOH electrolyte concentration of 6 M, a high cell power density of 69.5 $mWcm^{-2}$ was obtained. The excellent ORR activity and single cell performance strongly suggested that NCNT could be promising cathode catalysts for zinc-air battery.

7 Summary and future direction

In summary, excellent properties of NCNT and its great potential towards ORR catalysis have been demonstrated in a lab-made zinc air battery through a series of five investigations. The primary objective was to exploit the unique physical and chemical properties of NCNT towards ORR catalysis. In the process of doing this, the structural dependence of NCNT on the synthesis conditions was investigated. Additionally, the studies highlighted the correlations between structural differences and the ORR activity providing important directions for future studies.

The first paper details the synthesis of NCNT using ferrocene as catalyst and EDA and pyridine as nitrogen and carbon precursors. The premise of the study was based on recent developments regarding the use of nitrogen doped carbon materials towards ORR catalysis. The ORR performance of the NCNT synthesized in this study was investigated in a half-cell RRDE setup and very promising ORR performance were obtained. In particular, the EDA-NCNT illustrated superior performance than the state-of-the-art carbon supported platinum catalyst. The significant finding of this study illustrates the bright future for NPMC and great promising of sustainable energy development. Furthermore, the interesting properties of NCNT warrant future investigation and systematic study of the NCNT materials.

The second and third investigations describe the controlled synthesis of NCNT with different nitrogen content through two methods. First method involves carefully choosing the precursor molecules with varying carbon to nitrogen ratio whereas the second method involves the combination of two precursors at different proportions to create different nitrogen containing

precursor solutions. Through these two methods, the number nitrogen available in the synthesis environment can be controlled to produce NCNT with varying nitrogen content. The premise behind this study is based on the successful demonstration of excellent ORR activity in the first investigation and the fact that nitrogen content has been reported to greatly influence ORR activity of the nitrogen-doped carbon materials. The second and third investigation confirmed the positive correlation between nitrogen content and the ORR activity, but also put forth some concerns, is nitrogen content the only structural property that has significant influence on the ORR activity?

The fourth study was conducted to answer the question asked at the end for section 4. In this study, the NCNT were synthesized using different catalyst which resulted in drastically different surface structure. The premise of this study is from the fact that catalysis is a surface reaction and the nitrogen concentration in the NCNT has been found to be highest at the defects. The electrochemical evaluation of two NCNT catalysts with different degree of defects confirms the positive correlation between surface defects and ORR activity. The significant finding provides another avenue to improve the ORR activity of NCNT besides increasing the NCNT nitrogen content.

After a systematic study of the structural properties of NCNT and identify the aspect of improvement for ORR activity, the most active NCNT sample made from ethylenediamine was used as ORR catalyst in a zinc-air battery. The excellent performance of NCNT in the lab-made zinc-air battery provides additional evidence for the great promise of this material towards ORR catalysis for metal-air battery applications.

The present investigations provide an excellent basis for understanding the fundamentals involved in ORR catalysis by NCNT. Based on this knowledge, many future directions for NCNT materials are possible:

1. Optimization of the ORR activity of NCNT with respect to the nitrogen content and surface defects, while maintaining high electrical conductivity;
2. Combination of NCNT with other catalysts such as manganese oxide particle, via physical mixing to achieve improve stability and further improve the performance in alkaline conditions;
3. Synthesis of hierarchical structure such as core-shell or core-corona structure with metal oxide or mixed metal oxides to incorporate additional functionality. For example incorporation of NCNT as well as lanthanum nickel oxide particles can be used as bifunctional catalyst in rechargeable zinc-air batteries.

References

1. Tombaz, S.; Vastberg, A.; Zander, J. *Ieee Wirel Commun* **2011,** 18, (5), 18-24.
2. Scrosati, B.; Garche, J. *Journal of Power Sources* **2010,** 195, (9), 2419-2430.
3. Wagner, F. T.; Lakshmanan, B.; Mathias, M. F. *Journal of Physical Chemistry Letters* **2010,** 1, (14), 2204-2219.
4. Deane, J. P.; Gallachoir, B. P. O.; McKeogh, E. J. *Renewable & Sustainable Energy Reviews* **2010,** 14, (4), 1293-1302.
5. Armaroli, N.; Balzani, V. *Energy & Environmental Science* **2011,** 4, (9), 3193-3222.
6. Bouffard, F.; Galiana, F. D. *Ieee Transactions on Power Systems* **2008,** 23, (2), 306-316.
7. Denny, E.; O'Malley, M. *Ieee Transactions on Power Systems* **2006,** 21, (1), 341-347.
8. Benitez, L. E.; Benitez, P. C.; van Kooten, G. C. *Energy Economics* **2008,** 30, (4), 1973-1989.
9. Dunn, B.; Kamath, H.; Tarascon, J. M. *Science* **2011,** 334, (6058), 928-935.
10. Skyllas-Kazacos, M.; Chakrabarti, M. H.; Hajimolana, S. A.; Mjalli, F. S.; Saleem, M. *Journal of the Electrochemical Society* **2011,** 158, (8), R55-R79.
11. Soloveichik, G. L. *Annual Review of Chemical and Biomolecular Engineering, Vol 2* **2011,** 2, 503-527.
12. Armand, M.; Tarascon, J. M. *Nature* **2008,** 451, (7179), 652-657.
13. Burke, A. F. *Proceedings of the Ieee* **2007,** 95, (4), 806-820.
14. Winter, M.; Brodd, R. J. *Chemical Reviews* **2004,** 104, (10), 4245-4269.
15. McCloskey, B. D.; Scheffler, R.; Speidel, A.; Bethune, D. S.; Shelby, R. M.; Luntz, A. C. *Journal of the American Chemical Society* **2011,** 133, (45), 18038-18041.
16. Broussely, M.; Planchat, J. P.; Rigobert, G.; Virey, D.; Sarre, G. *Journal of Power Sources* **1997,** 68, (1), 8-12.
17. Kennedy, B.; Patterson, D.; Camilleri, S. *Journal of Power Sources* **2000,** 90, (2), 156-162.
18. Girishkumar, G.; McCloskey, B.; Luntz, A. C.; Swanson, S.; Wilcke, W. *Journal of Physical Chemistry Letters* **2010,** 1, (14), 2193-2203.
19. Vetter, J.; Novak, P.; Wagner, M. R.; Veit, C.; Moller, K. C.; Besenhard, J. O.; Winter, M.; Wohlfahrt-Mehrens, M.; Vogler, C.; Hammouche, A. *Journal of Power Sources* **2005,** 147, (1-2), 269-281.
20. Ji, L. W.; Lin, Z.; Alcoutlabi, M.; Zhang, X. W. *Energy & Environmental Science* **2011,** 4, (8), 2682-2699.
21. Fergus, J. W. *Journal of Power Sources* **2010,** 195, (4), 939-954.
22. Wakihara, M. *Materials Science & Engineering R-Reports* **2001,** 33, (4), 109-134.
23. Arora, P.; White, R. E.; Doyle, M. *Journal of the Electrochemical Society* **1998,** 145, (10), 3647-3667.
24. Blurton, K. F.; Sammells, A. F. *Journal of Power Sources* **1979,** 4, (4), 263-279.
25. Yuasa, M.; Nishida, M.; Kida, T.; Yamazoe, N.; Shimanoe, K. *Journal of the Electrochemical Society* **2011,** 158, (5), A605-A610.
26. Jacoby, M. *Chemical & Engineering News* **2010,** 88, (47), 29-31.
27. Kaisheva, A.; Iliev, I. *New Carbon Based Materials for Electrochemical Energy Storage Systems: Batteries, Supercapacitors and Fuel Cells* **2006,** 229, 117-136.

28. Korovin, N. *New Carbon Based Materials for Electrochemical Energy Storage Systems: Batteries, Supercapacitors and Fuel Cells* **2006,** 229, 137-149.
29. Akani, M. *New Materials for Fuel Cell and Modern Battery Systems Ii* **1997**, 239-251.
30. Shimizu, Y.; Matsuda, H.; Miura, N.; Yamazoe, N. *Chemistry Letters* **1992**, (6), 1033-1036.
31. Iliev, I.; Kaisheva, A.; Gamburzev, S. *Proceedings of the 26th Intersociety Energy Conversion Engineering Conference, Vols 1-6* **1991**, C469-C470.
32. Goldstein, J.; Brown, I.; Koretz, B. *Journal of Power Sources* **1999,** 80, (1-2), 171-179.
33. Kraytsberg, A.; Ein-Eli, Y. *Journal of Power Sources* **2011,** 196, (3), 886-893.
34. Neburchilov, V.; Wang, H. J.; Martin, J. J.; Qu, W. *Journal of Power Sources* **2010,** 195, (5), 1271-1291.
35. Jorissen, L. *Journal of Power Sources* **2006,** 155, (1), 23-32.
36. Nikolova, V.; Iliev, P.; Petrov, K.; Vitanov, T.; Zhecheva, E.; Stoyanova, R.; Valov, I.; Stoychev, D. *Journal of Power Sources* **2008,** 185, (2), 727-733.
37. Chen, G. Y.; Delafuente, D. A.; Sarangapani, S.; Mallouk, T. E. *Catalysis Today* **2001,** 67, (4), 341-355.
38. Lu, Y. C.; Gasteiger, H. A.; Shao-Horn, Y. *Journal of the American Chemical Society* **2011,** 133, (47), 19048-19051.
39. Sheng, W. C.; Lee, S. W.; Crumlin, E. J.; Chen, S.; Shao-Horn, Y. *Journal of the Electrochemical Society* **2011,** 158, (11), B1398-B1404.
40. Kim, J.; Lee, S. W.; Carlton, C.; Shao-Horn, Y. *Electrochemical and Solid State Letters* **2011,** 14, (10), B110-B113.
41. Lu, Y. C.; Xu, Z. C.; Gasteiger, H. A.; Chen, S.; Hamad-Schifferli, K.; Shao-Horn, Y. *Journal of the American Chemical Society* **2010,** 132, (35), 12170-12171.
42. Kim, J.; Lee, S. W.; Carlton, C.; Shao-Horn, Y. *Journal of Physical Chemistry Letters* **2011,** 2, (11), 1332-1336.
43. Lee, S. W.; Chen, S.; Suntivich, J.; Sasaki, K.; Adzic, R. R.; Shao-Horn, Y. *Journal of Physical Chemistry Letters* **2010,** 1, (9), 1316-1320.
44. Marschilok, A. C.; Zhu, S. L.; Milleville, C. C.; Lee, S. H.; Takeuchi, E. S.; Takeuchi, K. J. *Journal of the Electrochemical Society* **2011,** 158, (3), A223-A226.
45. Lee, S.; Zhu, S. L.; Milleville, C. C.; Lee, C. Y.; Chen, P. W.; Takeuchi, K. J.; Takeuchi, E. S.; Marschilok, A. C. *Electrochemical and Solid State Letters* **2010,** 13, (11), A162-A164.
46. Cheng, F. Y.; Shen, J. A.; Peng, B.; Pan, Y. D.; Tao, Z. L.; Chen, J. *Nature Chemistry* **2011,** 3, (1), 79-84.
47. Lee, Y.; Suntivich, J.; May, K. J.; Perry, E. E.; Shao-Horn, Y. *Journal of Physical Chemistry Letters* **2012,** 3, (3), 399-404.
48. Suntivich, J.; May, K. J.; Gasteiger, H. A.; Goodenough, J. B.; Shao-Horn, Y. *Science* **2011,** 334, (6061), 1383-1385.
49. Suntivich, J.; Gasteiger, H. A.; Yabuuchi, N.; Nakanishi, H.; Goodenough, J. B.; Shao-Horn, Y. *Nature Chemistry* **2011,** 3, (8), 647-647.
50. Suntivich, J.; Gasteiger, H. A.; Yabuuchi, N.; Shao-Horn, Y. *Journal of the Electrochemical Society* **2010,** 157, (8), B1263-B1268.
51. Tiwari, S. K.; Koenig, J. F.; Poillerat, G.; Chartier, P.; Singh, R. N. *Journal of Applied Electrochemistry* **1998,** 28, (1), 114-119.
52. Zhuang, S. X.; Huang, C. H.; Huang, K. L.; Hu, X.; Tu, F. Y.; Huang, H. X. *Electrochemistry Communications* **2011,** 13, (4), 321-324.

53. Roche, I.; Chainet, E.; Chatenet, M.; Vondrak, J. *Journal of Physical Chemistry C* **2007,** 111, (3), 1434-1443.
54. Roche, I.; Chainet, E.; Vondrak, J.; Chatenet, M. *Journal of Applied Electrochemistry* **2008,** 38, (9), 1195-1201.
55. Bezdicka, P.; Grygar, T.; Klapste, B.; Vondrak, J. *Electrochimica Acta* **1999,** 45, (6), 913-920.
56. Klapste, B.; Vondrak, J.; Velicka, J. *Electrochimica Acta* **2002,** 47, (15), 2365-2369.
57. Yang, J. S.; Xu, J. J. *Electrochemistry Communications* **2003,** 5, (4), 306-311.
58. Kinoshita, K.; Society, E., *Electrochemical Oxygen Technology*. Wiley: 1992.
59. Cheng, F. Y.; Chen, J. *Chemical Society Reviews* **2012,** 41, (6), 2172-2192.
60. Reddy, T.; Linden, D., *Linden's Handbook of Batteries*. McGraw-Hill: 2010.
61. Wang, X. Y.; Sebastian, P. J.; Smit, M. A.; Yang, H. P.; Gamboa, S. A. *Journal of Power Sources* **2003,** 124, (1), 278-284.
62. Mohamad, A. *Journal of Power Sources* **2006,** 159, (1), 752-757.
63. Padbury, R.; Zhang, X. W. *Journal of Power Sources* **2011,** 196, (10), 4436-4444.
64. Zhang, G. Q.; Zhang, X. G. *Electrochimica Acta* **2004,** 49, (6), 873-877.
65. Ogasawara, T.; Debart, A.; Holzapfel, M.; Novak, P.; Bruce, P. G. *Journal of the American Chemical Society* **2006,** 128, (4), 1390-1393.
66. Hadjipaschalis, I.; Poullikkas, A.; Efthimiou, V. *Renewable & Sustainable Energy Reviews* **2009,** 13, (6-7), 1513-1522.
67. Pytches, R. E. *Electronics and Power* **1983,** 29, (7-8), 577-580.
68. Mclarnon, F. R.; Cairns, E. J. *Journal of the Electrochemical Society* **1991,** 138, (2), 645-664.
69. Li, W. Y.; Li, C. S.; Zhou, C. Y.; Ma, H.; Chen, J. *Angewandte Chemie-International Edition* **2006,** 45, (36), 6009-6012.
70. Lee, J. S.; Kim, S. T.; Cao, R.; Choi, N. S.; Liu, M.; Lee, K. T.; Cho, J. *Advanced Energy Materials* **2011,** 1, (1), 34-50.
71. Yang, C. C.; Lin, S. J. *Journal of Power Sources* **2002,** 112, (1), 174-183.
72. Zhang, X. G. *Journal of Power Sources* **2006,** 163, (1), 591-597.
73. Ullah, S.; Badshah, A.; Ahmed, F.; Raza, R.; Altaf, A. A.; Hussain, R. *International Journal of Electrochemical Science* **2011,** 6, (9), 3801-3811.
74. Devyatkina, T. I.; Gun'ko, Y. L.; Mikhalenko, M. G. *Russ J Appl Chem* **2001,** 74, (7), 1122-1125.
75. Lee, C. W.; Sathiyanarayanan, K.; Eom, S. W.; Yun, M. S. *Journal of Power Sources* **2006,** 160, (2), 1436-1441.
76. Zhang, C.; Wang, J. M.; Zhang, L.; Zhang, J. Q.; Cao, C. N. *Journal of Applied Electrochemistry* **2001,** 31, (9), 1049-1054.
77. Cho, Y. D.; Fey, G. T. K. *Journal of Power Sources* **2008,** 184, (2), 610-616.
78. Ein-Eli, Y.; Auinat, M.; Starosvetsky, D. *Journal of Power Sources* **2003,** 114, (2), 330-337.
79. Pan, J.; Lu, S. F.; Li, Y.; Huang, A. B.; Zhuang, L.; Lu, J. T. *Advanced Functional Materials* **2010,** 20, (2), 312-319.
80. Sapkota, P.; Kim, H. *Journal of Industrial and Engineering Chemistry* **2010,** 16, (1), 39-44.
81. Muller, S.; Striebel, K.; Haas, O. *Electrochimica Acta* **1994,** 39, (11-12), 1661-1668.

82. Gamburzev, S.; Zhang, W.; Velev, O. A.; Srinivasan, S.; Appleby, A. J.; Visintin, A. *Journal of Applied Electrochemistry* **1998,** 28, (5), 545-549.
83. Sakai, T.; Iwaki, T.; Ye, Z.; Noreus, D. *Journal of the Electrochemical Society* **1995,** 142, (12), 4040-4045.
84. Kannan, A. M.; Shukla, A. K.; Sathyanarayana, S. *Journal of Power Sources* **1989,** 25, (2), 141-150.
85. Carlsson, L.; Ojefors, L. *Journal of the Electrochemical Society* **1980,** 127, (3), 525-528.
86. Zhang, J., *PEM Fuel Cell Electrocatalysts and Catalyst Layers: Fundamentals and Applications*. Springer: 2008.
87. Wu, G.; Cui, G. F.; Li, D. Y.; Shen, P. K.; Li, N. *Journal of Materials Chemistry* **2009,** 19, (36), 6581-6589.
88. Malakhov, I. V.; Nikitenko, S. G.; Savinova, E. R.; Kochubey, D. I.; Alonso-Vante, N. *Journal of Physical Chemistry B* **2002,** 106, (7), 1670-1676.
89. Zhang, X. G., *Corrosion and Electrochemistry of Zinc*. Plenum Press: 1996.
90. McLean, G.; Niet, T.; Prince-Richard, S.; Djilali, N. *International Journal of Hydrogen Energy* **2002,** 27, (5), 507-526.
91. Gülzow, E. *Journal of Power Sources* **1996,** 61, (1-2), 99-104.
92. Martin, J.; Neburchilov, V.; Wang, H.; Qu, W. In *Air cathodes for metal-air batteries and fuel cells*, **2009**; IEEE: 2009; pp 1-6.
93. Li, H.; Liu, H.; Jong, Z.; Qu, W.; Geng, D.; Sun, X.; Wang, H. *International Journal of Hydrogen Energy* **2011,** 36, (3), 2258-2265.
94. Baker, R.; Wilkinson, D. P.; Zhang, J. *Electrochimica Acta* **2008,** 53, (23), 6906-6919.
95. Liu, H.; Song, C.; Tang, Y.; Zhang, J. *Electrochimica Acta* **2007,** 52, (13), 4532-4538.
96. Bezerra, C. W. B.; Zhang, L.; Lee, K.; Liu, H.; Zhang, J.; Shi, Z.; Marques, A. L. B.; Marques, E. P.; Wu, S. *Electrochimica Acta* **2008,** 53, (26), 7703-7710.
97. Lee, K.; Zhang, L.; Lui, H.; Hui, R.; Shi, Z.; Zhang, J. *Electrochimica Acta* **2009,** 54, (20), 4704-4711.
98. Zhang, L.; Zhang, J.; Wilkinson, D. P.; Wang, H. *Journal of Power Sources* **2006,** 156, (2), 171-182.
99. Lefévre, M.; Proietti, E.; Jaouen, F.; Dodelet, J. P. *Science* **2009,** 324, (5923), 71-74.
100. Jaouen, F.; Dodelet, J. P. *The Journal of Physical Chemistry C* **2009,** 113, (34), 15422-15432.
101. Tang, Y.; Allen, B. L.; Kauffman, D. R.; Star, A. *Journal of the American Chemical Society* **2009,** 131, (37), 13200-13201.
102. Gong, K.; Du, F.; Xia, Z.; Durstock, M.; Dai, L. *Science* **2009,** 323, (5915), 760-764.
103. Qu, L.; Liu, Y.; Baek, J. B.; Dai, L. *ACS nano* **2010,** 4, (3), 1321-1326.
104. Chen, Z.; Higgins, D.; Tao, H.; Hsu, R. S. *The Journal of Physical Chemistry C* **2009,** 113, (49), 21008-21013.
105. Iijima, S. *Nature* **1991,** 354, (6348), 56-58.
106. Yu, M. F.; Lourie, O.; Dyer, M. J.; Moloni, K.; Kelly, T. F.; Ruoff, R. S. *Science* **2000,** 287, (5453), 637-640.
107. Pop, E.; Mann, D.; Wang, Q.; Goodson, K.; Dai, H. *Nano Letters* **2006,** 6, (1), 96-100.
108. Thostenson, E. T.; Li, C.; Chou, T. W. *Composites Science and Technology* **2005,** 65, (3), 491-516.
109. Hong, S.; Myung, S. *Nature Nanotech* **2007,** 2, 207-8.
110. Lin, M. F., Shung, W.-K. *Physical Review B* **1994,** 50, (23), 17744-17747.

111. Kataura, H.; Kumazawa, Y.; Maniwa, Y.; Umezu, I.; Suzuki, S.; Ohtsuka, Y.; Achiba, Y. *Synthetic Metals* **1999,** 103, (1), 2555-2558.
112. Jorio, A.; Dresselhaus, G.; Dresselhaus, M. S., *Carbon nanotubes: advanced topics in the synthesis, structure, properties and applications*. Springer Verlag: 2008; Vol. 111.
113. Zheng, M.; Diner, B. A. *Journal of the American Chemical Society* **2004,** 126, (47), 15490-15494.
114. Zhou, O.; Fleming, R.; Murphy, D.; Chen, C.; Haddon, R.; Ramirez, A.; Glarum, S. *Science* **1994,** 263, (5154), 1744.
115. Ebbesen, T. W., *Carbon Nanotubes: Preparation and Properties*. CRC Press: 1997.
116. O'Connell, M. J., *Carbon Nanotubes: Properties And Applications*. CRC/Taylor & Francis: 2006.
117. Reich, S.; Thomsen, C.; Maultzsch, J., *Carbon Nanotubes: Basic Concepts and Physical Properties*. John Wiley & Sons: 2008.
118. Ando, T. *NPG Asia Materials* **2009,** 1, (1), 17-21.
119. San, C.; Hong, C. *Journal of the Electrochemical Society* **2012,** 159, (5), 5.
120. Sorescu, D. C.; Jordan, K. D.; Avouris, P. *The Journal of Physical Chemistry B* **2001,** 105, (45), 11227-11232.
121. Stephan, O.; Ajayan, P. M.; Colliex, C.; Redlich, P.; Lambert, J.; Bernier, P.; Lefin, P. *Science* **1994,** 266, (5191), 1683-1685.
122. Han, W.; Bando, Y.; Kurashima, K.; Sato, T. *Chemical physics letters* **1999,** 299, (5), 368-373.
123. Sidik, R. A.; Anderson, A. B.; Subramanian, N. P.; Kumaraguru, S. P.; Popov, B. N. *The Journal of Physical Chemistry B* **2006,** 110, (4), 1787-1793.
124. Cruz-Silva, E.; Cullen, D. A.; Gu, L.; Romo-Herrera, J. M.; Muñoz-Sandoval, E.; López-Urías, F.; Sumpter, B. G.; Meunier, V.; Charlier, J. C.; Smith, D. J. *ACS nano* **2008,** 2, (3), 441-448.
125. Maciel, I.; Campos-Delgado, J.; Cruz-Silva, E.; Pimenta, M.; Sumpter, B.; Meunier, V.; Lopez-Urias, F.; Munoz-Sandoval, E.; Terrones, H.; Terrones, M. *Nano Letters* **2009,** 9, (6), 2267-2272.
126. Sumpter, B. G.; Huang, J.; Meunier, V.; Romo-Herrera, J. M.; Cruz-Silva, E.; Terrones, H.; Terrones, M. *International Journal of Quantum Chemistry* **2009,** 109, (1), 97-118.
127. Reimer, L., *Scanning Electron Microscopy: Physics of Image Formation and Microanalysis*. Springer: 1998.
128. Reimer, L.; Kohl, H., *Transmission Electron Microscopy: Physics of Image Formation*. Springer: 2008.
129. Crain, E. R., *Crain's Petrophysical Handbook*. Spectrum 2000 Mindware: 2010.
130. Saito, Y.; Yoshikawa, T.; Bandow, S.; Tomita, M.; Hayashi, T. *Physical Review B* **1993,** 48, 1907-1909.
131. Wagner, J. M., *X-Ray Photoelectron Spectroscopy*. Nova Science Pub Incorporated: 2010.
132. Van Der Heide, P., *X-Ray Photoelectron Spectroscopy: An Introduction to Principles and Practices*. John Wiley & Sons: 2011.
133. Nefedov, V. I., *X-Ray Photoelectron Spectroscopy of Solid Surfaces*. VSP BV: 1988.
134. Liang, E.; Ding, P.; Zhang, H.; Guo, X.; Du, Z. *Diamond and related materials* **2004,** 13, (1), 69-73.
135. Lin, Y.; Hsu, Y.; Wu, C.; Chen, S.; Chen, K.; Chen, L. *Diamond and related materials* **2009,** 18, (2-3), 433-437.

136. Dresselhaus, M.; Dresselhaus, G.; Jorio, A.; Souza Filho, A.; Saito, R. *Carbon* **2002,** 40, (12), 2043-2061.
137. Ferraro, J. R.; Nakamoto, K.; Brown, C. W., *Introductory Raman Spectroscopy*. Academic Press: 2003.
138. Lefevre, M.; Dodelet, J. P.; Bertrand, P. *Journal of Physical Chemistry B* **2002,** 106, (34), 8705-8713.
139. Yang, J. B.; Liu, D. J.; Kariuki, N. N.; Chen, L. X. *Chem Commun* **2008**, (3), 329-331.
140. Matter, P. H.; Wang, E.; Arias, M.; Biddinger, E. J.; Ozkan, U. S. *Journal of Physical Chemistry B* **2006,** 110, (37), 18374-18384.
141. Maldonado, S.; Stevenson, K. J. *Journal of Physical Chemistry B* **2004,** 108, (31), 11375-11383.
142. Terrones, M.; Terrones, H.; Grobert, N.; Hsu, W. K.; Zhu, Y. Q.; Hare, J. P.; Kroto, H. W.; Walton, D. R. M.; Kohler-Redlich, P.; Ruhle, M.; Zhang, J. P.; Cheetham, A. K. *Applied Physics Letters* **1999,** 75, (25), 3932-3934.
143. Terrones, M.; Redlich, P.; Grobert, N.; Trasobares, S.; Hsu, W. K.; Terrones, H.; Zhu, Y. Q.; Hare, J. P.; Reeves, C. L.; Cheetham, A. K.; Ruhle, M.; Kroto, H. W.; Walton, D. R. M. *Adv Mater* **1999,** 11, (8), 655.
144. Sumpter, B. G.; Meunier, V.; Romo-Herrera, J. M.; Cruz-Silva, E.; Cullen, D. A.; Terrones, H.; Smith, D. J.; Terrones, M. *ACS nano* **2007,** 1, (4), 369-375.
145. Jang, J. W.; Lee, C. E.; Lyu, S. C.; Lee, T. J.; Lee, C. J. *Applied Physics Letters* **2004,** 84, (15), 2877-2879.
146. Elezovic, N. R.; Babic, B. M.; Vracar, L. J. M.; Krstajic, N. V. *J Serb Chem Soc* **2007,** 72, (7), 699-708.
147. Solorza-Feria, O.; Ramirez-Raya, S.; Rivera-Noriega, R.; Ordonez-Regil, E.; Fernandez-Valverde, S. M. *Thin Solid Films* **1997,** 311, (1-2), 164-170.
148. Liu, J.; Czerw, R.; Carroll, D. L. *J Mater Res* **2005,** 20, (2), 538-543.
149. Matter, P. H.; Zhang, L.; Ozkan, U. S. *J Catal* **2006,** 239, (1), 83-96.
150. Maldonado, S.; Morin, S.; Stevenson, K. J. *Carbon* **2006,** 44, (8), 1429-1437.
151. Ghosh, K.; Kumar, M.; Maruyama, T.; Ando, Y. *Carbon* **2009,** 47, (6), 1565-1575.
152. Yang, Q. H.; Hou, P. X.; Unno, M.; Yamauchi, S.; Saito, R.; Kyotani, T. *Nano Letters* **2005,** 5, (12), 2465-2469.
153. Wong, E. W.; Sheehan, P. E.; Lieber, C. M. *Science* **1997,** 277, (5334), 1971-1975.
154. Berber, S.; Kwon, Y. K.; Tomanek, D. *Phys Rev Lett* **2000,** 84, (20), 4613-4616.
155. Higgins, D.; Chen, Z.; Chen, Z. W. *Electrochimica Acta* **2011,** 56, (3), 1570-1575.
156. Chen, Z.; Higgins, D.; Chen, Z. W. *Carbon* **2010,** 48, (11), 3057-3065.
157. Chun, K. Y.; Lee, H. S.; Lee, C. J. *Carbon* **2009,** 47, (1), 169-177.
158. Lin, Y. G.; Hsu, Y. K.; Wu, C. T.; Chen, S. Y.; Chen, K. H.; Chen, L. C. *Diamond and related materials* **2009,** 18, (2-3), 433-437.
159. Reyes-Reyes, M.; Grobert, N.; Kamalakaran, R.; Seeger, T.; Golberg, D.; Ruhle, M.; Bando, Y.; Terrones, H.; Terrones, M. *Chemical physics letters* **2004,** 396, (1-3), 167-173.
160. Yeager, E. *J Mol Catal* **1986,** 38, (1-2), 5-25.
161. Sidik, R. A.; Anderson, A. B.; Subramanian, N. P.; Kumaraguru, S. P.; Popov, B. N. *Journal of Physical Chemistry B* **2006,** 110, (4), 1787-1793.
162. Gochi-Ponce, Y.; Alonso-Nunez, G.; Alonso-Vante, N. *Electrochemistry Communications* **2006,** 8, (9), 1487-1491.

163. Pattabi, M.; Castellanos, R. H.; Castillo, R.; Ocampo, A. L.; Moreira, J.; Sebastian, P. J.; McClure, J. C.; Mathew, X. *International Journal of Hydrogen Energy* **2001,** 26, (2), 171-174.
164. Wakabayashi, N.; Takeichi, M.; Itagaki, M.; Uchida, H.; Watanabe, M. *Journal of Electroanalytical Chemistry* **2005,** 574, (2), 339-346.
165. Halseid, R.; Bystron, T.; Tunold, R. *Electrochimica Acta* **2006,** 51, (13), 2737-2742.
166. Bulusheva, L. G.; Okotrub, A. V.; Kinloch, I. A.; Asanov, I. P.; Kurenya, A. G.; Kudashov, A. G.; Chen, X.; Song, H. *Phys Status Solidi B* **2008,** 245, (10), 1971-1974.
167. Ayala, P.; Gruneis, A.; Kramberger, C.; Rummeli, M. H.; Solorzano, I. G.; Freire, F. L.; Pichler, T. *J Chem Phys* **2007,** 127, (18), 184709.
168. Chen, Z.; Higgins, D.; Chen, Z. W. *Electrochimica Acta* **2010,** 55, (16), 4799-4804.
169. Lefévre, M.; Dodelet, J. P. *Electrochimica Acta* **2003,** 48, (19), 2749-2760.
170. Lalande, G.; Cote, R.; Guay, D.; Dodelet, J. P.; Weng, L. T.; Bertrand, P. *Electrochimica Acta* **1997,** 42, (9), 1379-1388.
171. Strelko, V. V.; Kartel, N. T.; Dukhno, I. N.; Kuts, V. S.; Clarkson, R. B.; Odintsov, B. M. *Surface Science* **2004,** 548, (1-3), 281-290.
172. Strelko, V. V.; Kuts, V. S.; Thrower, P. A. *Carbon* **2000,** 38, (10), 1499-1503.
173. Wei, G.; Wainright, J. S.; Savinell, R. F. *Journal of New Materials for Electrochemical Systems* **2000,** 3, (2), 121-129.
174. Matter, P. H.; Wang, E.; Arias, M.; Biddinger, E. J.; Ozkan, U. S. *J Mol Catal a-Chem* **2007,** 264, (1-2), 73-81.
175. Shao, Y. Y.; Sui, J. H.; Yin, G. P.; Gao, Y. Z. *Applied Catalysis B-Environmental* **2008,** 79, (1-2), 89-99.
176. Ozaki, J.; Kimura, N.; Anahara, T.; Oya, A. *Carbon* **2007,** 45, (9), 1847-1853.
177. Terrones, M.; Grobert, N.; Olivares, J.; Zhang, J. P.; Terrones, H.; Kordatos, K.; Hsu, W. K.; Hare, J. P.; Townsend, P. D.; Prassides, K.; Cheetham, A. K.; Kroto, H. W.; Walton, D. R. M. *Nature* **1997,** 388, (6637), 52-55.
178. Sen, R.; Satishkumar, B. C.; Govindaraj, A.; Harikumar, K. R.; Raina, G.; Zhang, J. P.; Cheetham, A. K.; Rao, C. N. R. *Chemical physics letters* **1998,** 287, (5-6), 671-676.
179. Liu, J. W.; Webster, S.; Carroll, D. L. *Journal of Physical Chemistry B* **2005,** 109, (33), 15769-15774.
180. Gojkovic, S. L.; Gupta, S.; Savinell, R. F. *Journal of Electroanalytical Chemistry* **1999,** 462, (1), 63-72.
181. Gouerec, P.; Biloul, A.; Contamin, O.; Scarbeck, G.; Savy, M.; Riga, J.; Weng, L. T.; Bertrand, P. *Journal of Electroanalytical Chemistry* **1997,** 422, (1-2), 61-75.
182. Wiesener, K. *Electrochimica Acta* **1986,** 31, (8), 1073-1078.
183. Gupta, S.; Tryk, D.; Bae, I.; Aldred, W.; Yeager, E. *Journal of Applied Electrochemistry* **1989,** 19, (1), 19-27.
184. Rodriguez, N. M. *J Mater Res* **1993,** 8, (12), 3233-3250.
185. Baker, R. T. K. *Carbon* **1989,** 27, (3), 315-323.
186. Baker, R. T. K.; Kim, M. S.; Chambers, A.; Park, C.; Rodriguez, N. M. *Stud Surf Sci Catal* **1997,** 111, 99-109.
187. Rodriguez, N. M.; Chambers, A.; Baker, R. T. K. *Langmuir* **1995,** 11, (10), 3862-3866.
188. Terrones, H.; Hayashi, T.; Munoz-Navia, M.; Terrones, M.; Kim, Y. A.; Grobert, N.; Kamalakaran, R.; Dorantes-Davila, J.; Escudero, R.; Dresselhaus, M. S.; Endo, M. *Chemical physics letters* **2001,** 343, (3-4), 241-250.

189. Zhang, L.; Zhang, J. J.; Wilkinson, D. P.; Wang, H. J. *Journal of Power Sources* **2006,** 156, (2), 171-182.
190. Zhu, S. M.; Chen, Z.; Li, B.; Higgins, D.; Wang, H. J.; Li, H.; Chen, Z. W. *Electrochimica Acta* **2011,** 56, (14), 5080-5084.
191. Higgins, D. C.; Meza, D.; Chen, Z. W. *Journal of Physical Chemistry C* **2010,** 114, (50), 21982-21988.
192. Biddinger, E. J.; von Deak, D.; Ozkan, U. S. *Top Catal* **2009,** 52, (11), 1566-1574.
193. Nallathambi, V.; Lee, J. W.; Kumaraguru, S. P.; Wu, G.; Popov, B. N. *Journal of Power Sources* **2008,** 183, (1), 34-42.
194. Gong, K. P.; Du, F.; Xia, Z. H.; Durstock, M.; Dai, L. M. *Science* **2009,** 323, (5915), 760-764.
195. Chen, Z.; Choi, J. Y.; Wang, H. J.; Li, H.; Chen, Z. W. *Journal of Power Sources* **2011,** 196, (7), 3673-3677.
196. Li, X. X.; Zhu, A. L.; Qu, W.; Wang, H. J.; Hui, R.; Zhang, L.; Zhang, J. J. *Electrochimica Acta* **2010,** 55, (20), 5891-5898.
197. Tammeveski, K.; Arulepp, M.; Tenno, T.; Ferrater, C.; Claret, J. *Electrochimica Acta* **1997,** 42, (19), 2961-2967.
198. Paganin, V. A.; Oliveira, C. L. F.; Ticianelli, E. A.; Springer, T. E.; Gonzalez, E. R. *Electrochimica Acta* **1998,** 43, (24), 3761-3766.
199. Bidault, F.; Kucernak, A. *Journal of Power Sources* **2010,** 195, (9), 2549-2556.
200. Chen, G. B.; Zhang, H. M.; Ma, H. P.; Zhong, H. X. *Electrochimica Acta* **2009,** 54, (23), 5454-5462.
201. Bidault, F.; Brett, D. J. L.; Middleton, P. H.; Abson, N.; Brandon, N. P. *International Journal of Hydrogen Energy* **2010,** 35, (4), 1783-1788.
202. Kheirmand, M.; Gharibi, H.; Mirzaie, R. A.; Faraji, M.; Zhiani, M. *Journal of Power Sources* **2007,** 169, (2), 327-333.
203. Genies, L.; Bultel, Y.; Faure, R.; Durand, R. *Electrochimica Acta* **2003,** 48, (25-26), 3879-3890.

Appendix

Published papers are used in the thesis. The permissions to reuse the published results have been granted by the Publisher. Below are the License number from the Publishers.

Elsevier Publishing, 2903821337984, 2903821219014, 2903821015886, and 2903820906932